BNL–52627, CLNS 01/1729, FERMILAB–Pub–01/058-E,
LBNL–47813, SLAC–R–570, UCRL–ID–143810–DR
LC–REV–2001–074–US
hep-ex/0106058
June 2001

Linear Collider Physics Resource Book for Snowmass 2001

Part 4: Theoretical, Accelerator, and Experimental Options

American Linear Collider Working Group *

Abstract

This Resource Book reviews the physics opportunities of a next-generation e^+e^- linear collider and discusses options for the experimental program. Part 4 discusses options for the linear collider program, at a number of levels. First, it presents a broad review of physics beyond the Standard Model, indicating how the linear collider is relevant to each possible pathway. Next, it surveys options for the accelerator and experimental plan, including the questions of the running scenario, the issue of one or two interaction regions, and the options for positron polarization, photon-photon collisions, and e^-e^- collisions. Finally, it reviews the detector design issues for the linear collider and presents three possible detector designs.

*Work supported in part by the US Department of Energy under contracts DE–AC02–76CH03000, DE–AC02–98CH10886, DE–AC03–76SF00098, DE–AC03–76SF00515, and W–7405–ENG–048, and by the National Science Foundation under contract PHY-9809799.

Linear Collider Physics Resource Book for Snowmass 2001

American Linear Collider
Working Group

BNL–52627, CLNS 01/1729, FERMILAB–Pub–01/058-E,
LBNL–47813, SLAC–R–570, UCRL–ID–143810–DR

LC–REV–2001–074–US

June 2001

Cover: Events of $e^+e^- \to Z^0h^0$, simulated with the Large linear collider detector described in Chapter 15. Front cover: $h^0 \to \tau^+\tau^-$, $Z^0 \to b\overline{b}$. Back cover: $h^0 \to b\overline{b}$, $Z^0 \to \mu^+\mu^-$.

Typset in LaTeX by S. Jensen.

Prepared for the Department of Energy under contract number DE–AC03–76SF00515 by Stanford Linear Accelerator Center, Stanford University, Stanford, California. Printed in the United State of America. Available from National Technical Information Services, US Department of Commerce, 5285 Port Royal Road, Springfield, Virginia 22161.

American Linear Collider Working Group

T. Abe[52], N. Arkani-Hamed[29], D. Asner[30], H. Baer[22], J. Bagger[26], C. Balazs[23], C. Baltay[59], T. Barker[16], T. Barklow[52], J. Barron[16], U. Baur[38], R. Beach[30] R. Bellwied[57], I. Bigi[41], C. Blöchinger[58], S. Boege[47], T. Bolton[27], G. Bower[52], J. Brau[42], M. Breidenbach[52], S. J. Brodsky[52], D. Burke[52], P. Burrows[43], J. N. Butler[21], D. Chakraborty[40], H. C. Cheng[14], M. Chertok[6], S. Y. Choi[15], D. Cinabro[57], G. Corcella[50], R. K. Cordero[16], N. Danielson[16], H. Davoudiasl[52], S. Dawson[4], A. Denner[44], P. Derwent[21], M. A. Diaz[12], M. Dima[16], S. Dittmaier[18], M. Dixit[11], L. Dixon[52], B. Dobrescu[59], M. A. Doncheski[46], M. Duckwitz[16], J. Dunn[16], J. Early[30], J. Erler[45], J. L. Feng[35], C. Ferretti[37], H. E. Fisk[21], H. Fraas[58], A. Freitas[18], R. Frey[42], D. Gerdes[37], L. Gibbons[17], R. Godbole[24], S. Godfrey[11], E. Goodman[16], S. Gopalakrishna[29], N. Graf[52], P. D. Grannis[39], J. Gronberg[30], J. Gunion[6], H. E. Haber[9], T. Han[55], R. Hawkings[13], C. Hearty[3], S. Heinemeyer[4], S. S. Hertzbach[34], C. Heusch[9], J. Hewett[52], K. Hikasa[54], G. Hiller[52], A. Hoang[36], R. Hollebeek[45], M. Iwasaki[42], R. Jacobsen[29], J. Jaros[52], A. Juste[21], J. Kadyk[29], J. Kalinowski[57], P. Kalyniak[11], T. Kamon[53], D. Karlen[11], L. Keller[52] D. Koltick[48], G. Kribs[55], A. Kronfeld[21], A. Leike[32], H. E. Logan[21], J. Lykken[21], C. Macesanu[50], S. Magill[1], W. Marciano[4], T. W. Markiewicz[52], S. Martin[40], T. Maruyama[52], K. Matchev[13], K. Moenig[19], H. E. Montgomery[21], G. Moortgat-Pick[18], G. Moreau[33], S. Mrenna[6], B. Murakami[6], H. Murayama[29], U. Nauenberg[16], H. Neal[59], B. Newman[16], M. Nojiri[28], L. H. Orr[50], F. Paige[4], A. Para[21], S. Pathak[45], M. E. Peskin[52], T. Plehn[55], F. Porter[10], C. Potter[42], C. Prescott[52], D. Rainwater[21], T. Raubenheimer[52], J. Repond[1], K. Riles[37], T. Rizzo[52], M. Ronan[29], L. Rosenberg[35], J. Rosner[14], M. Roth[31], P. Rowson[52], B. Schumm[9], L. Seppala[30], A. Seryi[52], J. Siegrist[29], N. Sinev[42], K. Skulina[30], K. L. Sterner[45], I. Stewart[8], S. Su[10], X. Tata[23], V. Telnov[5], T. Teubner[49], S. Tkaczyk[21], A. S. Turcot[4], K. van Bibber[30], R. van Kooten[25], R. Vega[51], D. Wackeroth[50], D. Wagner[16], A. Waite[52], W. Walkowiak[9], G. Weiglein[13], J. D. Wells[6], W. Wester, III[21], B. Williams[16], G. Wilson[13], R. Wilson[2], D. Winn[20], M. Woods[52], J. Wudka[7], O. Yakovlev[37], H. Yamamoto[23] H. J. Yang[37]

[1] Argonne National Laboratory, Argonne, IL 60439
[2] Universitat Autonoma de Barcelona, E-08193 Bellaterra,Spain
[3] University of British Columbia, Vancouver, BC V6T 1Z1, Canada
[4] Brookhaven National Laboratory, Upton, NY 11973
[5] Budker INP, RU-630090 Novosibirsk, Russia
[6] University of California, Davis, CA 95616
[7] University of California, Riverside, CA 92521
[8] University of California at San Diego, La Jolla, CA 92093
[9] University of California, Santa Cruz, CA 95064
[10] California Institute of Technology, Pasadena, CA 91125
[11] Carleton University, Ottawa, ON K1S 5B6, Canada
[12] Universidad Catolica de Chile, Chile
[13] CERN, CH-1211 Geneva 23, Switzerland
[14] University of Chicago, Chicago, IL 60637
[15] Chonbuk National University, Chonju 561-756, Korea
[16] University of Colorado, Boulder, CO 80309
[17] Cornell University, Ithaca, NY 14853
[18] DESY, D-22063 Hamburg, Germany
[19] DESY, D-15738 Zeuthen, Germany
[20] Fairfield University, Fairfield, CT 06430
[21] Fermi National Accelerator Laboratory, Batavia, IL 60510
[22] Florida State University, Tallahassee, FL 32306
[23] University of Hawaii, Honolulu, HI 96822
[24] Indian Institute of Science, Bangalore, 560 012, India
[25] Indiana University, Bloomington, IN 47405
[26] Johns Hopkins University, Baltimore, MD 21218
[27] Kansas State University, Manhattan, KS 66506
[28] Kyoto University, Kyoto 606, Japan
[29] Lawrence Berkeley National Laboratory, Berkeley, CA 94720
[30] Lawrence Livermore National Laboratory, Livermore, CA 94551
[31] Universität Leipzig, D-04109 Leipzig, Germany
[32] Ludwigs-Maximilians-Universität, München, Germany
[32a] Manchester University, Manchester M13 9PL, UK
[33] Centre de Physique Theorique, CNRS, F-13288 Marseille, France
[34] University of Massachusetts, Amherst, MA 01003
[35] Massachussetts Institute of Technology, Cambridge, MA 02139
[36] Max-Planck-Institut für Physik, München, Germany
[37] University of Michigan, Ann Arbor MI 48109
[38] State University of New York, Buffalo, NY 14260
[39] State University of New York, Stony Brook, NY 11794
[40] Northern Illinois University, DeKalb, IL 60115

[41] University of Notre Dame, Notre Dame, IN 46556
[42] University of Oregon, Eugene, OR 97403
[43] Oxford University, Oxford OX1 3RH, UK
[44] Paul Scherrer Institut, CH-5232 Villigen PSI, Switzerland
[45] University of Pennsylvania, Philadelphia, PA 19104
[46] Pennsylvania State University, Mont Alto, PA 17237
[47] Perkins-Elmer Bioscience, Foster City, CA 94404
[48] Purdue University, West Lafayette, IN 47907
[49] RWTH Aachen, D-52056 Aachen, Germany
[50] University of Rochester, Rochester, NY 14627
[51] Southern Methodist University, Dallas, TX 75275
[52] Stanford Linear Accelerator Center, Stanford, CA 94309
[53] Texas A&M University, College Station, TX 77843
[54] Tokoku University, Sendai 980, Japan
[55] University of Wisconsin, Madison, WI 53706
[57] Uniwersytet Warszawski, 00681 Warsaw, Poland
[57] Wayne State University, Detroit, MI 48202
[58] Universität Würzburg, Würzburg 97074, Germany
[59] Yale University, New Haven, CT 06520

Work supported in part by the US Department of Energy under contracts DE–AC02–76CH03000, DE–AC02–98CH10886, DE–AC03–76SF00098, DE–AC03–76SF00515, and W–7405–ENG–048, and by the National Science Foundation under contract PHY-9809799.

Pathways Beyond the Standard Model

Chapter 9 Pathways Beyond the Standard Model

1 Introduction

Over the past 30 years or so, high energy physics experiments have systematically explored the behavior of the strong, electromagnetic and weak interactions. For the strong interactions, QCD is generally accepted as the correct description, and research on QCD has shifted to its application to special regimes such as diffractive and exclusive processes and the quark-gluon plasma. For the electromagnetic and weak interactions, the progress of the past decade on W, Z, top, and neutrino physics has demonstrated that their structure is understood with high precision.

Our current picture of the electroweak interactions requires spontaneous gauge symmetry breaking. As yet, there is no direct evidence on the means by which the gauge symmetry is broken. It is remarkable that all of the evidence accumulated to date is consistent with the Standard Model (SM) in which this symmetry breaking is due to a single elementary scalar field, the Higgs field, which generates the masses of the W and Z bosons and the quarks and leptons.

However, many features of this simple theory are inadequate. The Higgs field is an *ad hoc* addition to the SM. Its mass and symmetry-breaking expectation value are put in by hand. The quark and lepton masses are generated by arbitrary couplings to the Higgs field. The existence of three generations of quarks and leptons is not explained, nor is the dramatic lack of symmetry in the masses and mixings of these generations.

To explain these features, it is necessary to extend the SM. These extensions, in turn, predict new particles and phenomena. The compelling motivation for new experiments at the highest energies is to discover these phenomena and then to decipher them, so that we can learn the nature of the new laws of physics with which they are associated.

In this document, we are exploring the physics case for a next-generation e^+e^- linear collider. To make this case, it is necessary to demonstrate that the linear collider can have an important impact on our understanding of these new phenomena. The argument should be made broadly for models of new physics covering the whole range of possibilities allowed from our current knowledge. It should take into account new information that we will learn from the Tevatron and LHC experiments which will be done before the linear collider is completed.

Our purpose in this chapter is to give an overview of possibilities for new physics beyond the SM. Our emphasis will be on general orientation to the pathways that one might follow. We will then explain the relevance of the linear collider measurements

to each possible scenario. We encourage the reader to consult the relevant chapter of the 'Sourcebook', Chapters 3–8, to see how each quantity we discuss is measured at a linear collider and why the experimental precision that we expect is justified.

The essay is organized as follows: In Section 2, we discuss the general principle that we use to organize models of new physics. In Sections 3 and 4, we discuss models of new physics in the typical dichotomy used since the 1980's: on the one hand, models with supersymmetry, on the other hand, models with new strong interactions at the TeV scale. In Section 5, we discuss a new class of models for which the key ingredient is the existence of extra spatial dimensions. It is now understood that these models stand on the same footing as the more traditional schemes and, in fact, address certain of their weaknesses. Section 6 gives some conclusions.

2 Beyond the Standard Model

We first discuss some general principles regarding physics beyond the Standard Model.

From an experimental point of view, it is necessary to study the interactions of the observed particles at higher energies and with higher accuracy. This may lead to the discovery of new particles, in which case we need to study their spectrum and determine their interactions. Alternatively, it may lead to the observation of anomalous properties of the observed particles, in which case we could infer the existence of new particles or phenomena responsible for these effects. After this information is obtained in experiments, we must attempt to reconstruct the structure of the underlying theory. The linear collider is a crucial complement to the LHC in ensuring that the experimental information is extensive and precise enough for this goal to be achieved.

From the theoretical point of view, different ideas lead to models that provide challenges to this experimental program. To discuss the range of possible models, an organizing principle is needed. We will organize our discussion around the major question that we believe most strongly motivates new physics at the TeV scale. This is the *stability crisis* in the SM explanation for electroweak symmetry breaking. In technical terms, this is the problem that the Higgs boson mass is extremely sensitive to physics at very high energy scales. In the SM, the effect of quantum fields at the energy scale M is an additive contribution to the Higgs boson mass term of order M^2. More physically, this is the problem that not only the magnitude but even the sign of the Higgs boson mass term is not predicted in the SM, so that the SM cannot explain *why* the electroweak gauge symmetry is broken. From either perspective, this problem suggests that the SM is a dramatically incomplete picture of electroweak symmetry breaking. It is for this reason that we believe that new physics must appear at the TeV scale. We expect that the physics will be more exciting than simply the

production of some random new particles. The solution of the stability crisis will involve completely new principles of physics. These principles will be reflected in the spectrum and properties of the new particles, and in their interactions. Much as the discovery of the J/ψ convincingly brought together many different elements of the SM in a coherent picture, so the discovery and study of these new states will spur us on to the construction of a new theory that will displace the SM.

We will use the idea of solving the stability crisis to guide our classification of the various models of new physics. The three approaches to this problem that have received the most study are supersymmetry, strongly coupled theories, and extra dimensions. The common theme in all three proposed solutions is that additional particle states and dynamics must be present near the electroweak scale. We briefly describe each approach, summarizing in each case the types of new interactions expected and the key experimental issues they raise.

Each possible model of new physics must be approached from the viewpoint expressed at the beginning of this section, that of dissecting experimentally the spectrum of new particles and their interactions. We take particular note of the important strengths that the linear collider brings to disentangling the physics of these models. We will see that, in most cases, the linear collider not only contributes but is *essential* to forming this experimental picture. Even if none of the specific models we discuss here is actually realized in Nature, this exercise illustrates the importance of the linear collider in unraveling the new world beyond the SM.

3 Supersymmetry

One attempt to cure the stability crisis of the Higgs field is to introduce a new symmetry—supersymmetry—which relates fermions and bosons. To realize this symmetry in Nature, there must exist supersymmetry partners for each of the known SM particles. Further, supersymmetry must be broken in the ground state so that these superpartners are more massive than ordinary particles. The Higgs mass terms are then not sensitive to mass scales above the superpartner masses. The Higgs field vacuum expectation value is naturally of order 100 GeV if the superpartner masses are also near this energy scale.

The existence of superpartners implies a rich program for future accelerators. The phenomenology of supersymmetry has been studied in great detail in the literature. Dozens of papers have been written on the technical ability of linear collider experiments to discover and study supersymmetric theories of many different forms. This material is reviewed systematically in Chapter 4 of this book. Different patterns of supersymmetry breaking masses can yield substantially different phenomenology at a high-energy collider. Supersymmetry is not a dot on the theoretical landscape, but rather contains a tremendously varied range of possibilities to be searched for and

studied at all available high-energy collider facilities.

In the remainder of this section, we summarize the most important issues for the study of supersymmetry and the relevant measurements that can be done at a linear collider. It is important to keep in mind that we are likely to be surprised with the spectrum that Nature ultimately gives us. The linear collider's ability to cleanly disentangle the superpartner mass spectrum and couplings would be extremely important when the surprises occur. Of course, this is relevant only if the linear collider has sufficiently high center-of-mass energy to produce the superpartners. Section 2 of Chapter 4 reviews the expectations for the masses of superpartners and gives estimates of what center-of-mass energies should be required.

Mass measurements of accessible sparticles. If supersymmetry is relevant for electroweak symmetry breaking, then some of the superpartners should be discovered at the LHC. Furthermore, the experiments at the LHC should be able to accurately measure some masses or mass differences of the SUSY spectrum. This issue is reviewed in Chapter 4, Section 7. However, the systematic measurement of the SUSY spectrum requires a linear collider.

Superpartner masses are measured at a linear collider in three main ways: from distributions of the products of an on-shell superpartner decay, from threshold scans, and from contributions of virtual superpartners to cross sections or decay amplitudes. When sleptons, charginos, and neutralinos are produced on-shell, their masses will typically be measured to within about 1%. Even if the lightest neutralino LSP is not directly observed, its mass should be measurable to within 1% from these kinematic distributions. Threshold scans of sleptons in e^+e^- collisions and especially in e^-e^- collisions may yield mass measurements to within one part in a thousand. Indirect off-shell mass measurements are more model-dependent but have power in specific applications. For example, the t-channel sneutrino contribution to chargino pair production may allow the presence of the sneutrino to be deduced when its mass is as high as twice the center-of-mass energy of the collider. These techniques are reviewed in more detail in Chapter 4, Section 3.

Slepton and squark quantum numbers and mixing angles. When sparticle mixing can be ignored, the cross sections for pair production of squarks and sleptons at a linear collider are precisely determined by the SM quantum numbers. This should allow unambiguous checks of the quantum numbers and spins for sparticles of the first two generations. In particular, it is straightforward to distinguish the superpartners of left- and right-handed species (*e.g.*, $\tilde{e}_L$ from $\tilde{e}_R$) by cross section measurements with polarized beams. Third-generation sleptons and squarks are likely to be the most strongly mixed scalars of supersymmetry, forming mass eigenstates $\tilde{\tau}_{1,2}$, $\tilde{b}_{1,2}$, and $\tilde{t}_{1,2}$. Separation of these eigenstates and accurate measurement of their masses are difficult at the Tevatron and LHC but present no extraordinary problems to a linear collider. By combining direct mass measurements with polarization asymmetries for

the production of these sparticles, we can determine the mixing angle needed to form the observed mass eigenstates from the left- and right-handed weak-interaction eigenstates. The uncertainty in this determination depends on the parameters of the theory, but it has been demonstrated for some cases that the error is lower than 1%.

Chargino/neutralino parameters. The neutralino and chargino states may be strongly mixed combinations of gauge boson and Higgs boson superpartners. The mass matrix is determined by four parameters of the underlying Lagrangian: M_1 (bino mass), M_2 (wino mass), μ (supersymmetric higgsino mass) and $\tan\beta$ (ratio of Higgs vacuum expectation values). Precision measurements of masses, mixing angles, and couplings associated with chargino and neutralino production can supply the information to determine these four important underlying parameters of supersymmetry. For example, measurements of chargino production alone can, in some cases, determine $\tan\beta$ to better than 10% with only 100 fb^{-1} of data. The parameters M_1, M_2, and possibly μ can be determined at the percent level in large portions of the accessible supersymmetry parameter space.

Coupling relations. To establish supersymmetry as a principle of Nature, it is important to verify some of the symmetry relations that that principle predicts. An essential consequence of supersymmetry is that the couplings of sparticles to gauginos are equal to the corresponding couplings of particles to gauge bosons. It has been demonstrated that this equality can be tested at a linear collider to levels better than 1% for weakly interacting sparticles. The precision is sufficiently good that one can even contemplate measuring the tiny deviations from coupling equivalence that are caused by supersymmetry-breaking effects in loop corrections. This can give an estimate of the masses of unobserved sparticles with mass well above the collider energy, in the same way that the current precision measurements predict the mass of the Higgs. This issue is reviewed in Chapter 4, Section 4.

CP violating phases. The SM apparently does not have enough CP violation to account for the baryon asymmetry in the universe. Supersymmetry has parameters that may introduce additional sources of CP violation into the theory. Testing for the existence of such phases would be an important part of a full supersymmetry program. It has been shown that the linear collider can determine evidence for additional non-zero CP-violating phases in supersymmetric theories if the phases are large enough ($\phi_i \sim 0.1$), even accounting for the constraints from electric dipole moment measurements.

Lepton number violation. Recent data suggest that neutrinos have non-zero masses and mixings. This implies that non-zero lepton flavor angles should be present for leptons, in parallel with the CKM angles for the quarks. These rotation angles are difficult to measure using high-energy leptons because neutrinos are invisible and are summed over in most observables. However, these angles could be detected from

superpartner decays, such as $\tilde{\mu}^+\tilde{\mu}^- \to e^+\mu^-\tilde{\chi}_1^0\tilde{\chi}_1^0$. A linear collider can use these measurements to probe the lepton flavor angles with greater sensitivity than any existing experiment in some parts of parameter space.

Complete spectrum. The LHC will be a wonderful machine for the discovery of many supersymmetric sparticles in large regions of parameter space. The linear collider can add to the superpartner discoveries at the LHC by detecting states that are not straightforward to observe in the pp environment. The discovery abilities of the linear collider begin to be important at energies above LEPII and become increasingly important at energies of 500 GeV and beyond. One example of this is slepton studies. Sleptons with masses above about 300 GeV will be difficult to find at the LHC, especially if they are not produced copiously in the cascade decays of other strongly-interacting superpartners. Furthermore, if the left- and right-sleptons are close in mass to each other they will be difficult to resolve. The linear collider produces sleptons directly if the CM energy is sufficient. The two species of sleptons are readily distinguished using beam polarization and other observables. Another discovery issue arises in the case of a neutral wino or higgsino LSP, with a nearly degenerate charged $\widetilde{W}^\pm$ just above it in mass. The wino case occurs, for example, in anomaly-mediated and in $U(1)$-mediated supersymmetry breaking. In the limit in which all other superpartners are too massive to be produced at the LHC or LC, the linear collider with energy above 500 GeV and 100 fb^{-1} is expected to have a higher mass reach than the LHC for these states. There are other important cases, such as R-parity-violating supersymmetry, in which the linear collider is needed to discover or resolve states of the supersymmetry spectrum.

Supersymmetry and Higgs bosons. The minimal supersymmetric extension of the SM (MSSM) predicts that at least one scalar Higgs boson (h^0) must have mass below about 135 GeV. The mass is controlled at tree-level by the Z-boson mass, and at one loop by the logarithm of superpartner masses. The prediction of a light Higgs boson has two virtues: it is a useful falsifiable test of the MSSM, and fits nicely within the upper bound from the current precision EW data. Over much of the parameter space, the light MSSM Higgs boson behaves very similarly to the SM Higgs boson.

The other physical scalar Higgs states of the MSSM are H^0, A^0, and $H^\pm$. Unlike the h^0 state, these Higgs bosons receive tree-level masses directly from supersymmetry breaking parameters. Therefore, it is not possible to rigorously establish upper bounds to their masses. In large parts of parameter space, the masses of these particles are above 300 GeV, and the only important production processes in e^+e^- annihilation are the pair-production reactions $e^+e^- \to H^+H^-, H^0A^0$. Thus, these particles may not appear at the first-stage linear collider.

If the heavy Higgs boson are not seen directly, the effects of the more complicated Higgs sector of the MSSM can be observed by measuring slight deviations in the couplings of h^0 to fermions and gauge bosons from those predicted for a SM Higgs

boson. The more massive the heavy Higgs bosons are, the more h^0 behaves like the SM Higgs boson. Nevertheless, inconsistency with the SM can be discerned by precision measurements at the LC over much of the parameter space, even when m_{A^0} is significantly higher than $\sqrt{s}/2$ and out of reach of direct production. This issue is discussed in Chapter 3, Section 8. It demonstrates again the importance of precision Higgs boson measurements to pointing the way to new physics at higher mass scales.

Probing supersymmetry breaking. Finally, precision measurements of supersymmetry masses and mixing angles serve a purpose beyond simply determining what Lagrangian applies to the energy region around the weak interaction scale. Careful measurements can reveal a pattern characteristic of a more fundamental theory. For example, masses measured at the weak scale can be evolved using the renormalization group to a higher scale, where they might be seen to be unified or to fit another simple relation. A pattern that emerged from this study would point to a specific theory of supersymmetry breaking, indicating both the mechanism and scale at which it occurs. This study could also support or refute the hypothesis that our world is derived from a perturbative grand unified theory with an energy desert, a hypothesis that does seem to apply to the precisely known gauge couplings measured at m_Z. The ability of a linear collider to test these tantalizing ideas with precision measurements provides a route by which we can climb from the weak scale to a more profound theory operating at much higher energies.

4 New strong interactions at the TeV scale

A second way to cure the stability crisis of the Higgs field and to explain the origin of electroweak symmetry breaking is to introduce a new set of strong interactions that operate at the TeV scale of energies. In models of this type, symmetry breaking arises in the weak interactions in the same way that it arises in well-studied solid-state physics systems such as superconductors. Just as in those systems, the physics responsible for the symmetry breaking has many other consequences that lead to observable phenomena at the energy scale of the new interactions.

Two quite distinct implementations of this line of thought have been actively pursued. The first follows the possibility that the Higgs doublet (*i.e.*, the four degrees of freedom which after electroweak symmetry breaking become the Higgs boson and the longitudinal components of the $W^\pm$ and Z^0) is a bound state that arises from a short-range strongly coupled force. Theories that have this behavior are generically called 'composite Higgs' models. These models are usually well approximated at low energies by the SM, and therefore are consistent with the electroweak data.

The second implementation follows the possibility that the new strong interactions do not generate a Higgs doublet, even as a bound state. This is possible if the

electroweak symmetry is broken by the pair-condensation of some new strongly interacting particles. The prototype of such theories is 'technicolor', an asymptotically-free gauge interaction that becomes strong at the TeV scale. The behavior of technicolor theories below the TeV scale is typically very different from that of the SM. In most cases, there is no Higgs boson with an observable coupling to pairs of Z bosons, and the new symmetry-breaking interactions generate substantial corrections to precision electroweak observables.

The linear collider experiments that directly test these two theoretical pictures are reviewed in detail in Chapter 5, Sections 3 and 4. In this section we briefly discuss the two ideas in general terms and discuss the relevance of the linear collider for uncovering and studying these new interactions.

4.1 Composite Higgs models

Several ways have been suggested in the literature to form a bound-state Higgs boson that mimics the properties of the Higgs particle of the SM. In the top-quark seesaw theory, the Higgs boson arises as a bound state of the left-handed top quark and the right-handed component of a new heavy vector-like quark. Although the composite Higgs boson mass is typically about 500 GeV, there is agreement with the precision electroweak data for a range of parameters in which new contributions from the additional heavy quark compensate the effects of a heavy Higgs boson. Depending on the binding interactions, an extended composite Higgs sector may form. In this case, mixing among the CP-even scalar bound states may bring the SM-like Higgs boson down to a mass below 200 GeV.

Another scenario that may lead to a composite Higgs boson is the SM in extra spatial dimensions, a case that we will discuss in more detail in the next section. Here the short-range strongly-coupled force is given by the Kaluza-Klein excited states of the $SU(3)_C \times SU(2)_W \times U(1)_Y$ gauge bosons. The Kaluza-Klein states of the top quark become the constituents of the Higgs boson. The Higgs boson in this scenario has a mass of order 200 GeV.

We now list a number of non-standard phenomena that are likely to appear in these theories at relatively low energies. Of course, these theories will ultimately be tested by going to the energy scale of the new interaction and determining its nature as a gauge theory or as a field theory of some other type.

Deviations in Higgs sector. In models in which the Higgs boson appears as a bound state, it is likely that additional composite scalar states will also be present at the TeV scale or below. If these states appear, their masses and couplings will provide important information on the nature of the constituents. Additional states with the quantum numbers of the Higgs boson can be produced at a linear collider in association with a Z^0 or singly in $\gamma\gamma$ collisions. Other states can be studied in pair-production. In both cases, the precise measurement of their masses and branching

ratios will provide important information. In addition, it is possible at a linear collider to recognize even very small deviations of the properties of the Higgs boson from the predictions of the SM.

Extra fermions. The top-quark seesaw model implies the existence of an additional fermion whose left- and right-handed components have the same charges as the right-handed top quark, t_R. This quark could have a mass of many TeV with little loss in fine-tuning, making it hard to find directly at any of the next generation colliders, including the LHC. In this circumstance, however, the improved precision electroweak measurements described in Chapter 8 should show a clear deviation from the SM in the direction of positive ρ parameter ($\Delta T > 0$). This would prove that the SM is incomplete and give a clue as to the nature of the new physics.

Heavy vector bosons. Both the top-quark seesaw theory and the extra-dimensional composite Higgs models imply the existence of heavy vector bosons. In the top-condensate scenario, the extra heavy vectors could arise from a topcolor gauge group. In addition, one often requires an additional gauge interaction that couples differently to t_R and b_R to explain why we see top quark but not bottom quark condensation. If a new vector boson couples with some strength to all three generations, it will appear as a resonance at the LHC, and its effects will be seen at the LC as a pattern of deviations in all of the polarized $e^+e^- \to f\overline{f}$ cross sections. In both cases, the experiments are sensitive to masses of 4 TeV and above. This mass reach overlaps well with the expectation that the new physics should occur at a mass scale of several TeV. The observation and characterization of new Z bosons are described in Chapter 5, Section 5.

4.2 Technicolor theories

Technicolor theories provide an alternative type of model with new strong interactions. These theories do not require a composite Higgs boson. Instead, they involve new chiral fermions and a confining gauge interaction that becomes strongly-coupled at an energy scale of order 1 TeV. The most robust prediction of these theories is that there is a vector resonance with mass below about 2 TeV that couples with full strength to the $J = 1$ W^+W^- scattering amplitude.

The general idea of technicolor is severely constrained by the precision electroweak measurements, which favor models with a light Higgs boson over models where this state is replaced by heavy resonances. In order to be viable, a technicolor model must provide some new contributions to the precision electroweak observables that compensate for the absence of the Higgs boson. This leads us away from models in which the new strong interactions mimic the behavior of QCD and toward models with a significantly different behavior. For such models, it is difficult to compute quantitatively and so we must look for qualitative predictions that can be tested at high-energy colliders. In this situation, the ability of the linear collider to discover new

particles essentially independently of their decay schemes would play an important role.

We summarize some of the measurements that the linear collider can perform that are relevant to strongly-coupled theories of this type. Our approach is to identify qualitative features that are likely to result from technicolor dynamics. Because of the uncertainties in calculating the properties of such strongly-interacting theories, it is not possible to map out for what parameters a given model can be confirmed or ruled out. Nevertheless, the linear collider has the opportunity to identify key components of technicolor models.

Strong WW scattering. As we have noted, the most robust qualitative prediction of technicolor theories is the presence of a resonance in WW scattering in the vector ($J = 1$) channel. This particle is the analogue of the ρ meson of QCD. For masses up to 2 TeV, the 'techni-ρ' should be seen as a mass peak in the W^+W^- invariant mass distribution observed at the LHC. In addition, the techni-ρ will appear as a resonance in $e^+e^- \to W^+W^-$ for longitudinal W polarizations, for the same reason that in QCD the ρ meson appears as a dramatic resonance in $e^+e^- \to \pi^+\pi^-$. The resonant effect is a very large enhancement of a well-understood SM process, so the effect should be unmistakable at the linear collider, even at $\sqrt{s} = 500$ GeV, well below the resonance. As with the case of a Z', the two different observations at the linear collider and the LHC can be put together to obtain a clear phenomenological picture of this new state. These issues are discussed further in Chapter 5, Section 3.

Anomalous gauge couplings. If there is no Higgs boson resonance below about 800 GeV, the unitarization of the $WW \to WW$ scattering cross-section by new strong interactions will lead to a large set of new effective interactions that alter the couplings of W and Z. Some of these terms lead to anomalous contributions to the $WW\gamma$ and WWZ vertices. Through the precision study of $e^+e^- \to W^+W^-$ and related reactions, the 500 GeV linear collider with 500 fb^{-1} of integrated luminosity will detect these anomalous contributions or improve the limits by a factor of ten over those that will be set at the LHC. In the case that there are new strong interactions, the accuracy of the linear collider measurement is such as to make it possible to measure the coefficients of the effective Lagrangian that results from the new strong interactions. These measurements are discussed further in Chapter 5, Section 2. In addition, many technicolor models predict large anomalous contributions to the gauge interactions of the top quark particularly to the $t\bar{t}Z$ vertex function. The linear collider may provide the only way to measure this vertex precisely. The measurement is discussed in Chapter 6, Section 3.

Extra scalars. Just as, in QCD, where the strongly coupled quarks lead to octets of relatively light mesons, technicolor theories often imply the existence of a multiplet of pseudoscalar bosons that are relatively light compared to the TeV scale. These

bosons are composites of the underlying strongly coupled fermions. Since these particles have non-zero electroweak quantum numbers, they are pair-produced in e^+e^- annihilation. The number of such bosons and their quantum numbers depend on the precise technicolor theory. Experimentally, these particles look like the particles of an extended Higgs sector, and their detection and study follow the methods discussed for that case in Chapter 2, Section 6. Particular models may include additional new particles. For example, in 'topcolor-assisted technicolor', there is a second doublet of Higgs bosons, with masses of 200-300 GeV, associated with top-quark mass generation.

5 Extra spatial dimensions

It is 'apparent' that the space we live in is three-dimensional, and in fact precise measurements are consistent with this even down to the small distances probed by LEP2 and the Tevatron. But one should not hastily conclude that the universe has no more than three dimensions, because two important loopholes remain. First, there could be extra spatial dimensions that are not accessible to SM particles such as the photon and the gluon. Second, there could be extra spatial dimensions that are compact, with a size smaller than 10^{-17} cm. In both cases, it is possible to build models that are in agreement with all current data.

Besides being a logical possibility, the existence of extra spatial dimensions may explain key features of observed phenomena, ranging from the weakness of the gravitational interactions to the existence of three generations of quarks and leptons. Most importantly from the viewpoint of the stability problem of the Higgs field, the assumption that the universe contains more that three dimensions opens a number of new possibilities for models of electroweak symmetry breaking. In such models, the value of the weak-interaction scale results from the fact that some natural mass scale of gravity in higher dimensions, either the size of the new dimensions or the intrinsic mass scale of gravity, is of order 1 TeV. This, in turn, leads to new observable phenomena in high energy physics at energies near 1 TeV. These phenomena, and the possibility of their observation at a linear collider, are discussed in Chapter 5, Section 6.

Once we have opened the possibility of new spatial dimensions, there are many ways to construct models. Most of the options can be classified by two criteria. First, we must specify which particles are allowed to propagate in the full space and which are restricted by some mechanism to live in a three-dimensional subspace. Second, we must specify whether the extra dimensions are flat, like the three dimensions we see, or highly curved. The latter case is referred to in the literature as a 'warped' geometry. Some ideas may require additional fields, beyond the SM fields, to solve certain problems (such as flavor violation or anomaly cancelation) that can arise from

the hypothesized configuration of particles in the extra-dimensional space. We now give a brief overview of these possibilities and the role of the linear collider in each scenario.

5.1 Flat extra dimensions, containing only gravity

The first possibility is that all of the particles of the SM—quarks, leptons, and Higgs and gauge bosons—are localized on three-dimensional walls ('3-branes') in a higher-dimensional space. Gravity, however, necessarily propagates through all of space. Higher-dimensional gravity can be described in four-dimensional terms by using a momentum representation in the extra dimensions. If these extra dimensions are compact, the corresponding momenta are quantized. Each possible value of the extra-dimensional momentum gives a distinct particle in four dimensions. This particle has mass $m_i^2 = (\vec{p}_i)^2$, where $\vec{p}_i$ is the quantized value of the extra-dimensional momenta. These four-dimensional particles arising from a higher-dimensional field are called Kaluza-Klein (KK) excitations. In the later examples, where we put SM fields also into the higher dimensions, these field will also acquire a KK spectrum.

If gravity propagates in the extra dimensions, the exchange of its KK excitations will increase the strength of the gravitational force at distances smaller than the size of the new dimensions. Then the fundamental mass scale M_* at which gravity becomes a strong interaction is lower than the apparent Planck scale of 10^{19} GeV. It is possible that M_* is as low as 1 TeV if the volume of the extra dimensions is sufficiently large. In that case, there is no stability problem for the Higgs field. The Higgs expectation value is naturally of the order of M_*.

The KK gravitons can be produced in collider experiments. In e^+e^- collisions, one would look for e^+e^- annihilation into a photon plus missing energy. The cross section for this process has typical electroweak size as the CM energy approaches M_* and the phase space for producing the KK gravitons opens up. The expected signals of extra dimensions are highly sensitive to the number of extra dimensions. Nevertheless, if the number of extra dimensions is less than or equal to six, the signal can be studied at a linear collider at CM energies that are a factor of 3–10 below M_*. The LHC can also study KK graviton production through processes such as $q\overline{q}$ annihilation to a jet plus missing energy. The sensitivity to M_* is somewhat greater than that of a 1 TeV linear collider, but it is not possible to measure the missing mass of the unobserved graviton.

The KK gravitons can also appear through their virtual exchange in processes such as $e^+e^- \to f\overline{f}$, $e^+e^- \to \gamma\gamma$, and $e^+e^- \to gg$. The graviton exchange leads to a spin-2 component that is distinct from the SM expectation. Although this indirect signal of KK gravitons is more model-dependent, it is expected that it can be seen even at 500 GeV if M_* is less than a few TeV.

5.2 Warped extra dimensions, containing only gravity

If the extra dimensions are warped, the KK spectrum of gravitons has somewhat different properties. In the case of flat extra dimension, the KK particles are closely spaced in mass, but in the case of warped dimensions, the spacing is of order 1 TeV. In the simplest model, the KK gravitons have masses in a characteristic pattern given by the zeros of a Bessel function. The individual states appear as spin-2 resonances coupling with electroweak strength to e^+e^- and $q\overline{q}$. These resonances might be seen directly at the LHC or at a linear collider. If the resonances are very heavy, their effects can be seen from additional spin-2 contact contributions to $e^+e^- \to f\overline{f}$, even for masses more than an order of magnitude above the collider CM energy.

5.3 Flat extra dimensions, containing SM gauge fields

It is often assumed that the quarks and leptons are localized on three-dimensional walls (3-branes) and therefore do not have KK modes, whereas the gauge bosons propagate in the extra-dimensional space. In this case, the KK modes of the electroweak gauge bosons contribute at tree level to the electroweak observables, so that a rather tight lower bound of about 4 TeV can be imposed on the inverse size of the extra dimensions. The LHC should be able to see the first gauge boson KK resonance up to about 5 TeV, leaving a small window of available phase space for direct production of these states. On the other hand, precision measurements at a high-energy e^+e^- linear collider can establish a pattern of deviations from the SM predictions for the reactions $e^+e^- \to f\overline{f}$ from KK resonances well beyond direct production sensitivities. The capability of an e^+e^- linear collider in identifying the rise in cross sections due to KK resonances improves when the center-of-mass energy is increased. High luminosity is also important. For example, with more than 100 fb^{-1} of integrated luminosity at a 500 GeV, one could see the effects of resonance tails for KK masses above 10 TeV in models with one extra dimension.

5.4 Flat extra dimensions, containing all SM particles

Finally, we consider the case of 'universal' extra dimensions, in which all SM particles are permitted to propagate. A distinctive feature of universal extra dimensions is that the quantized KK momentum is conserved at each vertex. Thus, the KK modes of electroweak gauge bosons do not contribute to the precision electroweak observables at the tree level. As a result, the current mass bound on the first KK states is as low as 300 GeV for one universal extra dimension. If the KK states do indeed have a mass in the range 300-400 GeV, we would expect to observe the states at the Tevatron and the LHC. The linear collider, at a CM energy of 800 GeV, would become a KK factory that produces excited states of quarks, leptons, and gauge bosons.

6 Surprises

Our brief discussion of pathways beyond the SM concentrated on three very different approaches that have been proposed to solve the conundrums of the SM. Although some of these ideas are more easily tested than others at the next-generation colliders, it is important to note that all three approaches have many new observable consequences. In all cases, we expect to see an explosion of new phenomena as we head to higher energies.

Though these three approaches are very different, we should not delude ourselves into thinking that they cover the full range of possibilities. Letting our imaginations run free, we could envision models in which quantum field theory itself breaks down at the weak interaction scale and an even more fundamental description takes over. Such a possibility would be viable only if it satisfies the constraint of giving back the predictions of the SM at energies below 100 GeV. String theory is an example of a framework that resembles the SM at low energies but, at the energies of the string scale, is dramatically different from a simple quantum field theory. Perhaps there are other alternatives to be found.

Exploring physics at shorter distances and with higher precision is an endeavor that implies the possibility of great surprises. Experiments at a linear collider will be a necessary and rewarding part of this program, and will constitute a major step in our quest to understand how Nature works.

Experimental Program Issues

Chapter 10 Scenarios for Linear Collider Running

In the literature on physics studies at e^+e^- linear colliders, one typically finds each process analyzed in isolation with a specific choice of energy and polarization. This naturally raises the question of how the full program for the linear collider fits together and whether all of the important physics topics can actually be scheduled and investigated. In this chapter, we will examine this issue. We will suggest some simple run plans that accomplish the most important goals of the linear collider program under different physics scenarios.

Under almost any scenario, one would wish to run the linear collider at two or more different energies during the course of its program. Operation of the collider at energies lower than 500 GeV typically yields lower luminosity, scaling roughly as $E_{\rm CM}$. In this chapter, we will craft scenarios using the following guidelines: We assume that the collider has a single interaction region that can run at any energy from m_Z to 500 GeV, with instantaneous luminosity strictly proportional to the CM energy. We plan for a campaign equivalent to 1000 fb^{-1} at 500 GeV, corresponding to 3–5 years at design luminosity. We then ask how the collider running should be allotted among the various possible conditions. These assumptions are rather simplistic, but they frame a problem whose solution is instructive. In Chapter 11, we describe in a more careful way how a collider with two interaction regions, sharing luminosity, would be configured for a flexible program covering a large dynamic range in CM energy.

1 Preliminaries

In designing a plan for linear collider running, we should consider the alternative strategies for energy and for polarization. In this paragraph, we consider these two topics in turn.

There are three different ways to choose the energy of an e^+e^- collider:

- *Sit:* Choose an energy that is optimal for a particular interesting process, and accumulate integrated luminosity at that point.
- *Scan:* Step through a threshold for pair-production of some particle, taking enough data to define the threshold behavior.
- *Span:* Go to the highest available energy, and take a large sample of data there.

In the application of e^+e^- colliders to the J/ψ and Υ systems, and to the Z^0, the e^+e^- annihilation cross section contained narrow structures that put great importance on

the exact choice of the beam energy. For most of the important processes considered for study at the next-generation linear collider, the choice of energy should be less of an issue, since the Higgs boson, the top quark, supersymmetric particles, *etc.*, will be studied mainly in continuum production of a pair of particles. These processes have cross sections that peak within 50–100 GeV of the threshold and then fall as $E_{\rm CM}^{-2}$. This dependence is somewhat compensated by the higher collider luminosity at higher energy. Since the signatures of different particles seen in e^+e^- annihilation are distinctive, many different reactions can be studied at a single energy.

As an example, consider the measurement of Higgs boson branching ratios. For this study, the Higgs boson is produced in the reaction $e^+e^- \to Z^0h^0$. For a Higgs boson of mass 120 GeV, the peak of the cross section is at 250 GeV. However, taking into account the increase of luminosity with energy, the penalty in the total number of Higgs bosons in working at 500 GeV instead of at the peak of the cross section is only a factor of 2. At higher energy, more reactions become accessible, and more effort must be made to isolate the Higgs sample. On the other hand, the Higgs production process has a distinctive signature, the monoenergetic Z^0. As the energy increases, the kinematics become more distinctive as the Higgs and the Z^0 are boosted into opposite hemispheres. We conclude that LC experimenters will continue to accumulate statistics for the Higgs branching ratio study as they move to higher energies. Thus, though concentration on this process would favor a sit at an energy below 300 GeV, one could well adopt a span strategy if other physics required it. This example illustrates that it is important, in future studies of linear collider measurements, to evaluate explicitly how the quality of the measurement depends on CM energy.

Only a few reactions among those anticipated for the LC require a detailed scan of some energy region. These include the measurement of the top quark mass by a threshold scan, the precision measurement of supersymmetric particle masses (to the parts per mil rather than the percent level), and, in the precision electroweak program of Chapter 8, the measurement of the W mass to 6 MeV. The top quark mass measurement actually becomes limited by theory errors after about 10 fb^{-1} of data, though a longer run would be justified to obtain a precision measurement of the top quark width and the decay form factors. Other threshold scans require similarly small increments of luminosity, except for the cases of sleptons, where the threshold turns on very slowly, as β^3, and the W, where extreme precision is required.

As for the choice of beam polarization in LC running, it is important to understand how polarization will be implemented. The choice of a polarized or unpolarized electron source is not a limiting factor for the electron currents in the machine. So there is no penalty in choosing a polarization that is as large as possible—80%, with current technology. Polarized electrons are created by shining circularly polarized light on an appropriate cathode. In the SLD polarization program at the Z^0, the polarized light was created by passing a linearly polarized laser beam through a Pockels cell, a device that is effectively a quarter-wave plate whose sign is determined

by an applied voltage. The signal applied to the cell changed sign randomly at the 120 Hz repetition rate of the machine. This random sign was supplied to the experimenters and used to determine the initial-state polarization in detected events. We anticipate that the beam polarization will be created in a similar way at the LC. Thus, there will be no 'unpolarized' running. The normal running condition will be a half-and-half mixture of left- and right-handed electron polarization, switching randomly at the repetition rate for bunch trains. In this arrangement, it is straightforward to measure polarization-averaged cross sections. The rapid switching allows polarization asymmetries to be measured with many systematic errors cancelling.

For certain processes, it is advantageous to take the bulk of the data in a single state of beam polarization. For example, the supersymmetric partners of the right-handed sleptons are most easily studied with a right-hand polarized electron beam, while WW pair production and fusion processes such as $W^+W^- \to t\overline{t}$ receive most or all of their cross section from the left-handed electron beam. In contrast, $e^+e^- \to Z^0h^0$ has only a weak polarization dependence. It is possible that our knowledge of physics at the time of the LC running will single out one such process as being of great importance and call for a run with an unequal (90%/10%) distribution of beam polarizations. As in the case of the energy choice, this is a shallow optimum, winning back, in the best case, less than a factor of 2 in luminosity.

2 Illustrative scenarios

With these considerations in mind, we now propose some sample run plans appropriate to different physics scenerios. For each plan, we quote the luminosity sample to be obtained at each energy and, in parentheses, the corresponding sample scaled to 500 GeV. These latter values are constrained to add up to 1000 fb^{-1}.

In most cases, the luminosity assigned below to 500 GeV would be accumulated at the highest machine energy if higher energies were available. Many physics issues, including the measurement of the Higgs coupling to $t\overline{t}$ and the Higgs self-coupling in addition to studies of new heavy particles, benefit greatly from CM energies above 500 GeV. The integrated luminosities given are totals, which might be accumulated in any order. In the scenarios presented here, we omit, for simplicity, the possibility of positron polarization and $\gamma\gamma$ or e^-e^- running. These options are discussed in the later chapters of this section. In considering any of these options, it is important to keep in mind that these options entail trade-offs against e^+e^- integrated luminosity.

2.1 A Higgs boson, but no other new physics, is seen at the LHC

In this case, we would want to apply a substantial amount of luminosity to a precision study of the branching ratios of the known Higgs boson. It will also be important to search for Higgs bosons not seen at the LHC, to search for new particles

with electroweak couplings that might have been missed at the LHC, and to measure the W and top gauge couplings to look for the virtual influence of new particles. Thus:

- 300 GeV: 250 fb^{-1} (420 fb^{-1}) sit
- 350 GeV: 100 fb^{-1} (140 fb^{-1}) top threshold scan
- 500 GeV: 440 fb^{-1} (440 fb^{-1}) span

This run plan gives a data sample for the Higgs boson branching ratio measurement equivalent to 600 fb^{-1} at 350 GeV.

2.2 No Higgs boson or other new particles are seen at the LHC

In this case, we would want to apply the largest amount of luminosity to the highest available energy. The issues for this study would be the search for additional Higgs bosons not seen at the LHC and the search for new particles. The measurement of the W and top gauge couplings would be of essential importance. Because the absence of a light Higgs conflicts with the precision electroweak fits within the SM, it will also be crucial in this case to include running at the Z^0 and the WW threshold.

- 90 GeV: 50 fb^{-1} (280 fb^{-1}) sit
- 160 GeV: 70 fb^{-1} (220 fb^{-1}) W threshold scan
- 350 GeV: 50 fb^{-1} (70 fb^{-1}) top threshold scan
- 500 GeV: 430 fb^{-1} (430 fb^{-1}) span

2.3 Light Higgs and superpartners are seen at the LHC

In this case, it is necessary to compromise between the optimal energies to study each of the new states, the optimal energy for the Higgs study—since a light Higgs must also appear in supersymmetric models—and searches for new superparticles, such as the extended Higgs particles and the heavier charginos and neutralinos, that could have been missed at the LHC. The program will begin with extended running at 500 GeV, and perhaps also at a lower energy, to determine the superpartner masses to percent-level accuracy. This could be followed by detailed threshold scans.

Martyn and Blair [1] have studied a particular scenario in which the lightest neutralino has a mass of 70 GeV, the lighter charginos and sleptons lie at about 130 GeV, and the heavier charginos and neutralinos are at about 350 GeV. Converting their suggested program to our rules, we have for this case:

- 320 GeV: 160 fb^{-1} (250 fb^{-1}) sit
- 500 GeV: 245 fb^{-1} (245 fb^{-1}) span
- 255 GeV: 20 fb^{-1} (40 fb^{-1}) chargino threshold scan
- 265 GeV: 100 fb^{-1} (190 fb^{-1}) slepton ($\ell_R^-\ell_R^+$) threshold scan
- 310 GeV: 20 fb^{-1} (30 fb^{-1}) slepton ($\ell_L^-\ell_R^+$) threshold scan
- 350 GeV: 20 fb^{-1} (30 fb^{-1}) top threshold scan
- 450 GeV: 100 fb^{-1} (110 fb^{-1}) neutralino ($\chi_2^0\chi_3^0$) threshold scan
- 470 GeV: 100 fb^{-1} (105 fb^{-1}) chargino ($\chi_1^-\chi_2^+$) threshold scan

The threshold scans would be done with the dominant beam polarization chosen, respectively, right, left, equal, left, left. The threshold with β^1 cross sections are given small amounts of running time; thresholds with β^3 cross sections or cross sections that are intrinsically small are given 100 fb^{-1}. The running time at the top threshold is more than sufficient to push the determination of m_t to the systematics limit. While running at each threshold, pair production of all lighter species can also be studied. In particular, the total statistics for the Higgs branching ratio measurement is equivalent to about 700 fb^{-1} at 350 GeV.

References

[1] H. Martyn and G. A. Blair, in *Physics and Experiments at Future Linear e^+e^- Colliders* (LCWS99), E. Fernandez and A. Pacheco, eds. (Univ. Auton. de Barcelona, Bellaterra, 2000), hep-ph/9910416.

Chapter 11 Interaction Regions

1 Introduction

The Standard Model has received considerable experimental attention in the past two decades, and much is known about its electroweak sector and about its flavor sector. Recent precision experiments have the sensitivity to look beyond the SM for new physics. However, the mechanism for symmetry breaking in the SM is still unknown, and many questions, such as the existence of SUSY, still are answered only by speculation. A future linear collider will provide the tools with which we may probe the mechanism of symmetry breaking and address the questions of new physics beyond the SM. We seek the best configuration of a linear collider facility that maximizes the potential for answering these questions.

The number of interaction regions is a very important issue, affecting the project cost, the physical footprint of the collider complex, the number of detectors that can be accommodated, the breadth of the physics program, and almost certainly the amount of enthusiasm and support the linear collider would receive in the world's high energy physics community. In this section we look at the nature and number of interaction regions to accompany the accelerator complex of a linear collider. The baseline configurations for TESLA and the NLC are briefly discussed here. This section gives only a brief overview of the technical designs. One must go to the relevant reports and documents to get more technical details.

Both the TESLA and the NLC designs for the IRs allow for two regions. The TESLA philosophy in its baseline design differs somewhat from that of the NLC. The baseline design for TESLA includes only one IR, with real estate available for a second IR and a second beam delivery system, if and when the funds become available. The NLC baseline design contains two IRs, as described below.

The arguments favoring the two-IR collider configuration come first from the physics program. The rich program of particle physics could best be investigated by two active IRs with two or more detectors. However, one must consider the trade-off between the increased breadth of the physics program and the increased costs incurred. One of the "costs" encountered is the unavoidable sharing of the available luminosity between the two IRs. Strategies for simultaneous running in the NLC are briefly discussed.

However, it should be pointed out that the strongest motivation for two IRs may come from external factors. The future linear collider will surely be an international facility. In order for there to be international participation in the financing of the collider, it would be wise to incorporate two IRs to facilitate broad participation

in the detectors and the experimental program. This philosophy on international participation in the linear collider is surely part of the strategy for incorporating two IRs in the TESLA and NLC designs.

2 The two interaction region design at TESLA

TESLA has provision for two IRs, one which is in the baseline design, and a second which is not currently in the baseline, but may be added. The TESLA linear collider cannot serve two IRs with luminosity simultaneously. It is possible, however, to switch the beam between the two experimental stations. The primary IR will receive beams at a zero crossing angle, while the secondary IR will have a crossing angle of 34 mrad. If the secondary IR is run in the e^+e^- collider mode (with crab crossing), it is anticipated to have the same luminosity as the primary IR. The crossing angle also makes the secondary IR suitable for $\gamma\gamma$ and $e\gamma$ collider modes of operation using backscattered laser beams, as described in Chapter 13. Electron-electron collisions are possible at one or both IRs, by reversing magnet polarities and providing a second polarized electron source. This option is discussed in Chapter 14. The layout of the two IRs and their technical parameters can be found in the TESLA TDR [1].

3 The dual-energy interaction region design at the NLC

To allow for a collider design for the desired physics program that extends from the Z-pole to many TeV, the NLC group has introduced a dual-energy IR design [2]. The first IR is in a direct line with the main linacs that accelerate the beams. The second IR is reached by bending the beam away from this direct line. Both IRs have crossing angles, as described below. The IRs would be designed to operate in different energy ranges, the first from 250 to 1000 GeV, the second from 90 to 500 GeV.

There are two motivations for this choice. First, by having one of the two IRs in a direct line with the main linacs that accelerate the beams, this IR can operate at multi-TeV energies in subsequent machine energy upgrades. This layout eliminates the bending where incoherent synchrotron radiation would dilute the beam emittances. Second, Final Focus beamlines are naturally optimized to operate over roughly a factor of four to five in beam energy. At the high end of the range, the luminosity decays rapidly due to increasing synchrotron radiation. At lower energies, the luminosity scales proportionally to the collision energy until a limit is reached at roughly 25% of the maximum energy. Below this limit, the luminosity decays as the square of the collision energy due to increasing aberrations and limited vacuum and masking apertures. At either end, a smoother dependence of luminosity on energy can be retained by realigning the Final Focus components to change the total bending.

The choices we have indicated, with two Final Focus systems of fixed configuration, give the NLC overlapping coverage of the energy region that is thought to be initially of interest.

Because the straight-ahead IR could support multi-TeV beam collisions, we refer to this as the 'high-energy' IR (HEIR). The bending required to reach the second IR limits the maximum energy attainable. Thus, we refer to this as the 'low-energy' IR (LEIR). Schematic plans of the NLC machine and the two-IR layout are shown in Figs. 11.1 and 11.2.

With this starting point, the collider layout is determined by the length of the beam delivery systems, the required transverse separation of the IRs, and the desired crossing angle in the interaction regions. Given the new Final Focus optics design which utilizes local chromatic correction, the Final Focus can be relatively short. The present NLC Final Focus design is 700 meters long. This length is sufficient up to 5 TeV in the center of mass. In addition to the Final Focus optics itself, there are diagnostic regions and beam collimation regions upstream of the IP. Depending on the operating mode, these regions could likely be shared. In the present NLC design, these regions are roughly 1300 meters long for a total beam delivery system length of 2 km per side. This length could be reduced; however it is relatively inexpensive and provides a conservative solution to the beam optics and the beam collimation problems.

To attain reasonable transfer efficiency of the rf to the beam in a normal conducting linear collider, the bunches must be spaced together very closely. In this case, both IRs must have a non-zero crossing angle to prevent interactions between bunches at satellite crossings. Typical values for the crossing angle could range from 6 mrad to 40 mrad. The larger angles result in easier beam extraction and IR integration but lead to more difficult tolerances. Simplifying the beam extraction is important if one believes that it is important to measure the beam energy spread and polarization after collision at the IP. The crossing angles allow for these measurements in the NLC but not at the primary IR at TESLA.

Without consideration of the extraction line, the minimum crossing angle is set by the 'multi-bunch kink' instability. At CM energies below 1.5 TeV, the minimum angle in a normal conducting design is roughly 2 mrad. However, studies of the CLIC 3 TeV IR suggest that a minimum crossing angle of 15 mrad is necessary at multi-TeV energies. For these reasons, a crossing angle of 20 mrad at the HEIR and between 20–40 mrad at the LEIR is suggested.

The IR halls have been sized assuming that one would house the NLC L or SD Detector and that one would house the P Detector. Table 11.1 gives a list of the hall parameters. The hall length (transverse to the beam) is large enough to allow assembly of the detector while a concrete wall shields the interaction point. The wall would also serve as radiation shielding if the detector is not deemed to be 'self-shielding'. If the detector were built in place on the beam line, and could be self-

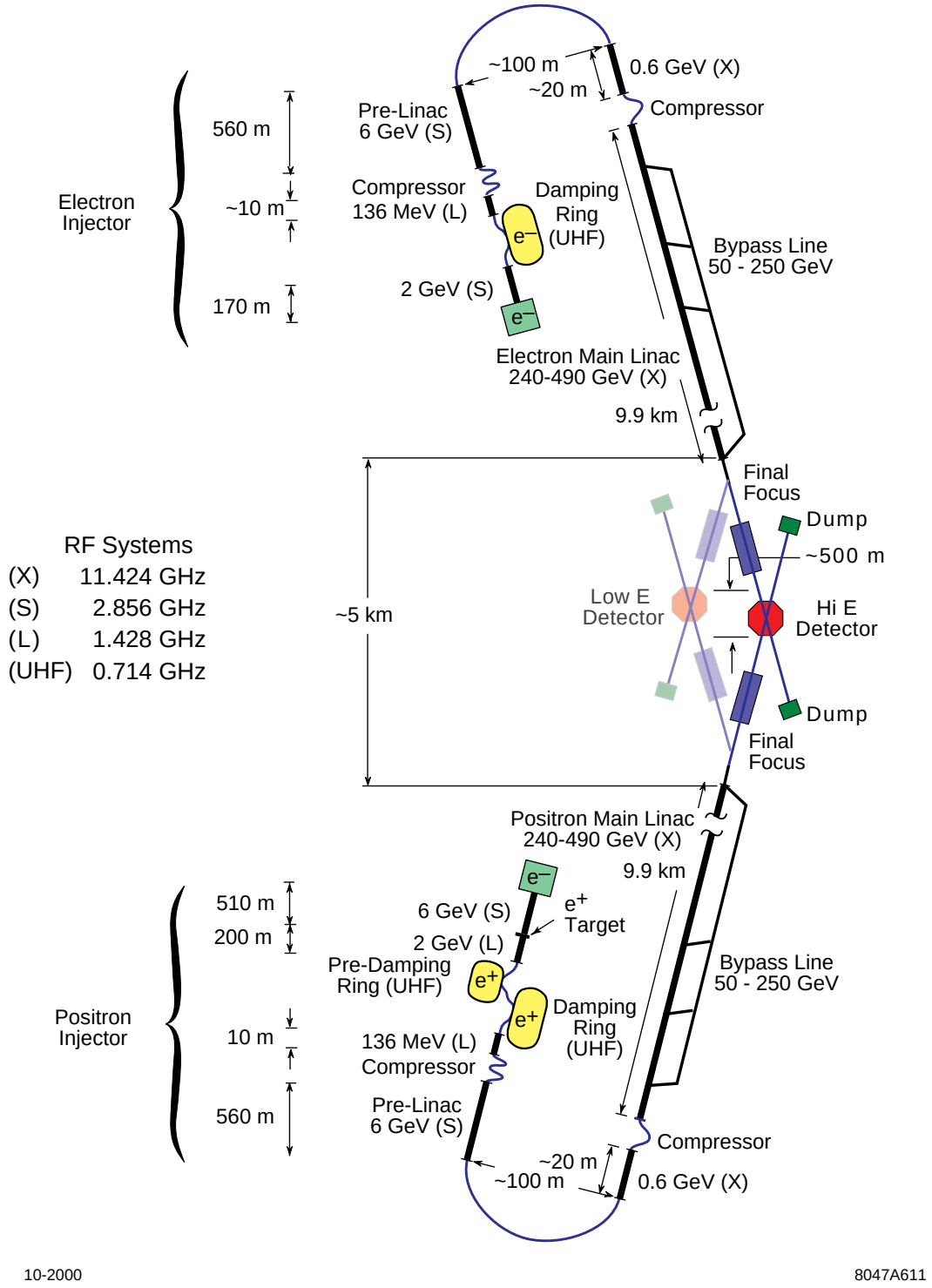

Figure 11.1: Schematic of the non-zero crossing angle of the two linacs and the Dual Energy IR layout.

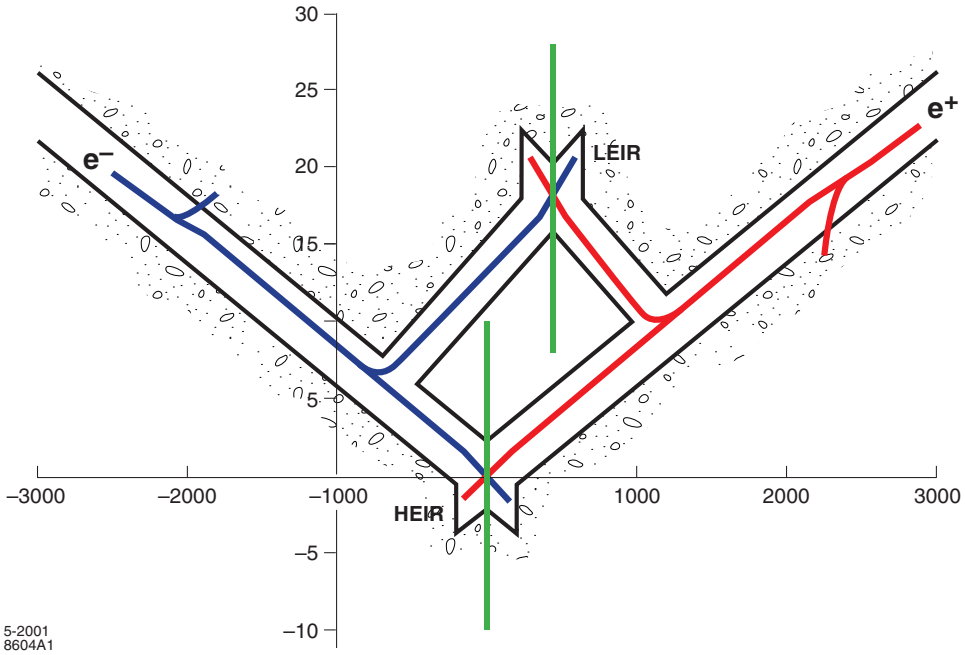

Figure 11.2: Schematic of the accelerator tunnels leading to the two interaction regions. The IRs are separated laterally by 25 m and longitudinally by 440 m. The crossing angles at the HEIR and LEIR are 20 mrad and 30 mrad, respectively. Note that the figure is extremely compressed in the horizontal direction; the detectors occupy the volume of the vertical rectangles that intersect the two beamlines at their crossing points.

shielding, the length could be reduced by roughly a factor of three. The hall width (parallel to the beamline) is set by the constraint that the doors open just enough to allow servicing of the inner detectors.

The baseline design assumes that the two IR halls are physically separated so that activities and mechanical equipment operating in one hall are seismically isolated from the other hall. For example, the LIGO facility has used 100 m as a minimum separation between rotating machinery and sensitive detectors. While the active detection and compensation of culturally induced ground vibration is a key element of the NLC R&D program, passive compliance with vibration criteria is the ideal. In principle each of the IR halls could be designed to accommodate two detectors that share the beamline in a push-pull manner, thus increasing experimental opportunities, or the overall NLC layout could be changed to support only one push-pull IR at a considerable cost savings. In any push-pull scheme, major installation activities might need to be curtailed if they introduced uncompensated vibration of the final magnets producing data for the detector currently on the beam line.

All of these features are illustrated in the schematic designs shown in Figs. 11.1 and

Parameter	Small Detector	Large Detector
Detector footprint	12 × 11 m	20 × 20 m
Pit length	40 m	62 m
Pit width	20 m	30 m
Pit depth below beamline	5 m	7 m
Door height	10 m	13 m
Door width	10 m	13 m
Barrel weight	2000 MT	7300 MT
Door weight	500 MT	1900 MT
Total weight	3100 MT	11100 MT

Table 11.1: The Baseline Interaction Region Parameters

11.2. The main linacs are aligned to provide the 20 mrad crossing angle at the HEIR. The LEIR beamline is bent from the straight-ahead beams. The transverse separation between the two IR collision points is currently set at roughly 25 meters. However, roughly 440 meters longitudinal separation of the two IR halls has been provided for increased vibration isolation. In addition, bypass lines are installed along the side of the linac so that lower-energy beams can be transported to the Final Focus without passing through the downstream accelerator structures.

3.1 The low-energy interaction region at the NLC

The experimental program in the LEIR is determined by the range of accessible center-of-mass energies and the available luminosity. The amount of luminosity that should be dedicated to a particular $\sqrt{s}$ will depend on the physics that is revealed by the Tevatron and the LHC. This need for flexibility imposes the requirement that the LEIR have high performance at least over the range $m_Z \leq \sqrt{s} \leq 2m_t$. Figure 11.3 shows the luminosity for the baseline design of the LEIR versus the center-of-mass energy. In the following, we outline the basic LEIR physics program as a function of increasing beam energy.

The lowest operating energy of the LEIR is determined by the requirement that high-statistics studies at the Z-pole be possible. The goal of a next-generation Z-pole experiment would be a significant reduction in the experimental errors in key electroweak parameters, as explained in Chapter 8. The success of this program relies on the availability of longitudinally polarized beams. Polarized electron beams will be available in the initial configuration. It would be desirable eventually to have positron polarization as well. Issues and technologies for positron polarization are discussed in Chapter 12. One feature pertaining to beam polarization in the LEIR is the need to account for the spin precession in the bends in the beam transport system. Another

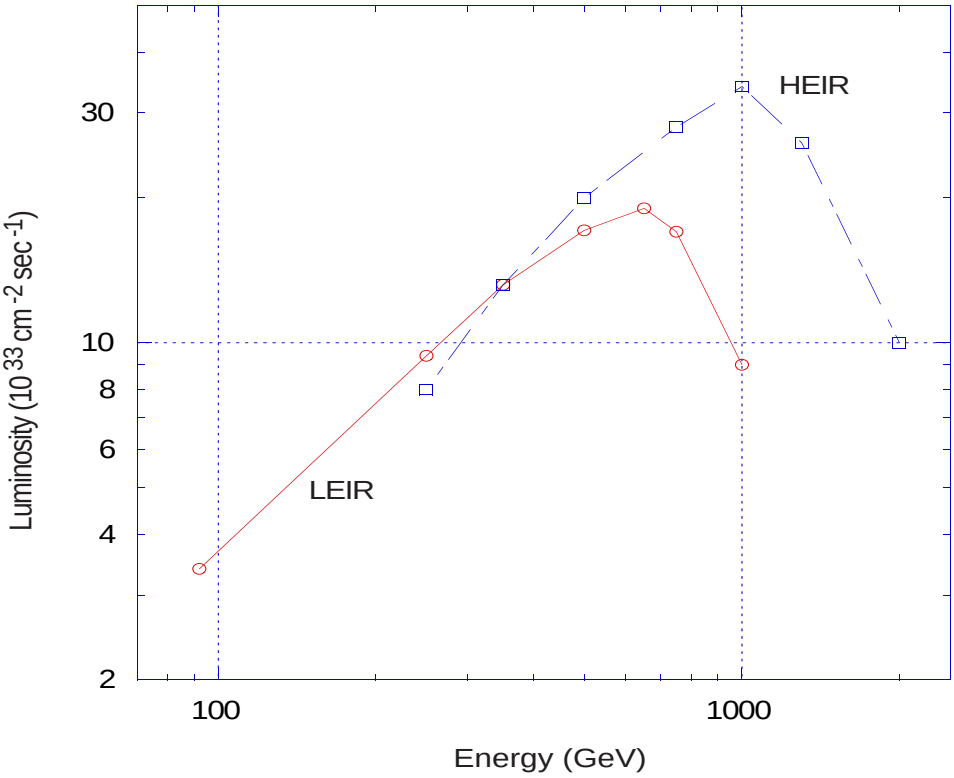

Figure 11.3: The baseline luminosity versus CM energy for the NLC LEIR and HEIR. The two IRs have been designed to have comparable performance in the region between 250 GeV and 500 GeV, however, the NLC HEIR beam delivery system has been optimized for a maximum energy of 500 GeV, the HEIR for 1 TeV.

issue is the desire to account for the depolarization that arises during collision. For this reason, a crossing angle is desirable, since it eases the polarization measurement after the IP.

Precise determination of the electroweak parameters could be particularly valuable in understanding the SM and physics beyond, particularly at a time when the Higgs boson mass is experimentally determined. In the event that only a single Higgs boson is observed with no other direct evidence of new physics from the LHC programs, the precision electroweak measurements will be a crucial aspect of the NLC program. A benchmark for such a program would be to accumulate a sample of 10^9 Z^0 decays.

The W-pair threshold occurs near $\sqrt{s} = 160$ GeV with the maximum production cross section at $\sqrt{s} \sim 200$ GeV. In the event that a significantly improved measurement of the W mass is required, it will be necessary to have dedicated running at the W-pair threshold. Studies have shown that an error on the W mass of 6 MeV would be obtainable with 100 fb^{-1}. Given the otherwise very limited physics program in

this energy range, the need for high instantaneous luminosity is evident.*

Beyond the W-pair threshold, it is highly likely that next benchmark center-of-mass energy will be the production cross section peak for a light Higgs boson. Precise measurements of the Higgs mass, width, spin-parity, and branching fractions are essential to help understand the role this object would play in electroweak symmetry breaking. The associated production process $e^+e^- \to Z^0h^0$, with $Z^0 \to \ell^+\ell^-$ and ℓ an electron or muon, provides a model-independent tag of Higgs production. The Higgs signal is easily identifiable in the dilepton recoil mass distribution. The maximum cross section for associated production occurs at roughly $m_Z + \sqrt{2}m_{\rm h}$. In minimal SUSY, the mass of the lightest CP-even scalar is required to satisfy $m_h \lesssim 135$ GeV. The precision electroweak fit to the SM calls for a Higgs boson with mass below 200 GeV. It is therefore essential that the LEIR design be capable of delivering high luminosity in the range $220 \lesssim \sqrt{s} \lesssim 340$ GeV. The study of a light Higgs boson will also benefit from control of the beam polarization; for example, for the measurement of the hWW coupling, one can exploit the large difference in the $\nu\overline{\nu}h^0$ production cross section for e^-_L and e^-_R beams. For some processes, positron polarization is also desirable. In many scenarios, the precision study of a light Higgs boson would be the principal focus of the LEIR program.

The $t\overline{t}$ threshold occurs near 350 GeV. The low-energy IR would be the natural facility to focus on this important topic. The threshold onset is a difficult process to study experimentally because of the resolution smearing caused by the natural energy spread from bremsstrahlung in the initial state, and from energy spread in the linear collider. The amount of dedicated running at the $t\overline{t}$ threshold will be dictated by the Higgs physics program. If a light Higgs is present, $m_H \lesssim 180$ GeV, it may be desirable to run below the $t\overline{t}$ threshold to control physics backgrounds and to optimize the Higgs production rate. For the case where the physics of electroweak symmetry breaking has conspired to produce a heavy Higgs boson that somehow satisfies the precision constraints, the study of the top quark properties will assume a central importance. The integrated luminosity requirements for the LEIR at or above the $t\overline{t}$ threshold in such a scenario will be the order of 100 fb^{-1} necessitating instantaneous luminosities of at least 5×10^{33} cm^{-2}s^{-1}.

Other physics options for the low-energy IR have been considered extensively. The region would serve well as the location for a 'second generation' detector for $\gamma\gamma$ collisions. Similarly, an e^-e^- program might be done in the LEIR, should the physics motivations lead in this direction.

In summary, a low-energy IR has many uses and advantages in an NLC program. It would provide considerable flexibility in the physics program, and would preserve many physics opportunities in scenarios in which the NLC is upgraded to multi-TeV

*Although investigation of W-boson properties will be an important goal of any NLC program, many of these studies, *e.g.*, the determination of Triple Gauge Boson couplings, are best performed at the highest achievable center-of-mass energy. This issue is discussed in Chapter 5, Section 2.

operations for high-energy studies in the other IR region.

3.2 The high-energy interaction region at the NLC

The design of the NLC allows for an IR region capable of upgrading to multi-TeV operations in an energy-upgraded NLC. To assure this possibility, the beam delivery systems are aligned in a straight-ahead configuration relative to their respective linacs, with very little bending of the incoming beams between the linear accelerator structure and the IR. To preserve the non-zero crossing angle required at the point of collisions, the two halves of the collider structure are not parallel but rather cross at an angle at the collision point. Figure 11.3 shows the luminosity versus CM energy for the baseline design of the HEIR.

The HEIR physics program is intimately related to the scenario that is realized in Nature for electroweak symmetry breaking. In the event that supersymmetry is discovered, the focus of the HEIR program will be the measurement of sparticle properties. It is unlikely that the full SUSY spectrum will be accessible at $\sqrt{s} = 500$ GeV; therefore, the energy reach of the HEIR should be upgradable to the multi-TeV region. Symmetry-breaking arising from some new strong dynamics would also be likely to put a premium on the energy reach. It is clear that in comparison to the LEIR, the physics requirements for the HEIR are, to first order, straightforward: the highest possible luminosity at the highest possible energy.

The energy span of the HEIR runs from 250 GeV to 500 GeV in the initial phase. Therefore the physics program can in principle include everything from 250 GeV on up, a region which overlaps in energy with the LEIR. Studies of W-pairs, low-lying SUSY states, and the $t\bar{t}$ threshold could occur in the HEIR. Although, in the case of a light Higgs boson, much of the precision Higgs physics could be performed at the LEIR, there is Higgs physics unique to the HEIR. For a light Higgs boson consistent with the current theoretical and experimental constraints, the maximum cross section for the rare process $e^+e^- \to Z^0h^0h^0$ occurs at $\sqrt{s} \sim 500$ GeV. This process is of great interest, since it enables measurement of the Higgs self-coupling which in turn can be related to the shape of the Higgs potential. The W-fusion process, $e^+e^- \to \nu\overline{\nu}h^0$, which is sensitive the hWW vertex, has a cross section that increases with center-of-mass energy. The measurement of the Higgs self-coupling sets a benchmark for the accelerator performance. Depending on the exact mass, a measurement of this quantity requires integrated luminosities the order of 1000 fb^{-1}, which corresponds to 3–4 years at design luminosity.

Supersymmetry is a primary candidate for physics beyond the SM. Almost all versions of SUSY models result in low-lying states that would appear in e^+e^- annihilations below 500 GeV. Although the discovery phase for SUSY is likely to occur at the Tevatron or LHC, the NLC will play a key role in the detailed study of the sparticle spectrum and subsequent delineation of the soft SUSY-breaking Lagrangian.

To exploit fully the physics potential of the NLC, a number of special operating conditions may be necessary for the HEIR. For example, in EWSB models with extended Higgs sectors, of which SUSY is the most widely studied, a $\gamma\gamma$ mode of operation for the HEIR may be crucial. For example, the $\gamma\gamma$ mode enables production of a single Higgs boson; for the case of a nominal 500 GeV center-of-mass, this would effectively increase the mass reach from 250 GeV to 400 GeV for production of heavy neutral Higgs particles. Operation with transversely polarized photon beams allows separate production of the CP-even and CP-odd states. Control of the electron and positron beam polarization will also be extremely useful. For Higgs physics it can be used to increase the nominal production cross section for the self-coupling measurement. Beam polarization will also be useful in unraveling gaugino and slepton mixing. The need for an e^-e^- operating mode may be necessary to decipher selectron production.

It is likely and perhaps desirable that there be a staged evolution of the HEIR center-of-mass energy. Although the goal of the initial phase of the NLC is 500 GeV for the HEIR, it may be possible to start physics earlier at a lower collision energy. An intermediate commissioning stage with $\sqrt{s} \sim 250$ GeV and modest luminosity could potentially be very relevant and exciting, especially if direct evidence from the LHC indicated the production of a light Higgs boson or a threshold for supersymmetric states. Another obvious commissioning stage could be the $t\bar{t}$ threshold at 350 GeV. Even at 10% of design luminosity, the physics program promises to be rich. For example, dedicating 10 fb^{-1} to a scan of the $t\bar{t}$ threshold would already lead to a top quark mass measurement with a 200 MeV error, as discussed in Chapter 6, Section 2.

3.3 Alternative interaction region scenarios

The baseline scenario that we have assumed considers two interaction regions—a high-energy region limited only by the available accelerating structures and a second region that is limited in energy or by the support of $\gamma\gamma$ or other options. It is appropriate to discuss alternative scenarios and the interplay between the physics programs of the high- and low-energy interaction regions. The issue is complicated by the diversity of physics scenarios that may arise. An additional consideration is the possible staging of the maximum center-of-mass energy. The possibilities can be broadly classified into types:

a) Single interaction region with one detector;

b) Single interaction region with two detectors;

c) Two interaction regions, high-energy and low-energy;

d) Two high-energy interaction regions.

For scenario (a), there is an obvious cost advantage; however, the NLC physics program could be unduly compromised. The physics program would be tightly coupled to the available center-of-mass energy. Depending on the details of the actual physics scenario, it may not be possible to simultaneously satisfy the various needs of a diverse user community. The resolution of mutually exclusive requirements for luminosity and choice of the center-of-mass energy may not be straightforward.

It is difficult to identify the merits of scenario (b), given the limitations of a single IR outlined above for scenario (a). Given that the total luminosity accumulated by both experiments will be comparable to that for a single experiment, this scenario would only be of interest if the two detectors were of sufficiently different capabilities or there were very strong sociological arguments for a second collaboration. One possible scenario where differences between detectors could arise is if there were a need to have a dedicated $\gamma\gamma$ collider program. In such a scenario, it would be more natural to consider a push-pull capability for one of the IRs in a two-IR facility. The two IR regions allow for a push-pull configuration in a least one of the two regions. The footprint of the push-pull IR hall must not infringe on the beamline of the adjacent region. In addition, access to the detector captured between the two beamlines must be possible, and adequate shielding must be provided to permit work in the IR hall when beams are alive in the machine. Scenarios for staging two detectors would have to be considered and understood. These are complicated issues that would involve assumptions that might not be appropriate at a future date. Nevertheless, provision for staging two detectors in a push-pull configuration would be a low-cost and effective means to keep open future possibilities for a unique and special-purpose detector.

The scenario that has been chosen as the baseline is (c); there are a number of considerations in its favor. It makes it possible to have parallel physics programs running simultaneously, a clearly desirable feature. The upgrade path for the HEIR is less complex. It provides for a lower-energy IR that can be dedicated to precision studies of the Higgs boson, Z-pole or $t\bar{t}$ system. Moreover, in this scenario both the HEIR and LEIR will cover the preferred energy range for the study of a light Higgs. The two-IR design adds a degree of flexibility that enables the NLC to address essentially any physics scenario that could arise.

The scenario (c) affords a natural context for energy staging. As mentioned in Section 2.2, staging the HEIR energy at the beginning of the NLC program would make it possible to perform an initial investigation of the region above 250 GeV. Commissioning of the LEIR program might follow the completion of the full complement of accelerating structures required to reach 500 GeV though, with a bypass line, this might alternatively begin before the accelerator is complete. Many of the high-luminosity measurements foreseen for the LEIR would benefit from longitudinally polarized positron beams, which are not likely to be available at the initial stages of running.

Given the need to have minimal bending in the beam delivery system in order to preserve beam emittances, scenario (d), which has two high-energy IRs of similar performance, becomes technically challenging and more costly. Given the interest exhibited by many members of the physics community in the low-energy potential of the NLC, and the need to perform high-statistics studies of the Z-pole in a number of physics scenarios that could arise, it would seem prudent to have at least one IR capable of delivering that physics.

3.4 Simultaneous operation

The NLC design has in it the capability for simultaneous operations in the two IRs. In the baseline design, the accelerator delivers bunch trains at a rate of 120 Hz. With pulsed magnets, the beams can be sent alternately to two IRs, resulting in an even split of 60–60 Hz. Uneven splitting of the 120 pulses per second is technically more challenging, and is not envisioned as an option.

A higher pulse rate in the NLC is possible, but is not in the baseline design. It appears technically feasible, for example, to operate at 180 Hz. This would require modifications to the damping rings and additional cooling for the klystrons and modulators in some regions of the accelerator. But these changes would allow operation, for example, with 60 Hz of low-energy beams in the LEIR and 120 Hz of beams in the HEIR. This mode of operation would clearly enhance the experimental program and augment the total luminosity delivered to the experimenters.

References

[1] TESLA Technical Design Report, http://tesla.desy.de/new_pages/TDR_CD/start.html

[2] US NLC Collaboration, *2001 Report on the Next Linear Collider*, FERMILAB–Conf–01/075–E, LBNL–47935, SLAC–R–571.

Chapter 12 Positron Polarization

1 Introduction

The baseline designs for NLC and TESLA include a polarized electron beam, but the positron beam is unpolarized. In this chapter, we investigate the physics merits of positron polarization and summarize the status of proposed polarized positron source designs. These questions have also been discussed in [1].

The importance of electron beam polarization has been demonstrated in Z^0 production at the Stanford Linear Collider (SLC), where 75% electron polarization was achieved. This level of electron polarization provided an effective luminosity increase of approximately a factor of 25 for many Z-pole asymmetry observables. In particular, it allowed the SLD experiment to make the world's best measurement of the weak mixing angle, which is a key ingredient for indirect predictions of the SM Higgs mass. The electron polarization at SLC also provided a powerful tool for bottom quark studies, providing a means for b and $\overline{b}$ tagging from the large polarized forward-backward asymmetry, and for studies of parity violation in the $Zb\overline{b}$ vertex. At a 500 GeV linear collider, electron polarization will increase sensitivity to form-factor studies of W^+W^- and $t\overline{t}$ states, control the level of W^+W^- backgrounds in new physics searches, provide direct coupling to specific SUSY chiral states, and enhance sensitivity to new physics that would show up in the spin-zero channel.

But what will positron polarization add? First, the presence of appreciable positron polarization is equivalent to a boost in the effective electron polarization. Measured asymmetries that are proportional to the polarization will increase; fractional errors in these quantities will accordingly decrease. Second, cross sections for many processes will grow. Any process mediated by gauge bosons in the s-channel naturally wastes half the incident positrons. Left-handed electrons, for example, only annihilate on right-handed positrons. The same is true for t-channel exchanges with unique handedness in their couplings, such as neutrino exchange in W-pair production. By polarizing the positrons and coordinating their polarization with that of the electrons, the cross sections for these processes can double (in the limit of 100% polarization). Finally, polarimetry will benefit from positron polarization. As the effective polarization increases, its error decreases, allowing measurements with very small systematic errors. Such small errors are needed for high-precision work at the Z pole and will benefit studies of production asymmetries for W^+W^-. And, by using measurements of rates with all four helicity states (RL,LR,RR,LL) the beam polarizations can be inferred directly without additional polarimetry.

What positron polarization can bring, poor yields of polarized positrons can take

away, so the yield of any source of polarized positrons is very important. Several schemes have been advanced for polarizing positrons. All are ambitious, large systems which are mostly untested. R&D is required before decisions are made about how and when to include positron polarization in linear collider design.

2 The physics perspective

2.1 The structure of electroweak interactions at high energies

The primary purpose of a linear collider will be to study the mechanism of electroweak symmetry breaking (EWSB). Beam polarization at a high-energy linear collider can play an important role in this endeavor because: (1) the electrons and positrons in the beams are essentially chirality eigenstates; (2) gauge boson interactions couple $e^-_L e^+_R$ or $e^-_R e^+_L$ but not $e^-_L e^+_L$ or $e^-_R e^+_R$; and (3) the $SU(2)_L$ interaction involves only left-handed fermions in doublets, whereas right-handed fermions undergo only hypercharge $U(1)_Y$ interactions. At typical LC energies, where masses are small compared to $\sqrt{s}$, one can replace the exchange of γ and Z bosons with the B and W^3 bosons associated with the unbroken $U(1)_Y$ and $SU(2)_L$.

As a concrete application of these points, consider $e^+e^- \to W^+W^-$ production, which is a background to many new physics searches. There are three tree–level Feynman diagrams for this process, one involving the t-channel exchange of ν_e and the others involving the s-channel exchange of γ and Z. The polarization choice $e^+e^-_R$ will eliminate the first contribution, since W bosons have only left-handed interactions. Decomposing the s-channel diagrams into a W^3 and a B contribution, the W^3 diagram is also eliminated using e^-_R polarization for the same reason. The only remaining diagram now vanishes for symmetry reasons—the B and W bosons involve different interactions and do not couple to each other. In reality, there is a small but non-vanishing component to W^+W^- production, because of EWSB. The polarization choice e^+_R would eliminate this background at tree-level. Of course, it also important to consider the behavior of the signal process under the same choices of polarization and the fact that 100% beam polarization is difficult in practice.

In the example above, note how the polarization of only one beam had a dramatic effect. Once the electron polarization was chosen, only certain positron polarizations contributed. One can imagine also the case where the desired effect is to enhance the W^+W^- signal. Then, by judiciously choosing the polarization combination $e^-_L e^+_R$, the production rate is enhanced by a factor of four relative to the unpolarized case, and a factor of two beyond what is possible with only electron polarization. When either searching for rare processes or attempting precision measurements, such enhancements of signal and depletions of background can be quite important.

We use the convention that the sign of polarization is *positive* for *right-handed* polarization, both for electrons and for positrons. Then, for example, for the case of

single gauge boson production, the production cross section is proportional to

$$(1-\mathcal{P}_-)(1+\mathcal{P}_+)c_L^2+(1+\mathcal{P}_-)(1-\mathcal{P}_+)c_R^2, \tag{12.1}$$

where c_L and c_R are chiral couplings. Equation (12.1) is at the heart of the forward-backward asymmetry that arises when $c_L \neq c_R$. If two measurements of the cross section are made with a different *sign* for the polarizations $\mathcal{P}_-$ and $\mathcal{P}_+$, then the difference of the two measurements normalized to the sum is:

$$\frac{N_L-N_R}{N_L+N_R} \quad = \quad \mathcal{P}_{\rm eff}\frac{c_L^2-c_R^2}{c_L^2+c_R^2} \quad \equiv \quad \mathcal{P}_{\rm eff}A_{LR}, \tag{12.2}$$

where

$$\mathcal{P}_{\rm eff}=\frac{\mathcal{P}_- - \mathcal{P}_+}{1-\mathcal{P}_-\mathcal{P}_+}\ . \tag{12.3}$$

In Z boson production, A_{LR} depends on the difference between $1/4$ and $\sin^2\theta_W$. Since the error in an asymmetry A for a fixed number of events $N = N_L + N_R$ is given by $\delta A = \sqrt{(1-A^2)/N}$, increasing $\mathcal{P}_{\rm eff}$ makes measurable asymmetries larger and reduces the error in the measured asymmetry significantly if A^2 is comparable to 1. When only partial electron polarization is possible, a small positron polarization can substantially increase $\mathcal{P}_{\rm eff}$, while also decreasing systematic errors. These asymmetry improvements utilizing polarized positrons are exploited in the Giga-Z mode for a linear collider. With Giga-Z, polarized positrons are needed to take full advantage of the large statistics possible at a linear collider—50 times more data than the integrated LEP-I data sample and 2000 times more data than SLD's sample. With a Giga-Z data sample, one expects to achieve a factor of 20 improvement over SLD's A_{LR} and A_b measurements. These improved measurements can be used to perform exquisite tests of the Standard Model. Together with a precise measurement of the top quark mass (to 100 MeV from a threshold scan at a linear collider), the A_{LR} measurement can be used to predict the Standard Model Higgs mass to 7%. The Giga-Z program is discussed in more detail in Chapter 8.

Equation (12.1) is also applicable to other situations. In general, as long as a process has a helicity structure similar to that of s-channel gauge boson production, the rate is

$$(1-\mathcal{P}_-\mathcal{P}_+)\sigma_{\rm unpol}\left(1+\mathcal{P}_{\rm eff}\frac{c_L^2-c_R^2}{c_L^2+c_R^2}\right), \tag{12.4}$$

where $\sigma_{\rm unpol}$ is the unpolarized cross section. Notice that polarization can increase the cross section by at most a factor of four, as can occur for W^+W^- production where $c_R \simeq 0$.

2.2 Standard Model-like Higgs boson

One process of particular interest for a LC is Higgs boson production. The primary modes at a LC are associated production with a Z boson (Zh) and vector boson fusion ($\nu\overline{\nu}h$). The Zh process is particularly simple, since the direct coupling of the Higgs boson to electrons is negligible. Polarization effects appear only at the initial e^+e^-Z vertex. The Z process allows for the discovery and study of a Higgs boson with substantial couplings to the Z boson independently of the Higgs boson decay mode, using the Z recoil method. Therefore, the relative size of signal and background is of great interest.

		$\sigma(Zh)$ $c_L^2 = .58$ $c_R^2 = .42$		$\sigma(ZZ)$ $c_L^2 = .65$ $c_R^2 = .35$		$\sigma(W^+W^-)$ $c_L^2 \simeq 1$ $c_R^2 \simeq 0$	
		$E = 1$	$E = .8$	$E = 1$	$E = .8$	$E = 1$	$E = .8$
$\mathcal{P}_-$	$\mathcal{P}_+$	$P = 1$	$P = .6$	$P = 1$	$P = .6$	$P = 1$	$P = .6$
0	0	1	1	1	1	1	1
$+E$	0	0.84	0.87	0.69	0.75	0	0.2
$-E$	0	1.16	1.13	1.31	1.25	2	1.8
$+E$	$-P$	1.68	1.26	1.37	1.05	0	0.08
$-E$	$+P$	2.32	1.70	2.62	1.91	4	2.88

Table 12.1: Behavior of various Standard Model cross sections relevant for Higgs boson studies as a function of polarization for full and partial electron and positron polarization. The numbers listed are normalized to the unpolarized cross section.

At tree-level, the Zh cross section depends on polarization as indicated in Eq. (12.1) with the couplings $c_L = -\frac{1}{2} + \sin^2\theta_w$, $c_R = \sin^2\theta_w$. Numerically, the two squared coupling factors appear with the relative weights (normalized to unity) 0.58 to 0.42. Table 12.1 shows the relative behavior of the Zh cross section for full (100%) and partial electron (80%) and positron (60%) polarization. Even for partial polarization, a substantial increase to the production cross section occurs over the unpolarized case. Other Higgs boson production processes, such as $e^+e^- \to HA$ in the MSSM or $e^+e^- \to Zhh$ in the SM or MSSM (relevant for measuring the Higgs self-coupling), proceed through the Z resonance and have the same chiral structure.

Significant backgrounds to the Zh search can arise from W^+W^- and ZZ production. The polarization dependence of these processes is also shown in Table 12.1. The physics of the W^+W^- background was discussed previously. It is relevant to note from Table 12.1 that without full polarization—which may be difficult to obtain in practice—the W^+W^- background cannot be fully eliminated. On the other hand, the partial polarization of both beams can approximately recover the benefits of full polarization, since the effective polarization $\mathcal{P}_{\text{eff}}$ is close to 1. Another potential

background, ZZ production, has a similar behavior as the signal Zh, except that an additional Z must be attached to the incoming e^+e^-. Therefore, the relative weight of the different polarization pieces goes as the square of those for Zh production. For the case of partial polarization of both beams and ($\mathcal{P}_- = +80\%, \mathcal{P}_+ = -60\%$), where the W^+W^- background is substantially decreased, there is a small increase in $\sigma(Zh)/\sigma(ZZ)$. The efficacy of polarization will depend on the most significant background. Note that for a Higgs boson mass that is significantly different from m_Z, propagator effects and non-resonant diagrams need to be included, but the results should not be significantly different from those shown here.

The other Higgs production process of interest is WW fusion, which has a similar behavior to the WW background. When operating at energies where Zh and WW fusion are comparable, polarization can be used to dial off the fusion contribution. This may be important for the study of inclusive Higgs production using the recoil technique.

2.3 Supersymmetric particle production

The production and study of new particles with electroweak quantum numbers should be the forte of a linear collider, where the major backgrounds are also electroweak in strength. Supersymmetry is a concrete example of physics beyond the SM that predicts a spectrum of new electroweak states related to the SM ones by a spin transformation. We now discuss some aspects of supersymmetry measurements affected by beam polarization. For further discussion of supersymmetry mass and coupling measurements, see Chapter 4.

2.3.1 Slepton and squark production

One of the simplest sparticle production processes to consider is $\widetilde{\mu}$ pair production, where the interaction eigenstates $\widetilde{\mu}_R$ and $\widetilde{\mu}_L$ are expected to be nearly mass eigenstates. Gauge bosons couple to the combinations $\widetilde{\mu}_R\widetilde{\mu}_R^*$ and $\widetilde{\mu}_L\widetilde{\mu}_L^*$. $\widetilde{\mu}_R$ has only couplings to the hypercharge boson B. The initial e^+e^- state has different hypercharge depending on the electron polarization: e_L^- has $Y = -1/2$, whereas e_R^- has $Y = -1$. The production cross section depends on Y^2 and thus is four times larger for e_R^- than for e_L^-. Furthermore, the choice e_R^- significantly reduces the background from W^+W^- production, which comes both from decays to $\mu^+\nu_\mu\mu^-\overline{\nu}_\mu$ and from feed-down from decays to τ. Since $e_R^-e_R^+$ components do not contribute to the signal, left-polarizing the positron beam doubles the signal rate. $\widetilde{\mu}_L$ pair production depends on both B and W^3 (γ and Z) components. Switching the electron polarization will emphasize different combinations. In all, a judicious choice of the positron polarization will make more efficient use of the beam, increase the cross section, and suppress the backgrounds.

For third-generation sparticles such as $\widetilde{\tau}$ and $\widetilde{t}$, there may be significant mixing between the mass and interaction eigenstates, leading to new observables. As for the $\widetilde{\mu}$ case, the production cross section itself is sensitive to the electron polarization. However, increased sensitivity to the mixing may be obtained from a measurement of the left-right asymmetry. For $\widetilde{t}$ production, the addition of 60% polarization in the positron beam increases the accuracy of the mixing angle measurement by 25%, while decreasing systematic errors [2]. Of course, the former effect can be achieved with only e^- polarization by increasing the integrated luminosity.

Selectron production may benefit more from positron polarization because of the e^+e^- initial state at a LC. The exchange of neutralinos $\widetilde{\chi}^0$ in the t-channel introduces more structure beyond the s-channel exchange of γ and Z. The processes $e^-_L e^+_L \to \widetilde{e}_L \widetilde{e}^*_R$ and $e^-_R e^+_R \to \widetilde{e}_R \widetilde{e}^*_L$ proceed through $\widetilde{\chi}^0$ exchange only. Considering the case that $\widetilde{e}_L$ and $\widetilde{e}_R$ are close in mass, the polarization of both beams can play an essential role in disentangling the different interaction states. For example, $e^-_L e^+_L$ polarization will only produce the negatively-charged $\widetilde{e}_L$ and the positively-charged $\widetilde{e}^*_R$. Switching the polarization of both beams will produce only negatively-charged $\widetilde{e}_R$ and positively-charged $\widetilde{e}^*_L$. Since the endpoints of the lepton spectrum can be used to reconstruct the selectron and neutralino masses, the electrons and positrons yield separate information about $\widetilde{e}_L$ and $\widetilde{e}_R$. Without the positron polarization, one would always have contamination from $\widetilde{e}_L \widetilde{e}^*_L$ and $\widetilde{e}_R \widetilde{e}^*_R$ production. Conversely, the observation of the switch from one species to another with the change in positron polarization would give more weight to the SUSY interpretation of the events. The study of t-channel exchange in selectron production is an important method for studying neutralino mixing, since the components of the neutralinos that are Higgsino-like do not contribute. Therefore, it is valuable to be able to isolate the t-channel exchanges experimentally by using polarization.

2.3.2 Chargino and neutralino production

The study of chargino pair production $e^+e^- \to \widetilde{\chi}^-\widetilde{\chi}^+$ gives access to the parameters M_2, μ, $\tan\beta$, $m_{\widetilde{\nu}_e}$. It is conservative to assume that only the lightest chargino is kinematically accessible. In this case, studies have considered the case of extracting the SUSY parameters from the measurement of cross sections for full $e^-_L e^+_R$ (σ_L), $e^-_R e^+_L$ (σ_R) and transverse (σ_T) polarizations [3]. By analyzing σ_R and σ_L, the two mixing parameters of the chargino sector can be determined up to at most a four-fold ambiguity, provided that the electron sneutrino mass is known and one assumes the supersymmetric relation between couplings in the interaction Lagrangian. The addition of transverse polarization allows the ambiguity to be resolved and gives a handle on the sneutrino mass. The role of *transverse* polarization is to allow interference between two different helicity states so that a product of two mixing factors appears in a physical observable instead of sums of squares of individual mixing factors, resolving

the sign ambiguity. Given the measurement of the chargino mass and the mixing parameters, the Lagrangian parameters $M_2, \mu, \tan\beta$ can be determined up to two-fold ambiguity in modulus and a 2π ambiguity in the phase combination $\arg(m_2)+\arg(\mu)$. Such studies need to be redone with more detail, considering partial beam polarization, backgrounds, cuts, and the likely absence of transverse polarization, but there is promise that SUSY parameters can be extracted from real data.

Other investigations have considered the consequences of partial longitudinal polarization at a purely theoretical level, focusing on the case $|\mathcal{P}_-| = .85, |\mathcal{P}_+| = .60$, and studying production cross sections near threshold [4]. Comparing a gaugino-like and Higgsino-like chargino, the total cross sections including the decay $\widetilde{\chi}^- \to e^-\overline{\nu}\widetilde{\chi}_1^0$ are calculated as a function of electron and positron polarization. For an unpolarized positron beam, the cross sections from e_L^- are larger than those from e_R^- for both the gaugino and Higgsino cases. However, the addition of positron polarization gives access to more detailed information. For example, one has the relation that $\sigma(e_R^- e_L^+)$ is less than the unpolarized cross section for gaugino-like charginos, and greater for Higgsino-like charginos. The sensitivity of the forward-backward asymmetry A_{FB} to polarization, and how this effect can be used to bound the sneutrino mass, has also been discussed [5]. Similar considerations can be applied to the case of $\widetilde{\chi}^0\widetilde{\chi}^0$ production. These analyses would benefit from more detailed studies, including backgrounds and addressing the issue of measuring branching ratios.

2.4 Some other new physics

Contact interactions can arise from many sources of new physics, such as compositeness, a heavy Z', leptoquarks, KK excitations, *etc.* The low-energy effect of such physics can be parameterized in an effective Lagrangian as

$$\mathcal{L}_{\text{eff}} = \frac{\tilde{g}^2}{\Lambda_{\alpha\beta}} \eta_{\alpha\beta} (\overline{e}_\alpha \gamma_\mu e_\alpha)(\overline{f}_\beta \gamma_\mu f_\beta), f \neq e, t.$$

The chiral components are extracted by varying $P_{\text{eff}} = \pm P$ (this is just A_{LR}). Positron polarization increases the reach on $\Lambda_{\alpha\beta}$ by $20-40\%$ depending on the nature of the couplings [6].

Low-energy signatures of string theory may include spin-zero resonances with non-negligible couplings to the electron and sizable amplitudes [7], *i.e.*, $\mathcal{A}(e_R^- e_R^+ \to \gamma_{03}^*) = \sqrt{2} e M_S$ and $\mathcal{A}(e_L^- e_L^+ \to \gamma_{04}^*) = \sqrt{2} e M_S$. With positron polarization, the SM backgrounds to these processes should be negligible.

2.5 Transverse polarization

Finally, we should comment on transverse polarization, which has been considered in some chargino studies. Transversely polarized beams are linear combinations of different helicities with equal weight. Transverse polarization can introduce an azimuthal

dependence into production cross sections, proportional to the degree of polarization. However, all such effects in the SM are negligible upon azimuthal averaging for an e^-e^+ collider, because of the small electron mass and Yukawa coupling [8]. Thus, transverse polarization can be used as a probe of physics beyond the SM, when small amplitudes from new physics interfere with larger SM ones. Without the positron polarization, however, there is no visible effect.

3 Experimental issues

3.1 Polarimetry

The baseline NLC design includes a laser-backscattering Compton polarimeter to measure the electron beam polarization with an expected accuracy of 1% or better [9,10]. For the Giga-Z physics program, an accuracy of 0.25% should be achievable in an optimized setup, which is a factor two improvement over SLD's Compton polarimeter. Above the W-pair threshold, the SM asymmetry in forward W pairs can also be used [9]. Sub-1% polarimetry using this technique will require reduction of the background to the W-pair sample below 1%.

If the positron beam can also be polarized, significant improvements in polarimetry are possible. At Giga-Z, the polarimetry error can be improved to 0.1% using the 'Blondel scheme'. In this method, one measures the three independent asymmetries [11,12]:

$$\begin{aligned} A_1 &= \frac{N_{LL} - N_{RR}}{N_{LL} + N_{RR}} \\ A_2 &= \frac{N_{RR} - N_{LR}}{N_{RR} + N_{LR}} \\ A_3 &= \frac{N_{LR} - N_{RL}}{N_{LR} + N_{RL}} = \mathcal{P}_{\text{eff}} A_{LR}, \end{aligned} \tag{12.5}$$

where $\mathcal{P}_{\text{eff}}$ is given by Eq. (12.3). From these three measurements, one can determine A_{LR} (and hence the weak mixing angle) along with $\mathcal{P}_-$ and $\mathcal{P}_+$. It should be noted that $\mathcal{P}_{\text{eff}}$ is typically substantially higher than either $\mathcal{P}_-$ or $\mathcal{P}_+$ and has a smaller uncertainty. For example, if $\mathcal{P}_- = 80\%$ and $\mathcal{P}_+ = -60\%$, then $\mathcal{P}_{\text{eff}} = 94.6\%$, and the error on $\mathcal{P}_{\text{eff}}$ is proportional to the difference from 100%. With a Giga-Z sample using these polarization values, A_{LR} can be determined to an accuracy of 10^{-4} and the beam polarizations to an accuracy of 10^{-3}. These estimates are derived in Chapter 8, Section 1. An advantage of the Blondel scheme for polarimetry is that the luminosity-weighted polarization, P_e^{lum}, is directly measured. A Compton polarimeter measures the average beam polarization and small corrections may be needed to extract P_e^{lum}. It should be noted that a Compton polarimeter is still needed to measure the difference

between the right-handed and left-handed beam polarizations. One also needs to understand the relative luminosities for the four beam polarization states (at the level 10^{-4} for Giga-Z).

Away from the Z-pole, the Blondel scheme with polarized positrons can also be applied to W-pair events. Using W pairs when both beams are polarized, an error on the beam polarizations of 0.1% should be achievable. The large W-pair physics asymmetry can be fit together with the beam polarizations, without sensitivity to backgrounds or assumptions about the polarization asymmetry in W interactions.

3.2 Frequency of spin flips

Depending on the method for producing polarized positrons, it may be difficult to achieve fast reversals of the positron helicity. For the polarized electron source, helicity reversals are easily done at the train frequency (120 Hz for NLC or 5 Hz for TESLA) using an electro-optic Pockels cell in the polarized source laser system. At SLC, the 120 Hz random helicity was very useful in controlling possible small left-right asymmetries in luminosity. Helicity reversals that are fast compared to any time constants for machine feedbacks are desirable. If fast helicity reversals are not possible, then relative integrated luminosities for the different polarization states need to be measured to better than 10^{-4} for Giga-Z. This should be achievable using forward detectors for Bhabha and radiative Bhabha events.

3.3 Run time strategy for LL, LR, RL, RR

One of the advantages of polarizing the positron beam is the increase in event rate by running in the (higher cross section) LR or RL polarization states. However, to take advantage of the Blondel technique for polarimetry and A_{LR} measurements, it is necessary also to accumulate data in the LL and RR states. However, it has been shown that only 10% of the running time has to be spent in the lower-event rate LL and RR states to achieve adequate statistics for the asymmetry measurements [13]. One anticipates equal run times for the LR and RL configurations, even though some physics analyses may benefit most from selecting one of these configurations for enhancing or suppressing W pairs or to enhance a cross section for a new process. Of course, some new physics searches will benefit from choosing those configurations that are suppressed in the SM.

4 Sources of polarized positrons

Several techniques have been suggested for producing polarized positrons for a linear collider. Present designs are largely conceptual, and much work remains before they can be realized.

In 1979, Mikhailichenko and Balakin [14] proposed generating circularly polarized photons by running a high-energy electron beam through a helical undulator. These photons are directed onto a thin target, where they produce e^+e^- pairs. Selecting positrons near the high-energy end of the spectrum gives a sample with appreciable polarization. Okugi *et al.* [15] have proposed generating polarized photons by colliding intense circularly polarized laser pulses with few-GeV electron beams. Variations on this theme have been proposed in an attempt to mitigate the rather extreme requirements on laser power by using an optical cavity to concentrate and store multiple laser pulses [16,17]. Finally, Potylitsin [18] has proposed directing a 50 MeV beam of polarized electrons onto a thin target.

4.1 Helical undulator

In the baseline TESLA design, unpolarized positrons are generated by photons produced when the full-energy electron beam is passed through a 100 m long wiggler prior to collision. The photon beam is directed to a thin, rotating target where e^+e^- pairs are produced, and the positrons are subsequently captured, accelerated, and damped. This novel approach reduces the power dissipated in the positron target to manageable levels and significantly reduces radiation in the target area.

Replacing the wiggler with a helical undulator would in principle allow polarized positrons to be produced. The magnetic field created by a helical undulator has two transverse components that vary sinusoidally down the length of the device, the vertical component shifted in phase by 90° from the horizontal. Such a field is created by two interleaved helical coils of the same handedness, driven by equal and opposite currents. Typical fields are of order 1 T; the period of the sinusoidal field variation is about 1 cm. The resulting electron trajectory for a 150 GeV beam is a helix whose axis coincides with that of the undulator; the radius of curvature is measured in nanometers! The undulator coils must be quite compact, with an internal radius of several millimeters and an outer radius of about 1 centimeter [19].

Efficient positron production requires photon energies of about 20 MeV, which in turn necessitates electron beam energies of approximately 150–200 GeV. The photons produced within $\theta \approx 1/\gamma$ have high average polarization. Collimators which are arranged to absorb the radiation at larger angles remove about 80% of the flux. To compensate this loss, the undulator length must be about 200 meters, somewhat longer than that of the wigglers used in the TESLA positron source. The undulator requires a very low-emittance electron beam, which probably prevents reuse of the electron beam after it has been used for high-energy collisions. It is possible that one could direct the primary high-energy electron beam through the undulator prior to collision. A drift space of about 200 meters between the undulator and the target is required to achieve the required photon beam size.

The highly polarized photons produced in the undulator are directed against a 0.4 X_0 target, where pair production can occur. Positrons produced with energies above

15 MeV are highly polarized. With this energy cut, roughly 0.025 e^+/incident photon is collected and 60% polarization is obtained [19]. Collection of the positrons requires solenoidal magnets, rf acceleration, and a predamping ring to handle the enlarged phase space. On paper, the scheme can generate the needed positron bunch currents.

The undulator scheme makes excellent use of the high-energy electron beam as the source of polarized photons. The low emittance requirements probably preclude the use of the post-collision beam. Whether the primary, pre-collision beam should be run through the undulator, or a dedicated beam should be generated for the sole purpose of positron production is a choice still being debated. A helical undulator generates positrons of a single helicity, so other means must be developed to flip the spin, and preferably to do so rapidly. Many of the photons could be absorbed in the undulator coil, so a workable design must accommodate many kilowatts of power dissipation.

4.2 Backscattered laser

A second method for producing highly polarized photons with enough energy to produce electron-positron pairs on a thin target involves backscattering an intense circularly polarized laser beam on a high-energy electron beam. The highest energy photons are strongly polarized and have helicity opposite to that of the incident laser light. As above, positrons are produced when these photons intercept a thin target. The highest-energy positrons are strongly polarized.

Omori and his collaborators have made a conceptual design of a laser-backscattering polarized positron source suitable for NLC/JLC [20]. They arrange for multiple collisions between polarized laser pulses from 50 CO_2 lasers and a high-current 5.8 GeV electron beam. The laser system must provide 250 kW of average optical power, which is regarded as extremely ambitious. Positron production is accomplished just as in the helical undulator scheme above. Simulations indicate that 9.4% of the incident photons produce a positron above 20 MeV, 26% of which are accepted into the pre-damping ring, with an average polarization of 60% [20].

This scheme makes production of polarized positrons independent of the high-energy electron beam, hence independent of its energy, but does so at the very considerable expense of a dedicated high-current linac and a very complex laser system. The estimated power required by those systems is roughly 10% of that required for the whole collider facility.

5 Conclusions

A polarized positron beam at a LC would be a powerful tool for enhancing signal-to-background, increasing the effective luminosity, improving asymmetry measurements with increased statistical precision and reduced systematic errors, and improv-

ing sensitivity to non-standard couplings. Suppression of W-pair backgrounds can be improved by a factor 3 with 60% positron polarization. By limiting the running time allotted for LL and RR modes to 10%, the effective luminosity for annihilation processes can be enhanced by 50%. For asymmetry measurements, the effective polarization is substantially increased (*e.g.*, from 80% to 95%) and the systematic precision is improved by a factor 3. With these features, a polarized positron beam may provide critical information for clarifying the interpretation of new physics signals. Polarized positrons are needed to realize the full potential for precision measurements, especially those anticipated for Giga-Z running at the Z-pole.

Designs of polarized positron sources have not reached maturity. Several approaches have been proposed, the most promising of which uses a helical undulator, but to date no real engineering designs, cost estimates, or experimental proofs of principle are available. Since much of the benefit of a polarized positron source would be negated if luminosity were compromised, it is very important that eventual designs have some margin on projected yields. Also, the source needs to be available for all collision energies. The helicity of a polarized positron source may be difficult to switch quickly and provision needs to be made to allow this, with a strong motivation to have helicity-switching capability at the train frequency. Present designs must be further developed and additional R&D is needed to pursue new schemes, some of which have been mentioned here.

Though a polarized positron source is not yet advanced enough to be included as part of the baseline linear collider design, it is an attractive feature that should be pursued as an upgrade. Site layout and engineering for a linear collider baseline design should accommodate such an upgrade at a later date. This has been done for the TESLA design and needs to be done for the NLC design as well.

References

[1] G. Moortgat-Pick and H. Steiner, EPJdirect **C6**, 1 (2001), DESY-00-178.

[2] A. Bartl, H. Eberl, H. Fraas, S. Kraml, W. Majerotto, G. Moortgat-Pick and W. Porod, hep-ph/0010018.

[3] S. Y. Choi, M. Guchait, J. Kalinowski and P. M. Zerwas, Phys. Lett. **B479**, 235 (2000) [hep-ph/0001175].

[4] G. Moortgat-Pick, A. Bartl, H. Fraas and W. Majerotto, Eur. Phys. J. **C18**, 379 (2000) [hep-ph/0007222].

[5] G. Moortgat-Pick and H. Fraas, Acta Phys. Polon. **B30**, 1999 (1999) [hep-ph/9904209].

[6] A. A. Babich, P. Osland, A. A. Pankov and N. Paver, Phys. Lett. **B481**, 263 (2000) [hep-ph/0003253].

[7] S. Cullen, M. Perelstein and M. E. Peskin, Phys. Rev. **D62**, 055012 (2000) [hep-ph/0001166].

[8] K. Hikasa, Phys. Rev. **D33**, 3203 (1986).

[9] M. Woods, Int. J. Mod. Phys. **A15**, 2529 (2000).

[10] P. C. Rowson and M. Woods, SLAC-PUB-8745 (2000).

[11] A. Blondel, Phys. Lett. **B202**, 145 (1988).

[12] F. Cuypers and P. Gambino, Phys. Lett. **B388**, 211 (1996); F. Cuypers and P. Gambino, PSI-PR-96-27 (1996).

[13] R. Hawkings and K. Monig, DESY 99-157 (1999).

[14] V. E. Balakin and A. A. Mikhailichenko, *The Conversion System for Obtaining High Polarized Electrons and Positrons*, INP 79-85 (1979).

[15] T. Okugi *et al.*, Jpn. J. Appl. Phys. **35**, (1996).

[16] J. Frisch, in Proceedings of the Workshop on New Kinds of Positron Sources for Linear Colliders, SLAC Report 502, 125 (1997).

[17] A. Potylitsin, *Single Pass Laser Polarizatrion of Ultrarelativistic Positrons*, arXiv:physics/0001004 (2000).

[18] A. P. Potylitsin, Nucl. Inst. and Meth. **A398**, 395 (1997).

[19] K. Flottmann, S. G. Wipf, *Field Enhancement of a Superconducting Helical Undulator with Iron*, TESLA 96-05. K. Flottmann, *Investigations toward the Development of Polarized and Unpolarized High Intensity Positron Sources for Linear Colliders*, DESY 93-161a (1993).

[20] T. Omori, *A Concept of a Polarized Positron Source for a Linear Collider*, KEK 99-188 (2000).

Chapter 13 Photon Collider

1 Introduction

The concept of producing $\gamma\gamma$ collisions through Compton backscattering of laser photons in a linear collider [1,2] was proposed in 1981. The available laser technology was barely adequate for the accelerators operating at that time. The linear colliders proposed since then are orders of magnitude more ambitious and require equivalent improvements in laser technology to produce a $\gamma\gamma$ collider. Fortunately, breakthroughs in laser technology have made feasible lasers capable of delivering the 10 kW of average power in short pulses of 1 TW peak power that are required for the NLC. The problem of obtaining such high peak power was resolved in 1985 with the invention of Chirped-Pulse Amplification (CPA). The high average power requirement could not be met without a long technology campaign that involved the development of diode-pumped lasers, adaptive optics and high-power multilayer optics, plus all of the associated engineering for thermal management. Nevertheless, today the laser and optics technology is finally in hand to proceed with an engineering design of a photon collider.

In the past few years there has been a crescendo of interest and theoretical activity in $\gamma\gamma$. This work has focused particularly on the precision measurement of the radiative width of the Higgs, the study of heavy neutral Higgs bosons, and on detailed studies of supersymmetric particles and the top quark. The $\gamma\gamma$ channel is also highly sensitive to new physics such as large extra dimensions and the appearance of strong gravity at the 10 TeV scale.

With the publication of the TESLA Technical Design Report (TDR) and the development of the NLC/JLC toward full conceptual design, it was appropriate therefore to bring the photon collider from its highly schematic state into parity with the mature design of the rest of the accelerator. A year ago, a team of scientists and engineers from LLNL, SLAC, and UC Davis along with a FNAL-Northwestern theory consortium began to develop a complete design that would be required for full incorporation in the future NLC Conceptual Design Report. This effort involved a tightly integrated effort of particle theory and modeling, accelerator physics, optics, laser technology and engineering. The guiding principle was to develop a design that was robust, relied on existing technology, involved a minimum of R&D, and posed the least risk. Considerations of elegance, power efficiency and cost, while not unimportant, were relegated to second place. A satisfactory design was also required to stay well away from compounding detector backgrounds, and to involve minimal modification to the existing Final Focus and detector geometries. While this is still

a work-in-progress, the conclusion of the study so far is that a photon collider can be built with confidence on existing technology, satisfying these guidelines and criteria. This chapter describes the principal physics drivers for the $\gamma\gamma$ IR, and the basic design and technologies to implement it.

2 Physics Studies at a $\gamma\gamma$ Collider

2.1 Production of Higgs bosons

Perhaps the most important physics that can be done at a $\gamma\gamma$ collider is in probing the properties of the Higgs boson(s). At such colliders the Higgs bosons of the SM and the MSSM can be singly produced as s-channel resonances through one-loop triangle diagrams. They will be observed in their subsequent decay to $b\overline{b}, \tau^+\tau^-, WW^*, ZZ$, *etc.* Contributions to this type of loop graph arise from all charged particles that receive mass from the produced Higgs. In the SM, the loop contributions are dominated by the W and top. SUSY contributions may be as large as 10% of the SM amplitude. In addition, other currently unknown particles may also contribute to the loop and their existence may be probed indirectly by observing a deviation from the SM value. (Since other particles, such as gravitons, can also appear in the s-channel, it will also be necessary to determine the spin of any resonances that are produced.) By combining measurements at both e^+e^- and $\gamma\gamma$ colliders it will be possible to determine both the quantity $\Gamma_{\gamma\gamma}$ and the Higgs total width [3,4].

A light Higgs ($m_H \leq 135$ GeV) can be detected in the $b\overline{b}$ mode, with the main background due to the conventional QED $\gamma\gamma \to b\overline{b}, c\overline{c}$ continuum [3,4]. Because of the relatively large $c\overline{c}$ cross section, excellent b tagging is necessary. The two initial photon polarizations can be chosen to produce spin-zero resonant states and to simultaneously reduce the cross section for the background which, at tree level, is suppressed by m_q^2/m_h^2. Unfortunately, both QCD and QED radiative corrections remove this strong helicity suppression and must be well accounted for in both the Higgs and QED channels when comparing anticipated signals and backgrounds. Several detailed Monte Carlo simulations have been performed for this channel, with some typical results shown in Fig. 13.1 [5]; these have demonstrated that the quantity $\Gamma_{\gamma\gamma}B(h \to b\overline{b})$ can be determined with a relative error of 2%. Assuming that the $b\overline{b}$ branching fraction can be measured to the level of 1% by combining e^+e^- and $\gamma\gamma$ data, $\Gamma_{\gamma\gamma}$ will be determined at the level of 2%. This level of accuracy is sufficient to distinguish the SM and MSSM Higgs and to see contributions of additional heavy states to the triangle loop graph. If e^+e^- colliders can also provide the branching fraction for $h \to \gamma\gamma$ at the $\sim 10\%$ level, the total Higgs width can be determined with a comparable level of uncertainty. A similar analysis can be performed using either the WW^* or ZZ final state for Higgs masses up to 350-400 GeV, with comparable results [4].

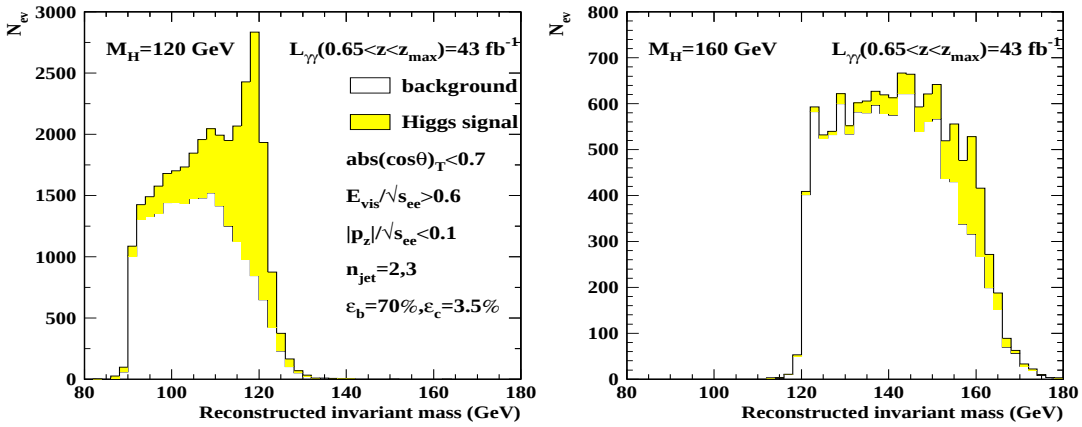

Figure 13.1: Mass distributions for the Higgs signal and heavy quark background for a Higgs mass of 120(left) and 160(right) GeV from Söldner-Rembold and Jikia [5]. The reduced signal-to-background at 160 GeV reflects the diminished branching ratio to $b\overline{b}$ near the WW threshold.

Very heavy Higgs bosons, such as those present in the MSSM, can also be produced as s-channel resonances in $\gamma\gamma$ collisions. In the MSSM, these heavy states have suppressed couplings to gauge bosons and may be most easily observed in $b\overline{b}$ or $t\overline{t}$ final states. These states may escape discovery at the LHC for intermediate values of $\tan\beta$. At e^+e^- colliders they can only be produced via associated production, $e^+e^- \to HA$, and thus lie outside the kinematic reach of the machine if their mass exceeds 240 GeV. The single production mode of the $\gamma\gamma$ collider allows the discovery reach to be extended to over 400 GeV. The $\gamma\gamma$ collider also allows one to separate degenerate H and A states and to study possible CP-violating mixing between H and A using linear polarization.

2.2 Supersymmetric particle production

For production significantly above threshold, sfermion and charged Higgs boson pairs have production cross sections in $\gamma\gamma$ collisions that are larger than those in e^+e^- annihilation. Thus, $\gamma\gamma$ collisions can provide an excellent laboratory for their detailed study. In addition, $\gamma\gamma$ production isolates the electromagnetic couplings of these particles, whereas in e^+e^- the Z and possible t-channel exchanges are also present. Thus complementary information can be obtained by combining data extracted from the two production processes. It should be noted that the search reach for new particles is typically somewhat greater in e^+e^- because of the kinematic cut-off of the photon spectra. However, the SUSY process $\gamma e \to \tilde{e}_{L,R}\chi_1^0$ shows that there are exceptions to this rule; the threshold for this process can be significantly below that for $\tilde{e}$ pair production in e^+e^- collisions when the χ_1^0 is light. In the study of this reaction, both the $\tilde{e}$ and χ_1^0 masses can be determined.

2.3 $\gamma\gamma \to W^+W^-$ and $\gamma e \to W\nu$

New physics beyond the SM can affect the expected values of the trilinear and quartic couplings of gauge bosons. These couplings can be studied in the reactions $\gamma e \to W\nu$ and $\gamma\gamma \to WW$, as well as in $e^+e^- \to WW$ [6]. It is noteworthy that the photon collider reactions isolate the anomalous photon couplings to the W, while $e^+e^- \to WW$ also involves anomalous Z couplings. In addition, the process $\gamma\gamma \to W^+W^-$ allows access to the quartic $\gamma\gamma W^+W^-$ coupling. The complementarity of the three reactions in determining the anomalous couplings is illustrated in Fig. 13.2, taken from [6]. Since the time of this study, it has been understood how to achieve bounds on the anomalous couplings from $e^+e^- \to WW$ that are a factor of 30 better than those shown in the figure, by taking advantage of more systematic event analysis and higher luminosities. Methods for that analysis are described in Chapter 5, Section 2. A similar improvement should be possible for the constraints from $\gamma e \to W\nu$ and $\gamma\gamma \to WW$, though the detailed study remains to be done.

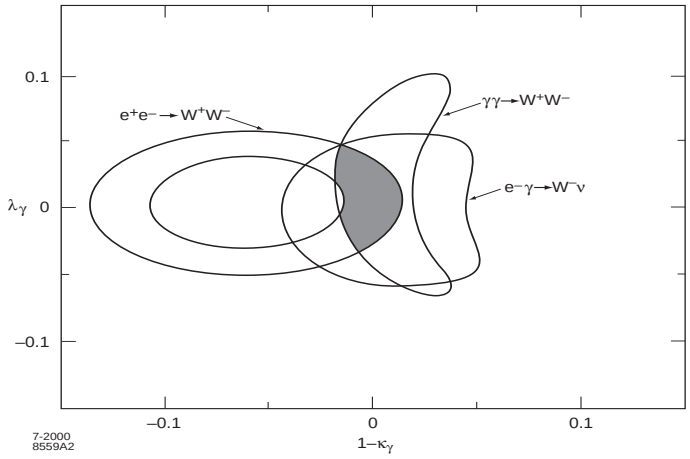

Figure 13.2: Allowed overlapping regions in the $\Delta\kappa_\gamma - \lambda_\gamma$ anomalous coupling plane, from the analysis of Choi and Schrempp [6].

The reaction $\gamma\gamma \to W^+W^-$ is also highly sensitive to other forms of new physics such as the exchange of virtual towers of gravitons that occurs in models of millimeter-scale extra dimensions [7,8]. It has been shown that this is the most sensitive process to graviton exchange of all those so far examined. Such exchanges can lead to substantial alterations in cross sections, angular distributions, asymmetries and W polarizations. These effects make it possible to probe the associated gravitational mass scale, M_s, to values as high as $13\sqrt{s}$ for the correctly chosen set of initial laser and electron polarizations. (For comparison, the reach in e^+e^- is about $7\sqrt{s}$.) The search reach as a function of the $\gamma\gamma$ luminosity is shown in Fig. 13.3 for the various

polarization choices. This same process can be used to search for graviton resonances such as those predicted in the Randall-Sundrum model [9].

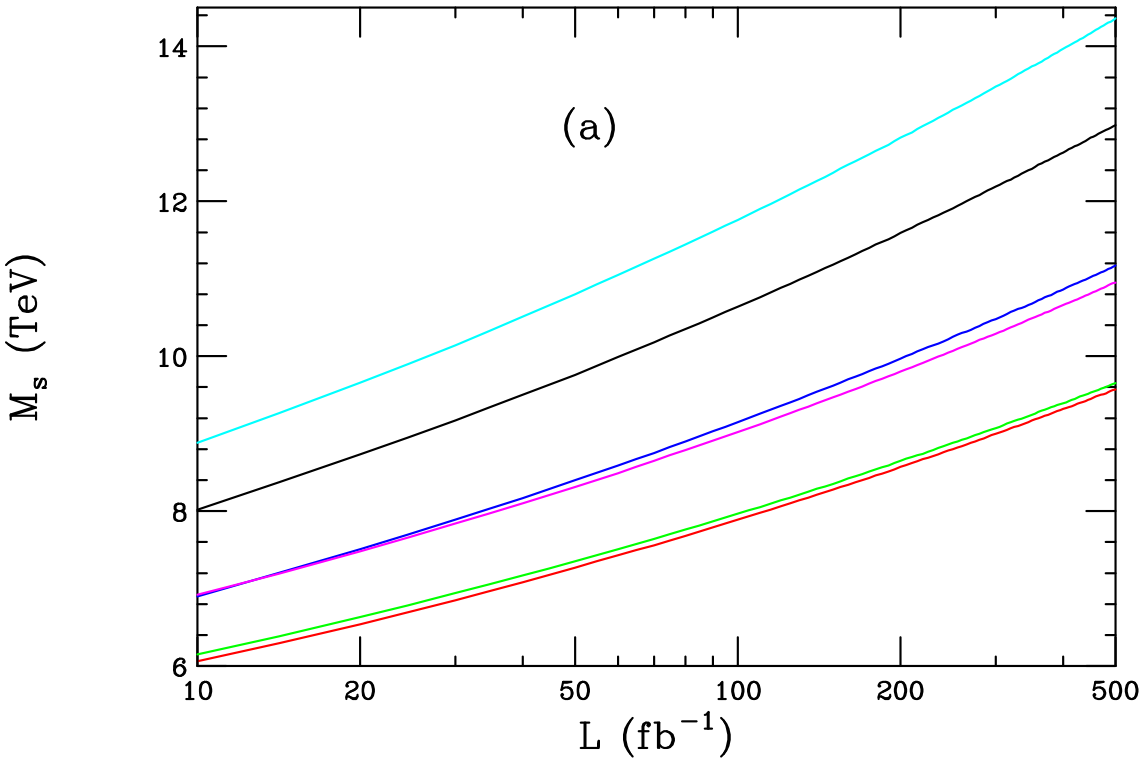

Figure 13.3: M_s reach for the process $\gamma\gamma \to W^+W^-$ at a 1 TeV e^+e^- collider as a function of the integrated luminosity for the different initial and final state polarizations. From top to bottom on the right hand side of the figure the polarizations are $(-++-)$, $(+--)$, $(++--)$, $(+-+-)$, $(+--)$, and $(++++)$.

2.4 $\gamma\gamma \to t\bar{t}$

Since the top quark is the heaviest SM fermion, with a Yukawa coupling that is quite close to unity, one might expect that its properties may be the most sensitive to new physics beyond the SM. For example, the top may have anomalous couplings to the SM gauge bosons, including the photon. The cross section for top pairs in $\gamma\gamma$ collisions is somewhat larger than in e^+e^-, thus this process may provide the best laboratory to probe new physics couplings to the top. In addition, while both e^+e^- and $\gamma\gamma$ colliders can probe the anomalous $\gamma t\bar{t}$ couplings, these are more easily isolated in $\gamma\gamma$ collisions. As shown in [10], there are 4 form factors that describe this vertex, one of which is CP-violating and corresponds to the top quark electric dipole moment. By measurements of the $t\bar{t}$ angular distribution significant constraints on these form

factors are possible with sensitivities to both electric and magnetic dipole moment couplings that are about an order of magnitude better in $\gamma\gamma$ colliders than in e^+e^- machines. In addition, CP-violating couplings can be directly probed through the use of polarization asymmetries and limits superior to those obtainable from e^+e^- colliders are possible.

2.5 Other processes

There are many other interesting processes that one can study in $\gamma\gamma$ collisions. As far as new physics is concerned, the $Z\gamma$ and ZZ final states can be used to probe anomalous $ZZ\gamma$ and $Z\gamma\gamma$ couplings [11] while the $\gamma\gamma$ final state can be used to search for non-commutativity and violations of Lorentz invariance in QED [12]. The couplings of leptoquarks discovered in e^+e^- collisions can be more easily disentangled by using data from both $\gamma\gamma$ and γe collisions [13]. It may also be possible to form resonances of stoponium, the supersymmetric version of toponium, with production rates that are significantly higher than in e^+e^- [14].

Within the SM there are a number of interesting QCD processes that can also be examined to obtain information on topics such as the gluon and quark content of the photon, the spin-dependent part of the photon structure function, and the QCD pomeron. These topics are reviewed in Chapter 7, Section 3.

3 Compton Backscattering for $\gamma\gamma$ Collisions

3.1 Introduction

High-energy photons can be produced through two-body scattering of laser photons from a high-energy electron beam. For example, the scattering of 1 eV laser photons from an electron beam of 250 GeV can produce gammas of up to 200 GeV. An electron linear collider can be converted to a $\gamma\gamma$ collider if a high-power laser pulse intersects the electron beam just before the interaction point (IP). The point where the laser beam intersects the electron beam—the conversion point (CP)—can be within 1 cm of the IP. A high $\gamma\gamma$ luminosity comparable to that of e^+e^- can be achieved, since the photons will focus to about the same spot size as the electron beam. The principles are reviewed in detail elsewhere [15].

3.2 Photon spectra

For the case mentioned above—1 eV laser photons and 250 GeV electrons—the energy spectrum of the backscattered photons ranges from 0 up to 0.8 of the incoming beam energy. Two-body kinematics creates a correlation between the photon energy and the angle between the outgoing photon and the incoming electron. The maxi-

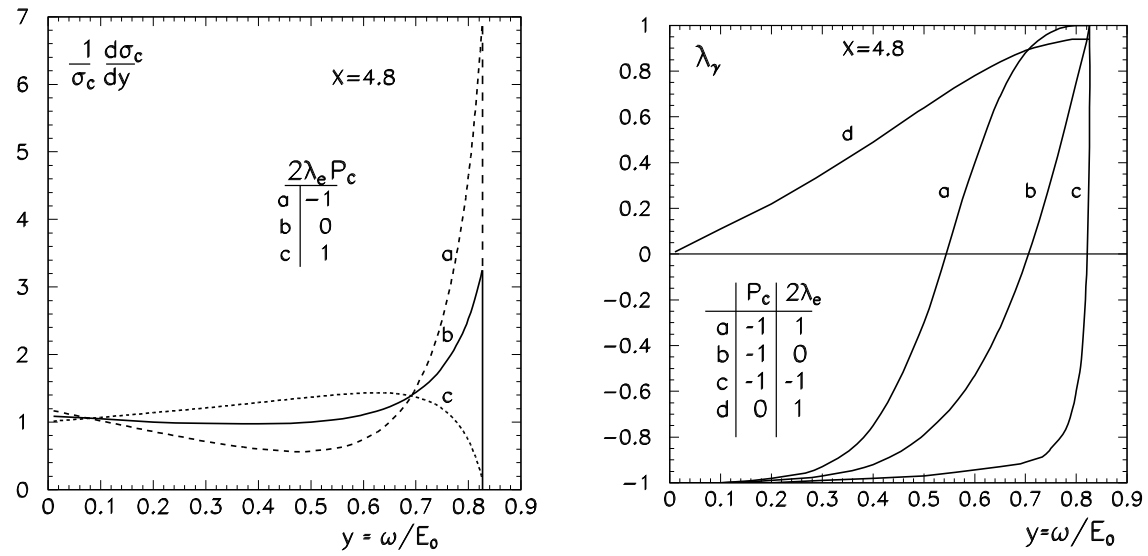

Figure 13.4: The energy spectrum and helicity spectrum of the Compton-backscattered photons for various helicities of the incoming electron beam with circularly polarized incoming photons [15]. The variable y is the photon energy as a fraction of the electron beam energy. The laser photon and electron helicities are designated by P_c and λ_e. The parameter $x = 4E_e\omega_0/m^2c^4$.

mum photon energy occurs when the produced photon is collinear with the incoming electron.

The exact energy spectrum is a function of the polarization of the incoming electron and laser beams. Figure 13.4 shows the energy spectrum of the backscattered photons for circularly polarized laser photons. The population of the high-energy peak is maximized when the electron beam is fully polarized and of opposite helicity to the laser beam. For that situation, the high-energy photons are also fully circularly polarized. While the lasers naturally produce linearly polarized photons, any combination of circular and linear polarization can be produced through the use of quarter-wave plates.

From Fig. 13.4 it can be seen that the ability to polarize the incoming electron beam is crucial for producing high-energy $\gamma\gamma$ collisions with polarized gammas. Currently it is foreseen that the electron beams will achieve 80% polarization while positrons will be unpolarized. This makes it attractive to run in an e^-e^- mode rather than e^+e^-. Many Standard Model backgrounds are also suppressed by choosing e^-e^- running.

Calculating the $\gamma\gamma$ luminosity spectrum at the IP is not as simple as convoluting the single-scattering energy spectrum with itself. There are additional sources of γ's that must be included. An electron can Compton backscatter multiple times as it

passes through the laser beam. This leads to a tail of low-energy photons, as can be seen in Fig. 13.5. Also, the leftover electron beam arrives at the IP coincident with the photons. When the two electron beams interact they produce a large number of beamstrahlung photons. All of these contribute to the $\gamma\gamma$ luminosity.

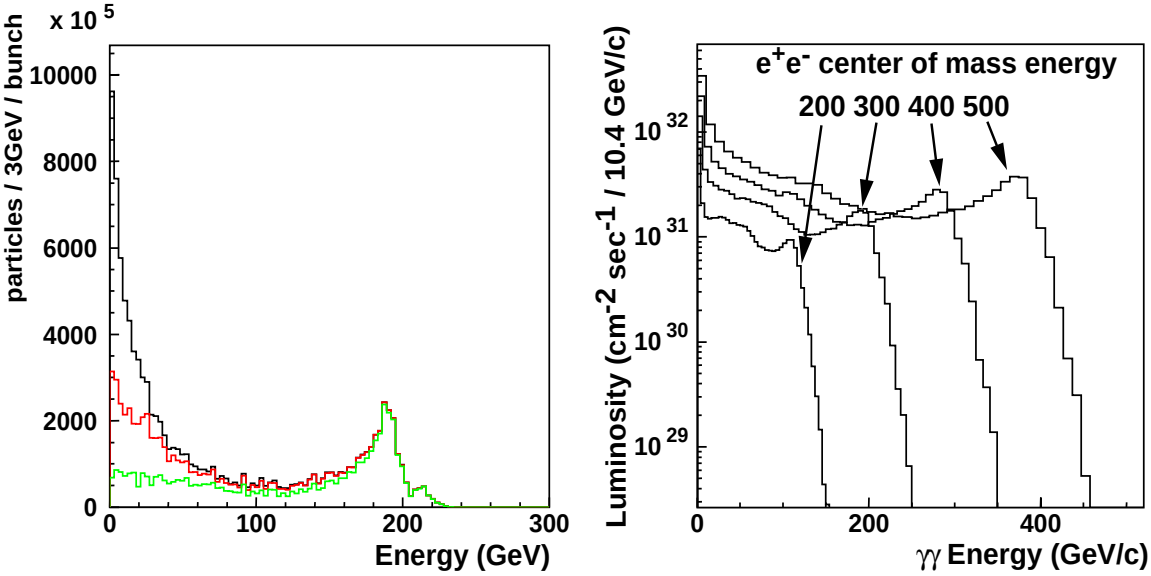

Figure 13.5: The first plot shows the energy spectrum from Compton backscattering when (respectively, from the bottom curve to the top) primary, secondary, and all higher scatters are taken into account. The second plot shows the $\gamma\gamma$ luminosity for e^-e^- center-of-mass energies of 500, 400, 300, and 200 GeV for the NLC-B machine parameters.

As a result of the energy-angle correlation, the spot size for collision of soft photons will be larger than that for the collision of harder photons. Thus the luminosity spectrum may be hardened by increasing the distance between the CP and IP. In the following, we chose the CP to be 5 mm from the IP.

To compute the $\gamma\gamma$, $e\gamma$ and ee luminosities, we use the program CAIN [16], which models all of the processes just described. Results for various incident electron beam energies are shown in Fig. 13.5. The luminosity spectrum peaks at $\gamma\gamma$ CM energies close to 0.8 times of the e^-e^- CM energy. The decrease of luminosity with decreasing CM energy, apparent from the plot, is primarily caused by the increased spot size of the electron beams and, secondarily, by a softer Compton-backscattering spectrum. For a 120 GeV Higgs this leads to a situation where higher luminosities can be achieved by running at 500 GeV e^-e^- CM energy at the cost of having unpolarized photons. For measurements requiring definite states of $\gamma\gamma$ polarization, on-peak running with 150 GeV e^-e^- CM energy is required.

3.2.1 Accelerator modifications

While no changes to the accelerator are required to produce $\gamma\gamma$ collisions, some changes can optimize performance. Beam-beam interactions are a major concern for e^+e^- but are not present in $\gamma\gamma$ collisions. Therefore the β functions of the Final Focus should be as small as possible to achieve a minimum spot size and maximum luminosity. The luminosity improvements from small β functions are limited by chromatic aberrations in the Final Focus and the hourglass effect, in which the β function becomes comparable to the longitudinal spot size. In addition, a small transverse spot size tends to select unboosted events because of the correlation between the energy and production angle of the high-energy γ's. A Final Focus design with rounder beams simplifies the final doublet stabilization and has been shown to recover nearly a factor of two in luminosity by increasing the contribution of boosted events. However, these boosted events suffer from reduced reconstruction efficiency and we have not yet optimized the design for this effect.

Achieving rounder beams requires only a change in the strength of the Final Focus magnets. It is useful also to cut the number of bunches in half and double the bunch charge, to better match the laser technology. This nominally increases the luminosity by a factor of two, although this is not fully achieved due to the increased emittance growth and the increased longitudinal spot size. The parameters we use are shown in Table 13.1. These have been reviewed and approved by the NLC machine group. When we reduce the e^-e^- CM energy such that the $\gamma\gamma$ peak is at 120 GeV for Higgs running, the $\gamma\gamma$ luminosity becomes 2.9×10^{31} cm^2/s/GeV at $\sqrt{s_{\gamma\gamma}} = 120$ GeV, with 80% of events being spin 0.

e^-e^- CM Energy (GeV)	490
Luminosity	1.23×10^{33} @ >65% e^-e^- energy
Bunch Charge	1.5×10^{10}
Bunches / pulse	95
Bunch separation	2.8 ns
$\gamma\epsilon_x$ at IP	360×10^{-8} m-rad
$\gamma\epsilon_y$ at IP	7.1×10^{-8} m-rad
β_x / β_y at IP	0.76/1.81 mm
σ_x / σ_y at IP	76/16 nm
σ_Z at IP	0.150 mm

Table 13.1: NLC-G parameter set. Unless otherwise noted parameters are identical to NLC-H.

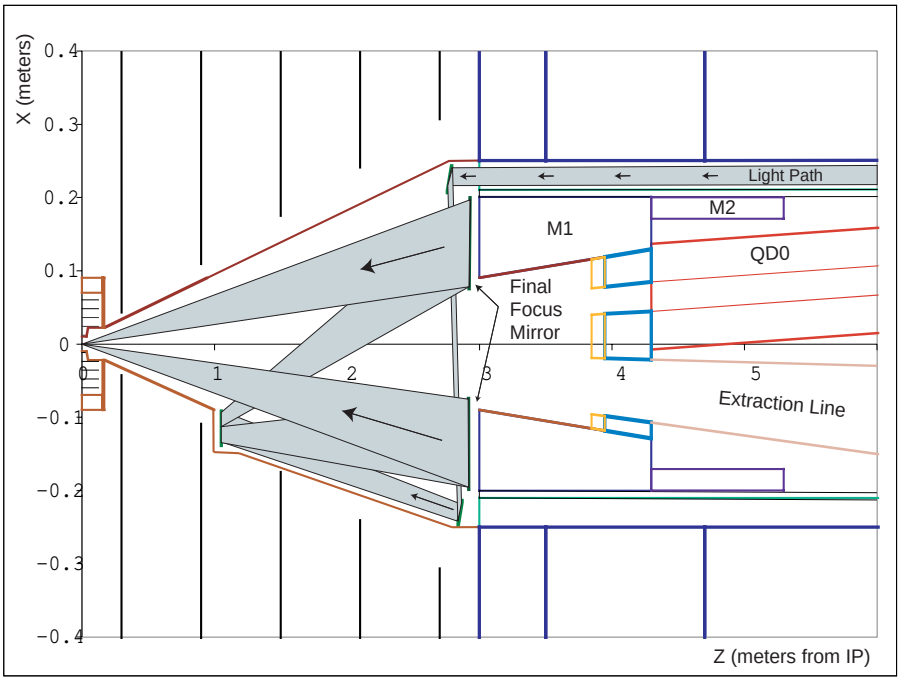

Figure 13.6: Optical configuration to inject the laser light into the Interaction Region. The high subpulse intensity requires all these optics to be reflective and mounted inside the vacuum enclosure.

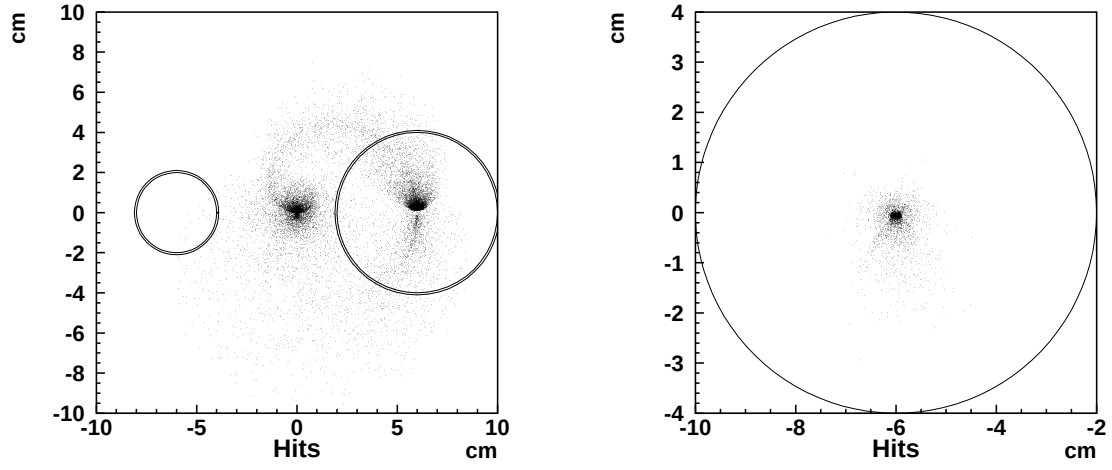

Figure 13.7: The front face of the magnet at $z = 4$ meters. The first plot shows the impact point of the pair background. High-energy particles travel out the extraction line. Low-energy particles spiral in the solenoidal magnetic field of the detector. The second plot is an expanded view of the extraction line aperture showing the location of the outgoing beam.

3.3 Interaction region design and backgrounds

Figure 13.6 shows the interaction region for a $\gamma\gamma$ collider. The design begins from the IR for e^+e^- collisions, but many modifications are needed to accommodate the laser beams. The first of these is the system of mirrors required to bring laser light into the IR, described in detail in Section 4.1. The mirrors have been carefully placed to be outside the path of the beams and the pair background. The pair background consists of low-energy electrons and positrons which spiral in the magnetic field of the detector. Their transverse location at $z = 4$ meters can be seen in Fig. 13.7. No additional backgrounds are generated by the presence of the mirrors.

The extraction lines for the spent beams must be modified for the $\gamma\gamma$ interaction region. The energy spectrum of electrons leaving the conversion point is composed of unscattered electrons at the beam energy and scattered electrons which peak around 1/5 the beam energy. The low-energy electrons receive a larger angular deflection from the beam-beam interaction at the IP, necessitating an increased aperture for the extraction line. Additionally, just as in the case of the pair background, the low-energy electrons spiral in the magnetic field. Figure 13.7 shows the position of the outgoing electrons at the entrance to the extraction line. An aperture of ± 10 milliradians accommodates these particles. In order to prevent mechanical interference between the extraction line and the last focusing quadrupole, the crossing angle has been increased from 20 to 30 milliradians.

Increasing the extraction line aperture has a detrimental effect on the neutron background levels at the IP. The Silicon Vertex Detector, 1.2 cm away from the IP, now has a direct line of sight back to the beam dump 150 meters away. It experiences a fluence of 10^{11} neutrons/cm^2/year. The standard CCD technology chosen for the e^+e^- IR cannot withstand it. The $\gamma\gamma$ IR would need a rad-hard CCD or pixel design.

We foresee no impact to the detector aside from the need for a rad-hard vertex detector. The machine backgrounds in the $\gamma\gamma$ IR are comparable to the e^+e^- IR. Still to be evaluated is the effect of resolved photon events from the higher $\gamma\gamma$ luminosity.

4 IR optical system

4.1 Optics design

The function of the optical system is to bring the laser beam to the IR while also minimizing the required laser pulse energy. The requirement for efficient conversion of the electrons sets the laser photon density required at the interaction point. The optical system will focus the laser beam at a point near the interaction point to maximize the conversion probability. The size of the laser focal spot will be much larger than the electron beam; therefore the size of the focal point should be minimized in order to minimize the required laser pulse energy.

When bringing a beam to a focus, the size of the focal point is determined by the f-number of the focusing optic, defined as the ratio of the focal length to the optic diameter. The size of the useful laser spot is approximately the wavelength times the f-number. There is a limit, however, to how small one can usefully make the f-number. The focal spot has a limited depth of focus. When the electron-photon interaction region becomes longer than the depth of focus, the required laser energy becomes independent of the f-number. Lowering the f-number beyond this point results in no decrease in the required laser pulse energy. Optimally, the laser pulse length should be the same as the electron bunch length to minimize the required pulse energy. However, at such high intensities, non-linear effects degrade the purity of the photon polarization. We choose a pulse length of 2 ps FWHM, which is well matched to the available laser technology. For such a 2 ps laser pulse, decreasing the f-number below 7 gains little further energy reduction. For the reference design the f-number is 8.

Figure 13.6 shows the optical design near the interaction region. The final focusing optic is located at the 3 m station and is mounted adjacent to (or on) the 40 cm diameter tungsten plug (M1). The optic has a 300 cm focal length and a 38 cm diameter, giving it an f-number of 8. The central 15 cm hole provides a space for the electron beams and high-energy scattered electrons to pass through the Final Focus optic. The secondary optic is mounted off-axis to minimize the obscuration of the laser beam. Additional turning optics provide centering and pointing capabilities as well as beam injection to the secondary optic. The high subpulse intensity requires all these optics to be reflective and mounted inside the vacuum chamber.

The laser beam enters the IR from one side. A symmetric set of optics (not shown in Fig. 13.6) takes the beam to a mirror that sends the beam back to a focus intersecting the second electron beam. The difference in the image plane of the focal spots as well as the difference in arrival times can then be used to separate the incoming and exiting laser beams in the beam transport system.

4.2 Beam pipe modifications

The short pulse format of the laser results in beam intensities that cannot be propagated through air or transmissive optics. The pulse compression, beam transport and IR injection optics will all be reflective optics inside vacuum enclosures. The small vacuum pipe that transports the electron beam must be expanded in the IR to contain the laser injection optics (as shown in Fig. 13.6). The level of vacuum required will be determined by the electron beam since it will be higher than needed by the laser. It should be noted that the vacuum requirement of the electron beam may place restrictions on the materials that can be used in the optics mounts and controls.

The laser beam transport pipe will contain isolation gate valves that will be open when the laser is operating. These valves can be closed during maintenance and

other operations when the laser in not operating. They can also be used to prevent contamination or accidental pressurization of the linac and IR during shutdowns.

The optics and vacuum enclosures will be mounted on the same structures as the electron beam transport system. The electron beam transport system in the IR region has not been designed in sufficient detail to begin the design of the laser system interfaces. The seismic requirements for the laser optics are not as stringent as for the Final Focus magnets. If both systems use the same supports, it will be important that the laser system does not feed excessive acoustic energy into the final quadrupole support structure.

5 Laser system

5.1 Requirements and overview

The laser system must match the pulse format of the electron beam and supply an adequate photon density at the IR to backscatter the laser photons efficiently to gamma rays. For efficient conversion of 250 GeV electrons, the optimal laser wavelength is one micron. The laser requirements for the NLC are summarized in Table 13.2.

A picosecond-duration laser pulse cannot be amplified to the joule level directly. The combination in the laser subpulse of a high pulse energy (1 J) and a short pulse duration (2 ps) generates field intensities that will damage laser materials. This problem is solved by first stretching a very low-energy laser subpulse to 3 ns and then amplifying this long pulse. The pulse is then compressed back to 2 ps for use in the IR. The procedure for stretching and compressing the laser pulse with diffraction gratings, known as Chirped-Pulse-Amplification (CPA) [17], is discussed below. The procedure requires the laser medium to have significant gain bandwidth.

Efficiently energizing a laser with the very low required duty factor (300 ns/8 ms) requires the use of a 'storage laser' material. Generally storage lasers are solid-state and, when used in a high-pulse-rate application, they are strongly limited by heat-removal capabilities. LLNL has been developing a solid-state Yb:S-FAP laser with diode pump lasers and rapid helium gas cooling to address this issue as part of its Inertial Fusion Energy program. The Mercury Laser Project is currently assembling a prototype. The default Mercury laser pulse format differs from that required for $\gamma\gamma$ operation. The necessary modifications of the laser are described below.

5.2 Laser system front end

The laser system front end must generate a low-power laser signal with a temporal format matched to that of the electron linac. This signal will then be delivered to the Mercury amplifiers to generate the high pulse energies needed to interact with the electron pulses.

A laser oscillator will be required with an approximately 350 MHz pulse rate and 2 ps pulse duration. With pulse energies of 1.0 nJ, the average power will only be only 0.35 W. The laser must be tuned to the 1.047 micron wavelength which overlaps the gain bandwidth of the Yb:S-FAP laser amplifiers. Commercial Ti-sapphire lasers will be appropriate for this task. The laser oscillator must have high frequency stability and must be locked to the master clock of the linac so that the laser pulse timing matches that of the electron pulses.

The beam from the oscillator will pass through a Pockels cell slicer that will cut out 300 ns pulse trains at 120 Hz. These batches will match the electron bunch trains, which contain approximately 100 subpulses. The pulse trains will then be passed through an electro-optic modulator that will impose a moderately increasing amplitude ramp on the macro-pulse. This amplitude ramp is designed to offset the decreasing gain ramp that will be experienced in the amplifier as the stored energy is extracted during the laser macro-pulse. The low power (about 1 μW) is easily handled by current EO modulators.

The gain in the amplifier will have frequency variations as well as amplitude diminution during the macro-pulse. To avoid strong amplitude variations at different frequencies in the amplified laser signal, the amplitude of the input laser beam will be sculpted in frequency space [18] to offset the effects of the gain variation. The short pulse length of the subpulses gives them a frequency bandwidth such that a diffraction grating will spread the beam over a range of angles. The different frequencies are then passed through a programmable liquid crystal display that provides different attenuation for different positions (frequencies) in the beam.

The laser beam is next passed through a diffraction grating pulse stretcher, described in a later section, that stretches the 2 ps subpulses to 3 ns. The spectral sculpting and pulse stretching might be combined into a single device if appropriate.

The stretched laser pulses can now be passed through a high-gain, low-power preamplifier. A laser optical parametric amplifier (OPA) will provide the high bandwidth needed to preserve the frequency profile of the laser pulse. A high-pulse energy green laser will pump a BBO crystal to provide the gain needed. The laser beam will be amplified to 500 μJ/subpulse. The beam will be split into twelve 10 Hz beams and then injected into the Mercury amplifiers.

Wavelength	1 μ	Format	$\sim$ 100 subpulses/macro-pulse
Subpulse energy	1 J	Repetition rate	120 Hz
Subpulse separation	2.8 ns	Gain bandwidth	10 nm
Subpulse duration	2 ps	Beam quality	$<$ 1.5 diffraction limit

Table 13.2: $\gamma\gamma$ collider laser requirements.

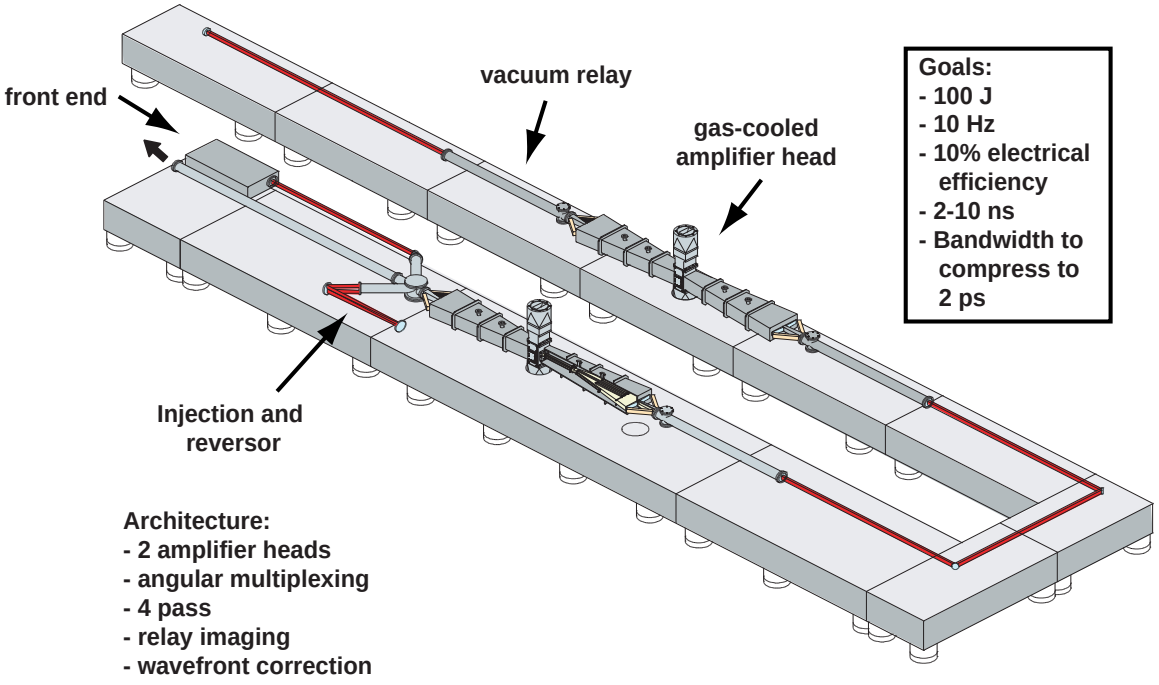

Figure 13.8: The diode-pumped solid state Mercury laser is a high-pulse rate, next-generation laser fusion driver.

5.3 Mercury amplifier

The Mercury laser (Fig. 13.8) will operate at 10 Hz with 100 J pulses. Twelve such lasers would have to be time-multiplexed to achieve the $\gamma\gamma$ laser requirements. The major challenge will be the modification of the Mercury laser pulse format, which is currently a single several-nanosecond-long pulse. Achieving the desired diffraction-limited beam quality will also be an important challenge.

The Mercury laser utilizes three primary innovations to achieve the goal of a high-efficiency, high-repetition-rate laser driver for laser fusion experiments. The first is that the removal of heat from the laser media is accomplished by flowing helium at high speed over the surface of thin laser slabs. The thermal gradients in the laser media are oriented both in the short dimension, for effective conductive cooling, and in the direction of the laser propagation, to minimize the optical distortion. The low index of refraction of helium minimizes the helium thermal-optical distortions that must later be removed with adaptive optics. Figure 13.9 shows the arrangement of thin laser slabs embedded in flow vanes within the helium flow duct. Full-scale demonstrations have validated the flow and thermal models have confirmed that the design meets the optical system requirements.

The second innovation is the use of diode lasers rather than flash lamps to energize

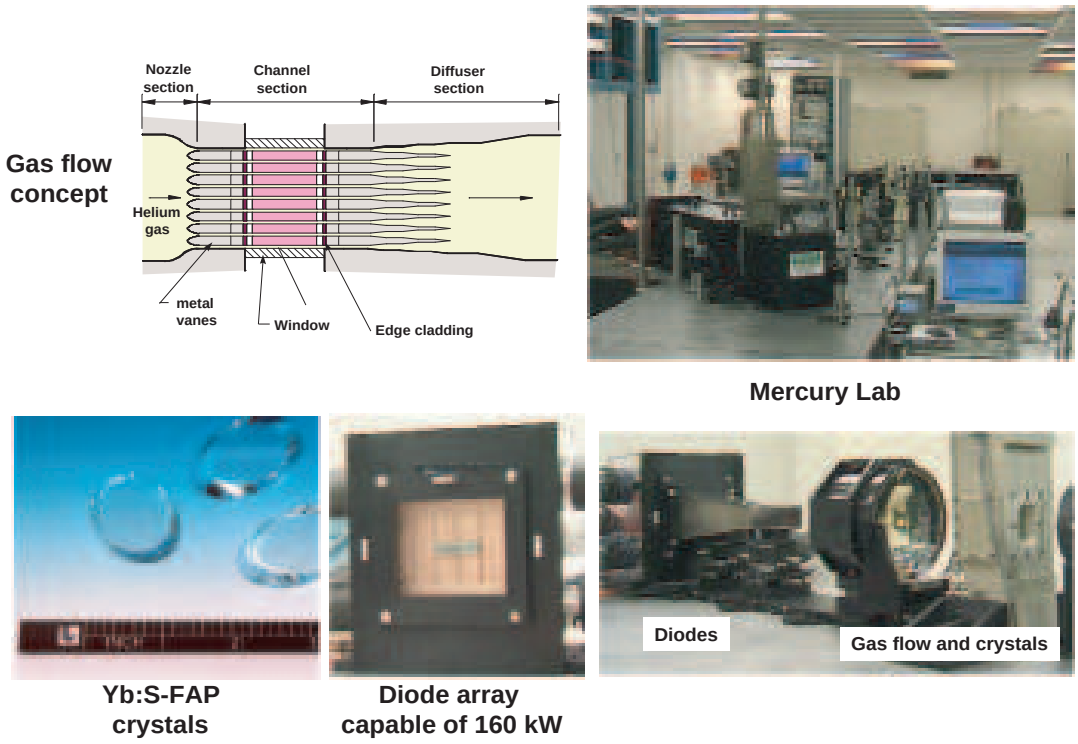

Figure 13.9: The Mercury laser will utilize three key technologies: gas cooling, diodes, and Yb:S-FAP crystals to deliver 100 J at 10 Hz with 10% efficiency.

the laser media. The narrow frequency output of the diode laser is matched to the absorption band of the laser media. The efficient coupling and the efficiency of diode lasers result in significantly higher pumping efficiency of the laser media and also significantly lower waste heat that must be removed by the helium cooling system. The primary challenge for the diode laser design is minimizing the high capital cost of the diode laser and its packaging design. LLNL has developed a low-cost packaging design that also efficiently couples the diode light into the laser slabs. This design has been produced under commercial contract and will be tested this year in the Mercury laser laboratory.

The third innovation is the use of Yb:S-FAP as the laser media instead of the usual Nd-glass. This crystalline media has better thermal conductivity for cooling, longer storage lifetime for efficient pumping, and a high quantum efficiency to minimize waste heat. The growth of these new crystals (Fig. 13.9) with adequate size and optical quality has been the primary technical challenge in the Mercury project. Crystals

grown recently may satisfy these requirements, but some testing remains to be done.

The Mercury laser has two amplifier heads and a four-pass optical system. This year one amplifier head and the full optical configuration will be tested in the Mercury laboratory. A second amplifier head must be constructed before full-power extraction can be demonstrated.

5.4 Multiplexer and beam transport

The beams from twelve Mercury lasers, each operating at 10 Hz, must be combined into a single co-aligned beam to produce the required 120 Hz beam. The beam combination should occur before the pulse compressor to minimize the stress on the combiner optics. At these low pulse rates the simplest beam combination scheme is a simple rotating faceted optic.

The beam combination optic is a 4 cm-diameter optic with twelve flat facets each covering a thirty degree sector. Each facet is ground at a slightly different angle. The optic is rotated on its axis at 10 Hz (600 rpm). The twelve incoming laser beams arrive at slightly different angle, such that they are all aligned after reflection off the optic. The angle differences are sufficiently large to allow the incoming laser beams to be projected from spatially separated optics. The incident laser beam diameter of 0.5 cm will give a power density of 5 kW/cm^2 on the optic. This will be below the damage threshold of 10 kW/cm^2. The optic can be made larger if a larger damage margin is desired.

The combined beam is then transported to the pulse compressor. The pulse compressor can be located in the laser facility or close to the detector, just prior to the final transport optics into the IR. For the reference design it is assumed that the compressor is located in the laser facility and that the laser facility is located a nominal 100 meters from the detector hall. The transport of the laser beams will be in vacuum pipes from the exit of the Mercury laser modules. To minimize the evolution of amplitude variations due to diffraction or phase aberrations, the laser beam will be expanded to a nominal 10 cm and image-relayed. The vacuum tubes should be 15 cm to allow for errors in initial alignment procedures.

5.5 Compressor / stretcher

The basic concept of compressing long pulses into short pulses after amplification is well known and widely used [19,20]. The challenge is in designing and fabricating high-efficiency gratings that can handle high-power laser beams. The specifications for the stretcher and compressor systems are given in Table 13.3.

The subpulses from the oscillator are 2 ps and 1.0 nJ. Their transform-limited full-width-half-maximum is 0.9 nm. The gratings in the stretcher give the beam an angular spread. Light of different wavelengths within the bandwidth of the laser follows optical paths of different length, thus introducing a frequency-time correlation

	Stretcher	Compressor
Substrate material	silica	silica
Coating material	gold	Multi-layer
First grating size (cm)	4 x 15	30 x 84
Second grating size (cm)	4 x 15	30 x 84
Roof mirror size (cm)	4 x 8 (flat)	30 x 40
Grating separation (m)	5	15
Lines per mm	1740	1740
Laser beam diameter (cm)	1	10
Cut bandwidth (nm)	2.0	2.0
Exit subpulse duration (ps)	3000	2.2
Efficiency-single bounce (%)	90.	96.0
System efficiency (%)	60	80
Laser macro-pulse fluence (J/cm^2)	10^{-7}	1.3
Damage fluence (J/cm^2)	0.4	2.0

Table 13.3: Specifications for stretcher and compressor optical systems.

to the subpulse ("chirping"). The laser subpulse has a 3 ns halfwidth duration upon exiting. The finite size of the grating results in the truncation of some frequencies and gives the exiting pulse a truncated spectral distribution and a temporal pulse with side lobes. The 100 subpulses that are separated by 2.8 ns will overlap to form a 300 ns macro-pulse that has some ($\sim 10\%$) time/amplitude modulation. Since the beam in the stretcher is of such low power, there are no technical issues with this system. The system efficiency will be limited by the reflectivity of the gratings in the first order and the frequency clipping due to finite grating size.

The compressor gratings must be designed to handle the full 100 J macro-pulses without damage. The 100 Hz pulse rate will also generate an average-power thermal concern. The large gold coatings used in laser fusion experiments (Fig. 13.10) have too large an absorption and would have thermal distortion problems. LLNL has also developed multi-layer dielectric diffraction gratings with high efficiency [21]. Their low absorptivity removes the thermal concerns while also increasing the system efficiency. Figure 13.10 shows the design of these gratings. Alternating layers of hafnia and silica are placed on the substrate to give a high-reflectivity, high-damage fluence coating. The grating is etched in the silica overcoating.

5.6 Laser facility, systems design and risk reduction

The general layout of the laser facility is shown in Fig. 13.11. The facility is dominated by the operating bays for the laser amplifiers and their utilities. The operating strategy will be to do no laser repairs in these operation bays. The laser

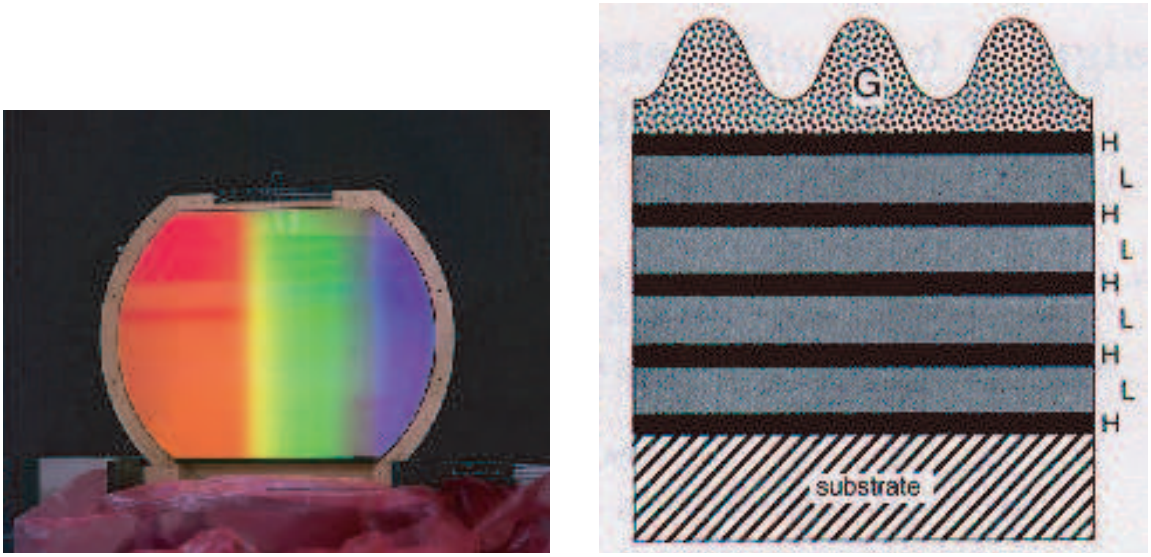

Figure 13.10: The 94 cm aperture gold-coated diffraction grating used for pulse compression on the Petawatt laser is shown on the left. A multilayer dielectric grating design of high-index (H) and low-index (L) layers and groove corrugations (G) is shown on the right. Layers form a high-reflectivity stack under the corrugations.

systems will be designed with quickly removable Line Replaceable Units (LRUs) for all the major subsystems, as in the NIF project. The equipment will be monitored by computer during operation. When a system needs special or preventive maintenance, the LRU is quickly removed and moved to a separate repair facility. A new LRU is inserted, and the laser is immediately returned to service. This repair strategy allows for high system availability without requiring excessive component lifetimes or redundancy. Some long-lifetime components such as the optics vacuum chamber may have to be occasionally repaired in place.

A systematic cost estimate has not yet been done. The expected capital cost is of order of $200M, and the operating budget of approximately $20M/yr. The largest uncertainties in the capital costs are the diode costs and the laser size needed to meet the performance requirements. The operating cost uncertainties are dominated by diode laser lifetime and cost uncertainties.

The cost risk reduction strategy is to identify the main cost drivers. Since diode lifetime is expected to be the primary cost risk driver, efforts will be made to acquire diode lifetime data.

The technical risks are dominated by the laser beam quality uncertainties and the lack of prototype demonstrations of some of the subsystems. The Mercury laser being built for the fusion program will serve as the main laser amplifier prototype. Other critical systems such as the laser system front end will be prototyped as part of a risk

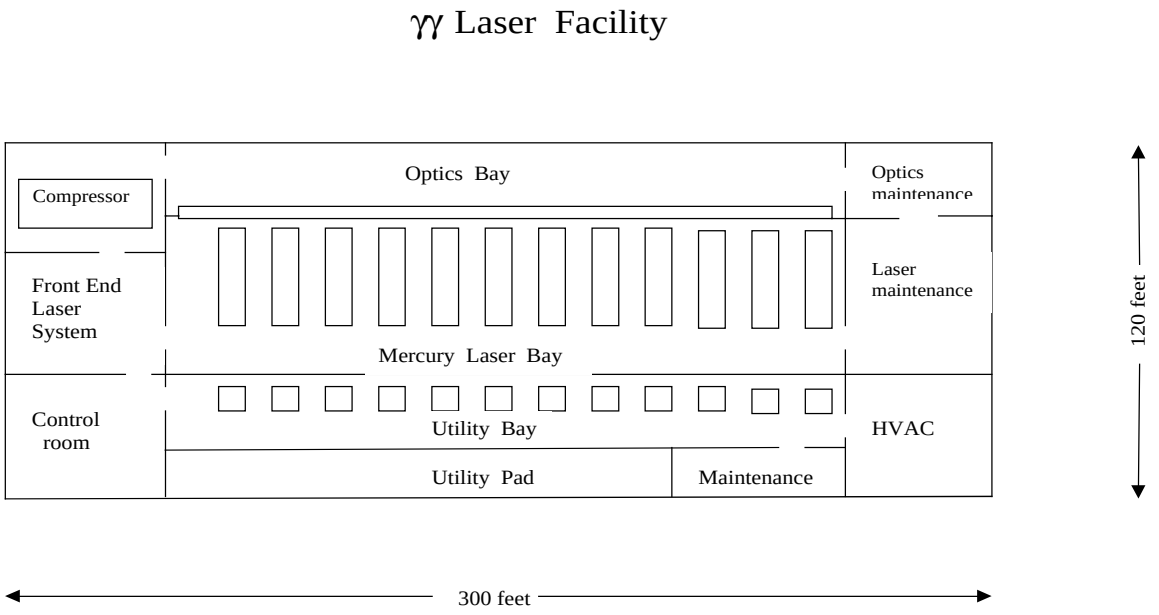

Figure 13.11: Floor plan of the laser physical plant.

reduction program.

References

[1] I. F. Ginzburg, G. L. Kotkin, V. G. Serbo and V. I. Telnov, Pizma ZhETF **34**, 514 (1981); JETP Lett. **34**, 491 (1982) (Preprint INF 81-50, Novosibirsk (1981) in English).

[2] I. F. Ginzburg, G. L. Kotkin, V. G. Serbo and V. I. Telnov, Nucl. Instrum. Meth. **205**, 47 (1983).

[3] D. L. Bordon, D. A. Bauer, and D. O. Caldwell, Phys. Rev. **D48**, 4018 (1993); T. Ohgaki, T. Takahashi and I. Wantanabe, Phys. Rev. **D56**, 1723 (1997); T. Ohgaki, T. Takahashi, I. Wantanabe and T. Tauchi, Int. J. Mod. Phys. **A13**, 2411 (1998); I. Wantanabe *et al.*, KEK Report 97-17 (1998).

[4] J. F. Gunion *et al.*, hep-ph/9703330; H. E. Haber, hep-ph/9505240; A. Djouadi, V. Driesen, W. Hollik and J. I. Illana, E. Phys. J. **C1**, 149 (1998); B. Grzadkowski and J. F. Gunion, Phys. Lett. **B291**, 361 (1992); J. F. Gunion and J. G. Kelly, Phys. Lett. **B333**, 110 (1994).

[5] See, for example, S. Söldner-Rembold and G. Jikia, in *Proc. Internat. Workshop on High-Energy Photon Colliders*, Hamburg, Germany, 14-17 June 2000; G. Jikia

and A. Tkabladze, Phys. Rev. **D54**, 2030 (1996); M. Melles, W. J. Stirling and V. A. Khoze, Phys. Rev. **D61**, 054015 (2000) and M. Melles, hep-ph/0008125; M. Battaglia, hep-ph/9910271.

[6] E. Yehudai, Phys. Rev. **D41**, 33 (1990) and **D44**, 3434 (1991); S. Y. Choi and F. Schrempp, Phys. Lett. **B272**, 149 (1991); S. J. Brodsky, T. G. Rizzo and I. Schmidt, Phys. Rev. **D52**, 4929 (1995); T. Takahashi, in *Physics and Experiments with Linear Colliders*, ed. A. Miyamoto *et al.* (World Scientific, Singapore, 1996); M. Baillargeon, G. Belanger and F. Boudjema, Nucl. Phys. **B500**, 224 (1997). For a review, see H. Aihara *et al.* in *Electroweak Symmetry Breaking and Beyond the Standard Model*, ed. T. Barklow *et al.*, (World Scientific, Singapore, 1996).

[7] N. Arkani-Hamed, S. Dimopoulos and G. Dvali, Phys. Lett. **B429**, 263 (1998) and Phys. Rev. **D59**, 086004 (1999); I. Antoniadis, N. Arkani-Hamed, S. Dimopoulos and G. Dvali, Phys. Lett. **B436**, 257 (1998); G. F. Giudice, R. Rattazzi and J. D. Wells, Nucl. Phys. **B544**, 3 (1999); T. Han, J. D. Lykken and R. Zhang, Phys. Rev. **D59**, 105006 (1999), E. A. Mirabelli, M. Perelstein and M. E. Peskin, Phys. Rev. Lett. **82**, 2236 (1999); J. L. Hewett, Phys. Rev. Lett. **82**, 4765 (1999); T. G. Rizzo, Phys. Rev. **D59**, 115010 (1999).

[8] T. G. Rizzo, Phys. Rev. **D60**, 115010 (1999).

[9] L. Randall and R. Sundrum, Phys. Rev. Lett. **83**, 3370 (1999). H. Davoudiasl, J. L. Hewett and T. G. Rizzo, Phys. Lett. **B473**, 43 (2000), hep-ph/0006041 and Phys. Rev. Lett. **84**, 2080 (2000).

[10] A. Djouadi, *Proc. of the Workshop on e^+e^- collisions at 500 GeV: the Physics Potential*, edited by P. Zerwas, DESY Report 92-123B; P. Poulose and S. D. Rindani, Phys. Lett. **B452**, 347 (1999); S. Y. Choi and Hagiwara, Phys. Lett. **B359**, 369 (1995); M. S. Baek, S. Y. Choi and C. S. Kim, Phys. Rev. **D56**, 6835 (1997).

[11] For a recent review and original references, see G. J. Gounaris, P. I. Porfyiadis and F.M. Renard, hep-ph/0010006.

[12] J. L. Hewett, F. J. Petriello and T. G. Rizzo, hep-ph/0010354.

[13] For a review, see A. Djoudai, J. Ng and T. G. Rizzo, in *Electroweak Symmetry Breaking and Beyond the Standard Model*, ed. T. Barklow *et al.*, (World Scientific, Singapore, 1996); W. Buchmüller, R. Rückl and D. Wyler, Phys. Lett. **B191**, 442 (1987); J. L. Hewett and T. G. Rizzo, Phys. Rev. **183**, 193 (1989) and Phys. Rev. **D56**, 5709 (1997); J. Blümlein and R. Rückl, Phys. Lett. **B304**, 337 (1993); S. Davidson, D. Bailey, and B. A. Campbell, Z. Phys. **C61**, 613 (1994); M. Leurer, Phys. Rev. **D50**, 536 (1994), and **D49**, 333 (1994).

[14] For a recent summary, see D. S. Gorbunov, V. A. Ilyin and V. I. Telnov, hep-ph/0012175.

[15] V. Telnov, Nucl. Instr. and Meth. **A 355**, 3 (1995).

[16] K. Yokoya, "A Computer Simulation Code for the Beam-Beam Interaction in Linear Colliders", KEK report 85-9, Oct. 1985.

[17] D. Strickland and G. Mourou, Opt. Commun. **56**, 219 (1985).

[18] M. D. Perry, F. G. Patterson, and J. Weston, Opt. Lett. **15**, 381 (1990)

[19] E. B. Treacy, IEEE J.Quantum Electron. **QE-5**, 454 (1969).

[20] M. D. Perry and G. Mourou, Science **264**, 917 (1994).

[21] B. W. Shore, M. D. Perry, J. A. Britten, R. D. Boyd, M. D. Feit, H. T. Nguyen, R. Chow, G. E. Loomis and Lifeng Li, J. Opt. Soc. Am., **14**, No.5, 1124 (May 1997).

Chapter 14 e^-e^- Collisions

1 General characteristics of e^-e^- collisions

The primary goal of the linear collider program will be to elucidate new physics at the weak scale. The e^-e^- collider brings a number of strengths to this program. Electron-electron collisions are characterized by several unique features:

• *Exactly Specified Initial States and Flexibility.* For precision measurements, complete knowledge of the initial state is a great virtue. This information is provided optimally in e^-e^- collisions. The initial state energy is well-known for both e^+ and e^- beams, despite small radiative tails due to initial state radiation and beamstrahlung. For e^- beams, however, 85% polarization is routinely obtainable now, and 90% appears to be within reach for linear colliders. The three possible polarization combinations allow one to completely specify the spin S_z, weak isospin I_w^3, and hypercharge Y of the initial state. One may also switch between these combinations with ease and incomparable flexibility.

• *Extreme Cleanliness.* Backgrounds are typically highly suppressed in e^-e^- collisions. The typical annihilation processes of e^+e^- collisions are absent. In addition, processes involving W bosons, often an important background in e^+e^- collisions, may be greatly suppressed by right-polarizing *both* beams.

• *Dictatorship of Leptons.* In e^+e^- collisions, particles are produced 'democratically'. In contrast, the initial state of e^-e^- collisions has lepton number $L = 2$, electron number $L_e = 2$, and electric charge $Q = -2$.

With respect to the first two properties, the e^-e^- collider takes the linear collider concept to its logical end. The third property precludes many processes available in e^+e^- interactions, but also provides unique opportunities for the study of certain types of new physics, such as supersymmetry. The physics motivations for the e^-e^- collider have been elaborated in a series of workshops over the past six years [1–3]. In the following, we briefly describe a number of possibilities for new physics in which e^-e^- collisions provide information beyond what is possible in other experimental settings. We then review the accelerator and experimental issues relevant for e^-e^- collisions.

2 Physics at e^-e^- colliders

2.1 Møller scattering

The process $e^-e^- \to e^-e^-$ is, of course, present in the standard model. At e^-e^- colliders, the ability to polarize both beams makes it possible to exploit this process fully.

One may, for example, define two left-right asymmetries

$$A_{LR}^{(1)} \equiv \frac{d\sigma_{LL} + d\sigma_{LR} - d\sigma_{RL} - d\sigma_{RR}}{d\sigma_{LL} + d\sigma_{LR} + d\sigma_{RL} + d\sigma_{RR}}$$

$$A_{LR}^{(2)} \equiv \frac{d\sigma_{LL} - d\sigma_{RR}}{d\sigma_{LL} + d\sigma_{RR}} , \tag{14.1}$$

where $d\sigma_{ij}$ is the differential cross section for $e_i^- e_j^- \to e^-e^-$ scattering. There are four possible beam polarization configurations. The number of events in each of the four configurations, N_{ij}, depends on the two beam polarizations P_1 and P_2. Given the standard model value for $A_{LR}^{(1)}$, the values of N_{ij} allow one to simultaneously determine P_1, P_2, and $A_{LR}^{(2)}$. For polarizations $P_1 \simeq P_2 \simeq 90\%$, integrated luminosity 10 fb^{-1}, and $\sqrt{s} = 500$ GeV, the beam polarizations may be determined to $\Delta P/P \approx 1\%$ [4,5]. Such a measurement is comparable to precisions achieved with Compton polarimetry, and has the advantage that it is a direct measurement of beam polarization at the interaction point.

This analysis also yields a determination of $A_{LR}^{(2)}$, as noted above. Any inconsistency with the standard model prediction is then a signal of new physics. For example, one might consider the possibility of electron compositeness, parameterized by the dimension-six operator $\mathcal{L}_{\rm eff} = \frac{2\pi}{\Lambda^2}\overline{e}_L\gamma^\mu e_L\overline{e}_L\gamma_\mu e_L$. With $\sqrt{s} = 1$ TeV and an 82 fb^{-1} event sample, an e^-e^- collider is sensitive to scales as high as $\Lambda = 150$ TeV [6]. The analogous reach for Bhabha scattering at e^+e^- colliders with equivalent luminosity is roughly $\Lambda = 100$ TeV.

2.2 Higgs bosons

The Higgs boson production mechanism $e^+e^- \to Zh$ in the e^+e^- mode is complemented by production through WW and ZZ fusion in both e^+e^- and e^-e^- colliders. The study of $e^-e^- \to e^-e^-h^0$ through ZZ fusion has a number of advantages [7,8]. The cross section is large at high energy, since it does not fall off as $1/s$. The usual backgrounds from e^+e^- annihilation are absent. The final electrons typically have transverse momenta of order m_Z. Thus, one can reconstruct the recoil mass and observe the Higgs boson in this distribution, as shown in Fig. 14.1. Invisible decays of the Higgs boson, and branching ratios more generally, can be studied by this technique.

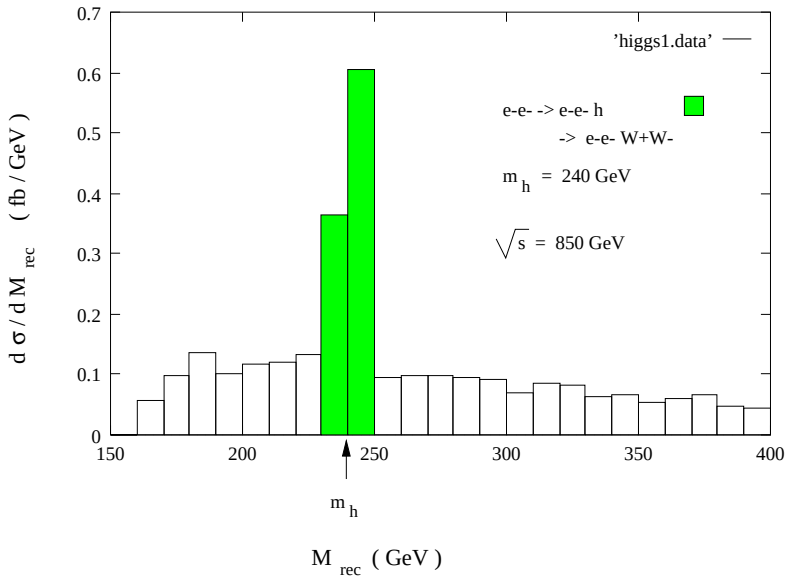

Figure 14.1: Differential cross sections as functions of recoil mass for $e^-e^- \to e^-e^-h$ and its principal standard model background $e^-e^- \to e^-e^-W^+W^-$. The Higgs boson mass is $m_h = 240$ GeV, $\sqrt{s} = 850$ GeV, and each electron satisfies an angular cut $\theta_{e^-} > 5°$. From [7].

2.3 Supersymmetry

The e^-e^- mode is an ideal setting for studies of sleptons. All supersymmetric models contain Majorana fermions that couple to electrons—the electroweak gauginos $\widetilde{B}$ and $\widetilde{W}$. Slepton pair production is therefore always possible [9], while all potential backgrounds are absent or highly suppressed. Precision measurements of slepton masses, slepton flavor mixings, and slepton couplings in the e^-e^- mode are typically far superior to those possible in the e^+e^- mode. Studies of all of these possibilities are reviewed in Chapter 4, Section 6.1.

The e^-e^- collider may also be used to determine the properties of other superpartners. For example, the production of right-handed selectron pairs is highly sensitive to the Majorana Bino mass M_1 that enters in the t-channel (see Fig. 14.2). As a consequence, extremely high Bino masses M_1 may be measured through the cross section of $\tilde{e}_R^-$ pair production [10]. This region of parameter space is difficult to access in other ways.

2.4 Bileptons

The peculiar initial state quantum numbers of e^-e^- colliders make them uniquely suited for the exploration of a variety of exotic phenomena. Among these are bilep-

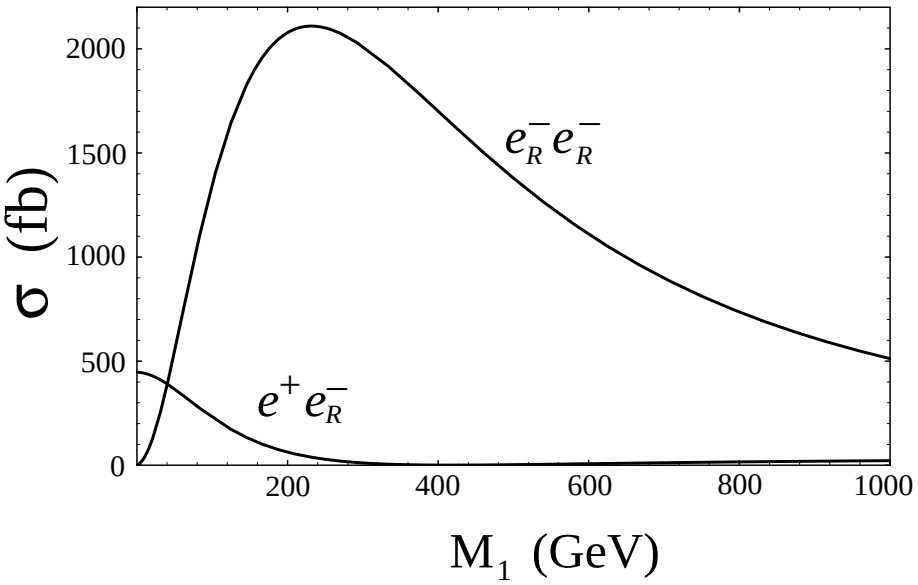

Figure 14.2: The total selectron pair production cross sections for the $e_R^- e_R^-$ and $e^+ e_R^-$ modes with $m_{\tilde{e}_R} = 150$ GeV and $\sqrt{s} = 500$ GeV, as functions of the Bino mass M_1. From [10].

tons, particles with lepton number $L = \pm 2$. Such particles appear, for example, in models where the $SU(2)_L$ gauge group is extended to SU(3) [11], and the Lagrangian contains the terms

$$\mathcal{L} \supset \left(\begin{array}{ccc} \ell^- & \nu & \ell^+ \end{array} \right)_L^* \left(\begin{array}{ccc} & & Y^{--} \\ & & Y^- \\ Y^{++} & Y^+ & \end{array} \right) \left(\begin{array}{c} \ell^- \\ \nu \\ \ell^+ \end{array} \right)_L , \tag{14.2}$$

where Y are new gauge bosons. Y^{--} may then be produced as an s-channel resonance at e^-e^- colliders, mediating background-free events like $e^-e^- \to Y^{--} \to \mu^-\mu^-$. Clearly the e^-e^- collider is ideal for such studies.

Bileptons may also appear in models with extended Higgs sectors that contain doubly charged Higgs bosons H^{--}. In these models, both types of particles are produced as resonances in e^-e^- scattering. However, the types of states are clearly distinguished by initial state polarization: bileptons are produced from initial polarization states with $|J_z| = 1$, while doubly charged Higgs particles are produced in channels with $J_z = 0$. The potential of e^-e^- colliders to probe the full spectrum of these models is reviewed in [12].

2.5 Other physics

In addition to these topics, the potential of e^-e^- colliders has also been studied as a probe of strong W^-W^- scattering, anomalous trilinear and quartic gauge boson

couplings, heavy Majorana neutrinos, leptoquarks, heavy Z' bosons, TeV-scale gravity and Kaluza-Klein states, and non-commuting spacetime observables. These topics and other possibilities are discussed in [1–3].

3 Accelerator and experimental issues

3.1 Machine design

There are at present two well-developed approaches to linear collider architecture in the 0.35 to 1 TeV energy range: the NLC/JLC and TESLA designs. Both approaches are easily adaptable to make both e^+e^- and e^-e^- collisions available with relatively little overhead.

The general layout of the NLC design is given in Fig. 14.3. The careful inclusion of the e^-e^- design is described in [13]. The installation of a second polarized electron source presents no difficulty, but magnet polarity reversals and potential spin rotators need to be carefully optimized.

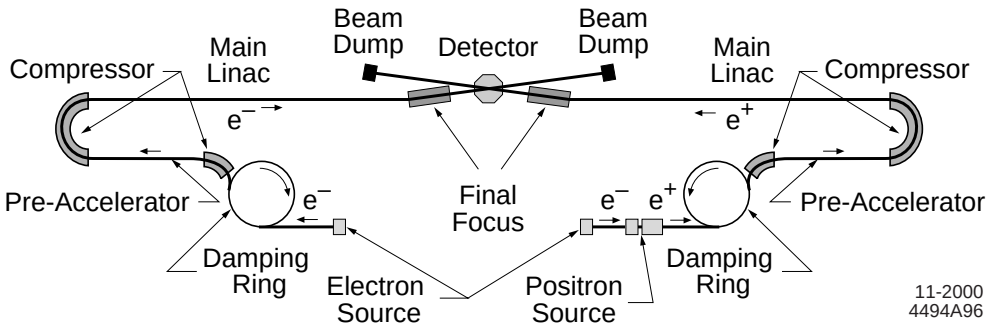

Figure 14.3: Schematic of the NLC. From [13].

Three different modifications for the injection area on the "positron" side have been investigated [14]. We show one of these in Fig. 14.4. In this scheme, the damping ring and bunch compressor for the e^+ beam are used for an e^- beam which circulates in the opposite direction. A new electron gun and some additional components for injection and extraction are needed, but the cost of these is modest, and the switchover from e^+ to e^- operation can be accomplished without significant manual intervention.

For the TESLA project, it is even simpler to introduce polarized e^- through the e^+ injection system. A new polarized electron source is needed, and new components are needed for injection and extraction from the existing positron 'dogbone' damping ring [15]. The positions of these new devices mirror the positions of the electron injection and extraction points on the other side of the machine.

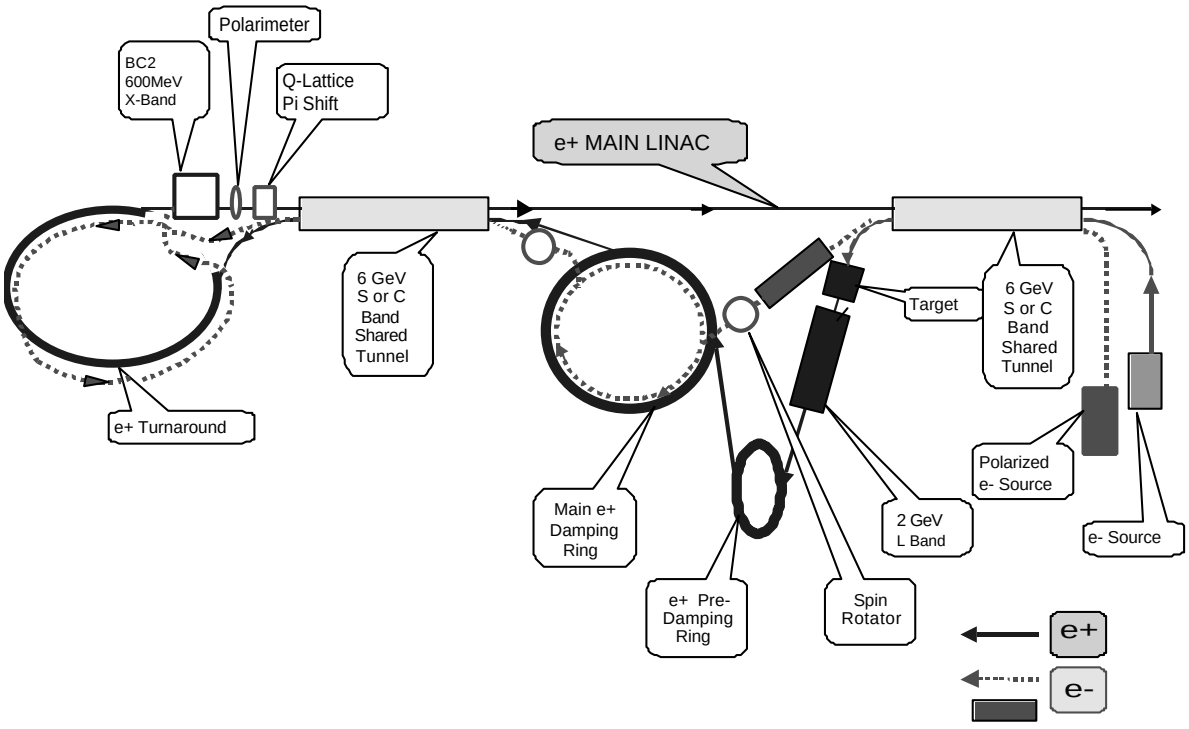

Figure 14.4: The direction reversal model. From [14].

Similar considerations apply to the higher-energy CLIC proposal [16]. As with NLC/JLC and TESLA, the main difficulties involve the injection scheme; once appropriate components are provided, the acceleration of e^- beams and the switchover from e^+e^- to e^-e^- should be straightforward.

3.2 Interaction region

Although e^-e^- operation is straightforwardly incorporated in linear collider designs, experimentation at e^-e^- colliders is not entirely equivalent to that at e^+e^- colliders. This is because the luminosity of the collider is decreased significantly by beam disruption due to the electromagnetic repulsion of the two e^- beams.

Clever manipulation of the beam parameters can minimize the relative luminosity loss; see, for example, [17]. The resulting parameters give about a factor 3 loss for NLC/JLC and a factor 5 loss for TESLA, and do not much reduce the merits of the proposed e^-e^- studies. A plasma lens [18,19] has been proposed to reduce the disruption effects, but this would introduce a serious level of beam-gas backgrounds.

The beamstrahlung effect in e^-e^- is somewhat larger than that in e^+e^- due to the larger disruption, leading to a stronger effective field from the opposite beam. The effect is still modest in size for 500 GeV CM energy. Figure 14.5 shows a comparison of the e^-e^- and e^+e^- cases for the TESLA machine design [20].

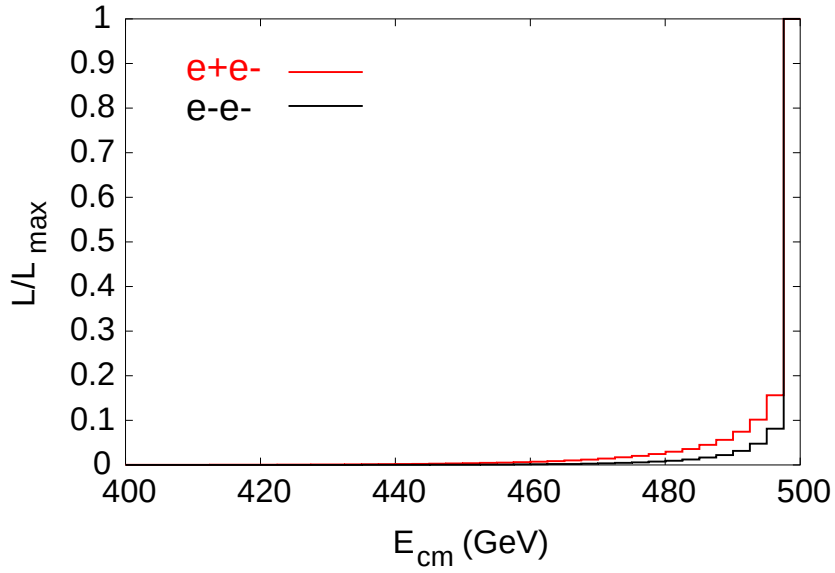

Figure 14.5: Normalized luminosity spectrum for e^-e^- collisions compared to e^+e^-. From [20].

3.3 Detectors

It is important to realize that the detector configuration is easily shared for e^+e^- and e^-e^- experimentation. A caveat exists for beam disposal downstream of the interaction point: if there is any bend upstream of this point, like-sign incoming beams will *not* follow the incoming trajectories of the opposite side, and special beam dumps may have to be configured.

If the linear collider program plans to incorporate $e\gamma$ and $\gamma\gamma$ collisions, with backscattered photon beams, the photon beams must be created from e^- rather than e^+ beams, so that the electron beam polarization can be used to optimize the energy spectrum and polarization of the photon beams. Photon colliders of course have their own, very different, requirements for interaction regions and detectors. These are described in Chapter 13, Section 3.

4 Conclusions

For a number of interesting physics scenarios, the unique properties of e^-e^- colliders will provide additional information through new channels and observables. While the specific scenario realized in nature is yet to be determined, these additional tools may prove extremely valuable in elucidating the physics of the weak scale and beyond. Given the similarities of the e^+e^- and e^-e^- colliders, it should be possible with some

thought in advance to guarantee the compatibility of these two modes of operation and the ease of switching between them. For many possibilities for new physics in the energy region of the linear collider, the small effort to ensure the availability of e^-e^- collisions should reap great benefits.

References

[1] *Proceedings of the 1st International Workshop on Electron-Electron Interactions at TeV Energies (e^-e^-95)*, Santa Cruz, California, 5–6 September 1995, ed. C. A. Heusch, Int. J. Mod. Phys. **A11**, 1523-1697 (1996).

[2] *Proceedings of the 2nd International Workshop on Electron-Electron Interactions at TeV Energies (e^-e^-97)*, Santa Cruz, California, 22–24 September 1997, ed. C. A. Heusch, Int. J. Mod. Phys. **A13**, 2217-2549 (1998).

[3] *Proceedings of the 3nd International Workshop on Electron-Electron Interactions at TeV Energies (e^-e^-99)*, Santa Cruz, California, 10–12 December 1999, ed. C. A. Heusch, Int. J. Mod. Phys. **A15**, 2347-2628 (2000).

[4] F. Cuypers and P. Gambino, Phys. Lett. **B388**, 211 (1996) [hep-ph/9606391].

[5] A. Czarnecki and W. J. Marciano, Int. J. Mod. Phys. **A13**, 2235 (1998) [hep-ph/9801394].

[6] T. L. Barklow, Int. J. Mod. Phys. **A11**, 1579 (1996).

[7] P. Minkowski, Int. J. Mod. Phys. **13**, 2255 (1998).

[8] J. F. Gunion, T. Han and R. Sobey, Phys. Lett. **B429**, 79 (1998) [hep-ph/9801317].

[9] W. Y. Keung and L. Littenberg, Phys. Rev. **D28**, 1067 (1983).

[10] J. L. Feng, Int. J. Mod. Phys. **A13**, 2319 (1998) [hep-ph/9803319].

[11] P. H. Frampton, Int. J. Mod. Phys. **A13**, 2345 (1998) [hep-ph/9711281].

[12] J. F. Gunion, Int. J. Mod. Phys. **A13**, 2277 (1998) [hep-ph/9803222].

[13] P. Tenenbaum, Int. J. Mod. Phys. **A15**, 2461 (2000).

[14] R. S. Larsen, Int. J. Mod. Phys. **A15**, 2477 (2000).

[15] J. Andruszkow, *et al.*, "TESLA Technical Design Report" (DESY 2001-011/ECFA 2001-209) Vol. II, Chapter 5.

[16] J. P. Delahaye *et al.*, CERN/PS 98-009 (1998).

[17] K. A. Thompson, Int. J. Mod. Phys. **A15**, 2485 (2000).

[18] P. Chen, A. Spitkovsky and A. W. Weidemann, Int. J. Mod. Phys. **A11**, 1687 (1996).

[19] J. S. Ng *et al.*, SLAC-PUB-8565, Invited talk presented at the 9th Workshop on Advanced Accelerator Concepts, Santa Fe, New Mexico, 11-16 June 2000.

[20] I. Reyzl and S. Schreiber, Int. J. Mod. Phys. **A15**, 2495 (2000).

Detectors for the Linear Collider

Chapter 15 Detectors for the Linear Collider

1 Introduction

The linear collider detector must be optimized for physics performance, taking consideration of its special environment. To plan for this detector, we consider the physics requirements of the linear collider and build on the experience of operating SLD at the SLC.

The detector must be hermetic, with good charged-track momentum and impact parameter resolution. The calorimeter must provide good resolution, with good granularity, particularly in the electromagnetic section. Electron and muon identification must be done efficiently.

The beamline conditions of the linear collider motivate a strong solenoidal magnetic field to contain the vast number of low-energy electron-positron pairs. There must be provision for an accurate measurement of the differential luminosity, and for timing information that will be useful to separate interactions from separate bunches within a bunch train.

This chapter begins with a discussion of the major issues for the linear collider detector, starting from the beamline conditions and working through the subsystems. Following this discussion, three potential detectors developed for the NLC are described, two designed for the higher-energy IR, and the third for the second IR, where the lower-energy operation is foreseen. Other detectors have been considered in Europe [1] and Asia [2].

These detector studies have been undertaken to understand how well the diverse physics measurements at a linear collider can be accomplished, to provide preliminary guidance on costs, and to highlight areas where R&D is needed. The specific choices of technology and full detector optimization will await the formation of LC experimental collaborations.

2 Interaction region issues for the detector

2.1 Time structure.

The NLC is expected to operate with trains of 190 bunches with 1.4 ns bunch spacing. This time structure requires that the beams cross at an angle. It also affects the number of bunches seen within the integration time of any detector subcomponent and has a strong influence on the types of feedback schemes that can be used to keep the beams in collision.

Crossing angle and parasitic collisions. In order to avoid parasitic collisions, a crossing angle between the colliding beams is required. The minimum angle acceptable for this beam-beam limit is approximately 4 mrad for the NLC parameters. A larger angle is desirable because it permits a more straightforward extraction of the spent beams (see Fig. 15.1), but an excessively large crossing angle will result in a luminosity loss. The angle between the beams chosen in the NLC design is 20 mrad.

The bunches must interact head-to-head or there will be a substantial loss of luminosity. RF cavities that rotate each bunch transversely will be located 10–20 m on either side of the IP. At 20 mrad crossing angle, the relative phasing of the two RF pulses must be accurate to within 10 μm to limit the luminosity loss to less than 2%. This corresponds to 0.04 degrees of phase at S-band (2.8 GHz). The achievable resolution is about 0.02 degrees, which sets an upper limit on the crossing angle of 40 mrad.

Solenoid field effects. The crossing angle in the x–z plane causes the beam to see a transverse component of the detector's solenoid field. If uncorrected, this field will deflect the beams so they do not collide. Likewise, the deflection would cause dispersion that would blow up the beam spot size. Both of these effects can be cancelled by judiciously offsetting the position of the last quadrupole, QD0, and steering the beam appropriately. Synchrotron radiation emission in the transverse field leads to an irreducible increase in spot size. This effect is proportional to $(L^* B_S \theta_C)^{5/2}$, where L^* is the distance between the IP face of the last magnet and the interaction point. While it is small at the values of L^*, B_S, and θ_C considered to date, this effect might someday limit the design of the detector and IR.

After the beams collide at the IP, they are further bent by the solenoid field. Since compensating for this energy-dependent position and angle change with independent dipoles is difficult, the extraction line must be adjusted appropriately for the chosen beam energy. Realignment will be required if the extraction line does not have adequate dynamic aperture to accommodate the full range of beam energies used in experiments.

Finally, if the permeability of QD0 is not exactly unity, the field gradient of the solenoid in the detector endcap region will result in forces on QD0 that will need to be compensated. This may influence the schemes considered to compensate for nanometer-level vibration compensation of the magnet.

2.2 IR layout

Magnet technology. The NLC/JLC and TESLA designs have chosen to use different technologies for the final quadrupole doublet. The choices are dictated by the choice of crossing angle, and by the scheme to extract the spent beam after the collision. The NLC approach is to extract outside the outer radius of a compact Rare Earth Cobalt (REC) magnet into an extraction line that begins 6 m from the IP. The REC of choice is Sm_2 Co_{17}, because of its radiation-resistant properties. Since the

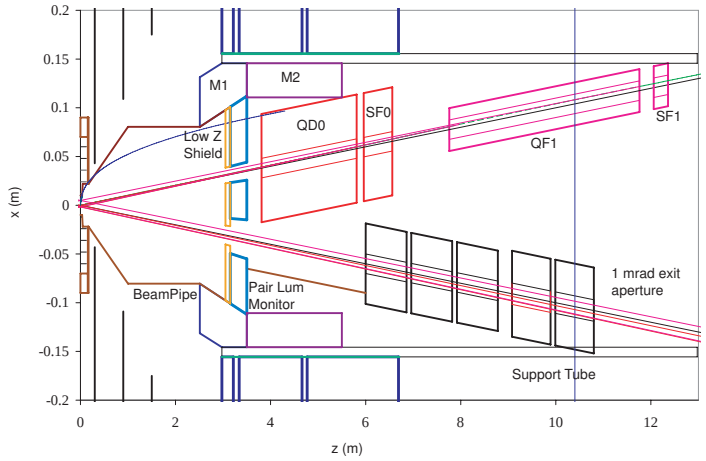

Figure 15.1: IR Layout for the NLC Large Detector.

final quadrupoles can be made light and stiff and have no external power connections, they are well suited for vibration stabilization. The downside to this choice is a lack of flexibility. Other issues that need to be explored further are the compatibility of the REC material with the solenoid field of the detector and the variation of the magnetic field with temperature.

In the current design $L^* = 3.8$ m. An additional 30 cm of free space has been left in front of the pair luminosity monitor to allow for different magnet configurations as the beam energy is increased. Increasing L^* provides more transverse space for the final quads and moves their mounting points further outside the detector, where they can presumably be better stabilized. By keeping L^* larger than the minimum z of the endcap calorimeter, the heavy W/Si-instrumented mask described below can be better incorporated into the detector's acceptance and mechanical structure. By increasing the distance between the IP and the first piece of high-Z material seen by the beam, one can minimize the effect of backscattered debris from the interaction of off-energy e^+e^- pairs created when the beams interact.

On the other hand, increasing L^* tightens the tolerances of the Final Focus optics and reduces its bandwidth. Synchrotron radiation produced by beam halo particles in the final lenses determines the minimum radius of the beam pipe inside the vertex detector. The larger L^* is, the larger will be the fan of photons shining on the vertex detector.

Masks. The electrons and positrons produced in pairs in the beam-beam interaction have a mean energy of about 13 GeV at $\sqrt{s} = 1$ TeV. These off-energy particles spiral in the detector's solenoid field and strike the pair-luminosity monitor or the inner bore of the extraction line magnet. The main purpose of the masking is to

shield the detector from the secondary particle debris produced when an $e^{\pm}$ interacts. There are three masks foreseen. M1 begins at the back of the pair luminosity monitor and extends 0.64 m in z beyond its front face; its inner angle is set by the requirement that it stay just outside the so-called "dead cone" through which the pairs coming from the IP travel. With the mask tip at 2.5 m, a 3 T field requires an inner angle of 32 mrad. This mask would ideally be made of W/Si and be fully integrated with the detector's calorimetry. M2 is a simple tungsten cylinder. The last mask near the IP is a 10–50 cm layer of low-Z material (*e.g.*, Be or C) that absorbs low energy charged particles and neutrons produced when the pairs hit the front face of the W/Si pair luminosity monitor. The very low-energy charged secondaries would otherwise flow back along the solenoid's field lines toward the vertex detector (VXD) and produce unacceptable backgrounds.

2.3 Small spot size issues

The beams must be held stable with respect to one another in the vertical plane at the level of one nanometer. Measurements in existing detectors imply that the mounting of the final quadrupoles may have to correct as much as 50 nm of vibration, caused mostly by local vibration sources and to a much lesser extent by naturally occurring seismic ground motion. Concerns about vibrations caused by moving fluids lead to the choice of permanent magnets for QD0 and QF1. These magnets will be mounted in cam-driven mover assemblies and the beam-beam interaction used to control their position to compensate for disturbances at frequencies below about $f/20$, where f is the beam repetition rate of 120 Hz.

For frequencies above 5–6 Hz, the NLC strategy for stabilizing luminosity relies on a combination of passive compliance (minimizing and passively suppressing vibration sources while engineering to avoid resonant behavior) and active suppression techniques. Quad motion will be measured either optically relative to the surrounding bedrock or inertially, and a correction will be applied to either the final doublet position (via an independent set of magnet movers) or its field center (via a corrector coil). Finally, there will be feedback based on the measured beam-beam deflection. Such a system can respond sufficiently rapidly (within 15 ns) to correct the trailing bunches in a train, once the first few are used to measure any collision offset.

2.4 The beam-beam interaction

The two main experimental consequences of the beam-beam interaction are a broadening of the energy distribution, due to the emission of photons by one beam in the field of the oncoming beam, and the subsequent background generated by interactions of those photons. The beamstrahlung contribution to the energy spread must be considered together with the intrinsic energy spread of the accelerator and the effect of initial state radiation. These effects have been taken into account in the

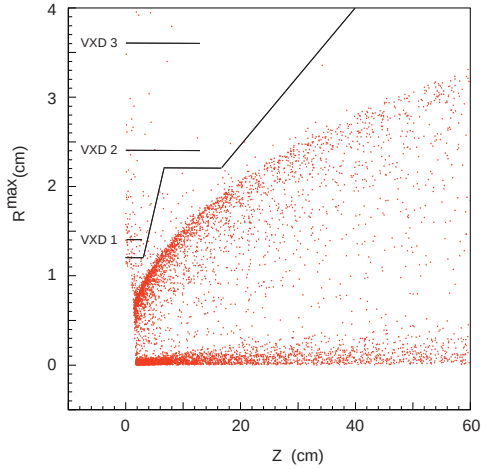

Figure 15.2: $R_{\rm max}$ vs. z distribution of pairs in a 3 Tesla solenoid field. $R_{\rm max}$ is the maximum radius the particle travels from the IP, plotted at the z corresponding to the first apex of its helical trajectory.

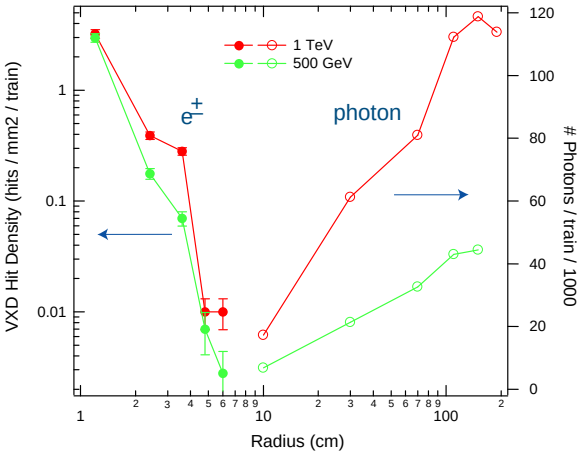

Figure 15.3: Charged particle hit density per train in the VXD, and the absolute number of photons per train entering the TPC within $|\cos\theta| < 0.92$, as function of radius.

discussion of the various physics process. Below we discuss the beam-beam interaction as a potential source of backgrounds.

e^+e^- pairs and the minimum solenoid field. The incoherent production of e^+e^- pairs arising from Bethe-Heitler ($e^\pm\gamma \to e^\pm e^+e^-$), Breit-Wheeler ($\gamma\gamma \to e^+e^-$), and Landau-Lifshitz ($e^+e^- \to e^+e^-e^+e^-$) processes is the main source of background at the present generation of planned linear colliders. At CM energies of 1 TeV, roughly 10^5 particles are produced each bunch crossing, with a mean energy of 13 GeV. Very few particles are produced at a large angle and the dominant deflection is due to the collective field of the oncoming beam. The so-called 'dead cone' that is filled by these particles is clear in the $R_{\rm max}$ vs. z plot in Fig. 15.2. The beam pipe inside the VXD innermost layer must be large enough and short enough that it does not intersect this region.

Secondary particles and their sources. Secondary particle backgrounds—from neutrons, photons, and charged particles—can be a problem for the detector whenever primary particles or particles from the collision are lost close to the IP. The main purpose of the masking described earlier is to limit the backgrounds these secondaries produce. Figure 15.3 shows the charged particle hit density per train in the VXD as a function of radius, and the absolute number of photons per train entering the TPC within $|\cos\theta| < 0.92$. The most important sources of secondary particles are as follows:

- e^+e^- pairs striking the pair luminosity monitor are the most important source

of secondaries as the pairs are well off the nominal beam energy, spiral in the detector's field and strike high-Z materials close to the IP. Backgrounds from this process are controlled by the masks described above.

- Radiative Bhabhas are a source of off-energy particles that are outside the energy acceptance of the extraction line. However, they are sufficiently few in number and leave the beam line sufficiently far from the IP that they are not an important background for the main detector elements.

- The low-energy tail of the disrupted beam cannot be transported all the way to the dump. The current design of the extraction line includes a chicane to move the charged beam transversely relative to the neutral beam of beamstrahlung photons. The bends at the beginning and the end of the chicane are the primary locations where particles are lost. The number of particles lost, $\sim 0.25\%$ of the beam, and the separation of the loss point from the IP makes this an unimportant background source for the main detector, but calls into question the viability of sophisticated instrumentation, such as a polarimeter and an energy spectrometer, in the extraction line.

- Neutrons shining back on the detector from the dump are controlled by shielding immediately surrounding the dump, placing concrete plugs at the tunnel mouths, maximizing the distance from the dump to the IP, and minimizing window penetrations in the concrete. The detector of most concern is the VXD, which can look into the dump with an aperture equal to that provided to accommodate the outgoing beamstrahlung photons and synchrotron radiation.

Beamstrahlung photons. At 500 GeV, 5% of the beam power is transformed into beamstrahlung photons; this rises to 10% at 1 TeV. The IR is designed so that these photons pass unimpeded to a dump. This consideration, along with the angular spread of the synchrotron radiation (SR) photons, determines the exit aperture of the extraction line, currently set at 1 mrad. The maximum transverse size of the dump window that can be engineered and the beamstrahlung angular spread set the maximum distance the dump can be located from the IP. That distance and the size of the aperture in the concrete blockhouse surrounding the dump determine the level of neutron backshine at the detector.

Hadrons from $\gamma\gamma$ interactions. Beamstrahlung photon interactions will also produce hadrons. For the TESLA 500 GeV IP parameters it is estimated that there is a 2% probability per bunch crossing of producing a hadronic event with $p_{T\,\mathrm{min}} > 2.2$ GeV [3]. The average number of charged tracks is 17 per hadronic $\gamma\gamma$ event, with 100 GeV deposited in the calorimeter. This study needs to be repeated for the NLC IP parameters and detector acceptance. Nonetheless, we can estimate the severity of this background by scaling the rate from the TESLA study by the square of n_γ, the

average number of photons produced by beamstrahlung, giving a factor $((1.2/1.6)^2)$, and also taking the bunch structure (190/1) into account. This leads to an event probability of 2.2 events/train with 220 GeV in the calorimeter at $\sqrt{s} = 500$ GeV. It would clearly be advantageous to be able to time-stamp the hit calorimeter cells and tracks with the bunch number that produced them and thereby limit the background affecting a physics event of interest.

Muons and synchrotron radiation. SR photons arise from the beam halo in the final doublet, as shown in Fig. 15.4. The limiting apertures of the IR layout determine the maximum angular divergence of the charged particles that can be tolerated. Particles above the maximum divergence must be removed by the accelerator's collimation system. If the VXD radius is too small, the apertures in the collimation system required to remove the beam halo will be unreasonably small and will produce wakefields that will lead to beam spot size increases and a loss of luminosity. As particles are scraped off by the collimation system, muons are produced. Depending on the level of the halo and the robustness of the detector against background muons, a magnetic muon spoiler system may be required.

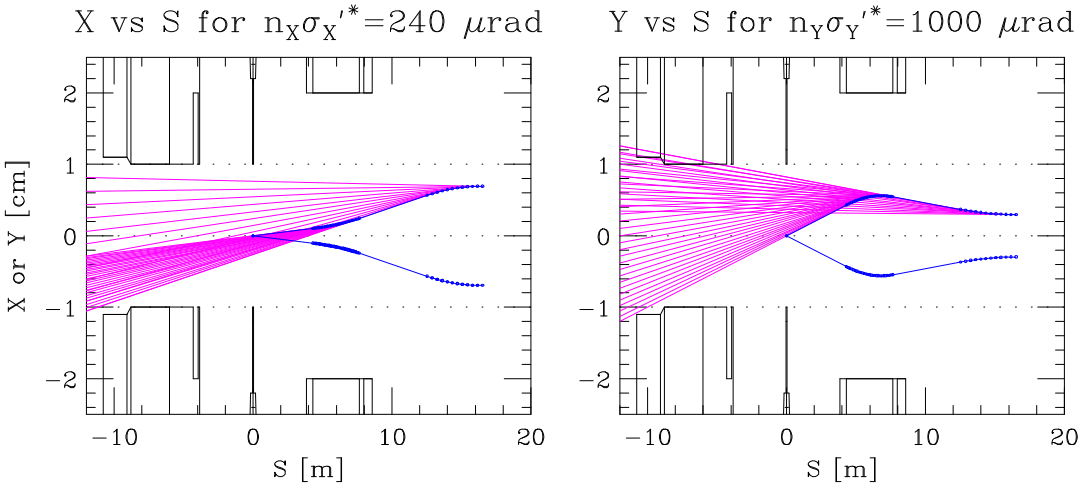

Figure 15.4: Synchrotron radiation fans from beam halo particles .

3 Subsystem considerations

3.1 Vertex detector

Recent experiments have benefited enormously from investments in excellent vertex detectors. An important lesson has been the immense value of a pixelated detector. This technology enabled SLD to match many of the physics measurements

at LEP with a much smaller data sample. The physics goals of the linear collider will also demand optimal vertex detection. The physics signals are rich in secondary vertices, and event rates are limited, demanding highly pure and efficient tagging.

Physics processes requiring vertex detection include the Higgs branching ratios, SUSY Higgs searches such as A$\rightarrow \tau^+\tau^-$, searches for staus, top studies, improved measurement of W pairs, Z' studies such as τ polarization, and Z pole physics. Some processes will involve several heavy quark decays, complicating the reconstruction, and increasing the demand for pixelated detectors. The physics will require highly efficient and pure b and c tagging, including tertiary vertex reconstruction, and charge tagging (as needed for $b/\overline{b}$ discrimination, for example). Optimal performance calls for point resolutions better than 4 μm, ladder thickness under 0.2% X_0, inner layers within 2 or 3 cm of the interaction point, coverage at least over $|\cos\theta| < 0.9$, and good central tracking linked to the vertex detector. The accelerator time structure and radiation environment will constrain the design, and must be carefully considered.

A pixel CCD vertex detector was developed at the SLC. The SLD vertex detector, VXD3 [4], comprised 307 million pixels on 96 detectors, and achieved 3.8 μm point resolution throughout this large system. With such exceptional precision, extremely pure and efficient flavor tagging at the Z-pole was possible: 60% b tagging efficiency with >98% purity, and better than 20% c tagging efficiency with 60% purity. SLD also achieved exceptional charge separation between b and $\overline{b}$. The value of the pixel detector has been clearly established, even in the relatively clean environment of the SLC, where the hit occupancy in VXD3 was about 10^{-4}. These successes motivate the choice of CCDs for the next-generation linear collider, where even better performance is foreseen.

The main weaknesses of the CCD approach to vertex detection are the slow read-out speed and the radiation sensitivity. The speed issue can be managed at the linear collider, as SLD demonstrated. The hit density is maximal at the inner radius, where one expects about 3 per mm^2 per bunch train at 1.2 cm. This rate of $\sim 10^{-3}$ per pixel is challenging, but manageable, especially when the inner layer hits are matched to tracks reconstructed outside this layer.

With regard to the radiation background, the neutrons create the major challenge. Fluences greater than 10^9/cm^2/year are expected. CCDs are expected to withstand this level of radiation. However, since the neutron backgrounds could be larger, CCDs with engineered rad-hard enhancements are being studied [5].

Despite the established performance of the CCD vertex detector, active pixels do provide interesting alternatives. They can be inherently less sensitive to radiation damage (hence the interest in using them at the LHC), but generally have been less precise, and they contain more material leading to multiple scattering. Efforts are underway to close the gap between the demonstrated CCD performance and the state of the art in active pixels. These efforts will be followed closely.

Central tracking is vital to the performance of the vertex detector. With severely

limited momentum resolution of its own, the vertex detector relies on the momentum measurement of the tracker for inward projection of tracks.

3.2 Tracking

Tracking of high-energy isolated charged particles will be important at a linear e^+e^- collider. Isolated leptons are prevalent in many new physical processes, including production of sleptons, heavy leptons, and leptoquarks, and in many interesting Standard Model processes, notably in associated hZ production where the Z decays into charged leptons. While the calorimeter may provide a good measure of electron energy (but not electric charge), excellent tracking will be needed to measure high muon energies and the charged decay products of τ's.

Reconstruction of hadron jets will also be important, both in searching for new physical processes and in understanding Standard Model channels. Compared to the high-energy leptons discussed above, charged hadrons in jets have much lower average energies, relaxing the asymptotic $\sigma(1/p_t)$ requirements. But tracking these hadrons well requires good two-track separation in both azimuth (ϕ) and polar angle (θ). Aggressive jet energy flow measurement also requires unambiguous extrapolation of tracks into the electromagnetic calorimeter, again demanding good two-track separation and also good absolute precision.

Forward-angle tracking is expected to be more important at a linear collider than has been traditionally the case for e^+e^- detectors. Some supersymmetry processes have strongly forward-peaked cross sections. Furthermore, in order to monitor beamstrahlung adequately, it is likely that precise differential luminosity measurement will be necessary, including accurate (0.1 mrad) polar angle determination of low-angle scattered electrons and positrons [6].

The central tracker cannot be considered in isolation. Its outer radius drives the overall detector size and cost. Given a desired momentum resolution the tracker's spatial resolution and sampling drive the required magnetic field. This affects the solenoid design, including the flux return volume.

For a detector with a compact silicon vertex detector and a large gas chamber for central tracking, an intermediate tracking layer can improve momentum resolution, provide timing information for bunch tagging, and serve as a trigger device for a linear collider with a long spill time.

The most important technical issue for the tracking system is designing to meet a desired resolution in $1/p_t$ of order 10^{-5} GeV^{-1}. This goal is driven by mass resolution on dileptons in Higgsstrahlung events and by end-point resolution in leptonic supersymmetry decays. There are tradeoffs among intrinsic spatial resolution, the number of sampling layers, the tracking volume size, and the magnetic field. The choices affect many other issues. For example, pattern recognition is more prone to ambiguities for a small number of sampling layers, with in-flight decays a particular problem. Matching to the vertex detector and achieving good two-track separation is more

difficult for large intrinsic spatial resolution. A large magnetic field distorts electron drift trajectories for several tracking technologies. High accelerator backgrounds may lead to space charge buildup in a time projection chamber (TPC), degrading field uniformity and hence resolution. More generally, though, high backgrounds tend to favor choosing a TPC or another device which makes 3-dimensional space point measurements (such as a silicon drift detector) over a device with 2-dimensional projective measurements (such as an axial drift chamber or silicon microstrips). On the other hand, a pixel-based vertex detector may provide adequate 'seeds' for tracks, even in the presence of large backgrounds.

Material in the tracker degrades momentum resolution for soft tracks and increases tracker occupancy from accelerator backgrounds due to Compton scattering and conversions. Because front-end electronics can be a significant source of material, readout configuration can be quite important, affecting detector segmentation and stereo-angle options. Achieving polar angle resolution comparable to the azimuthal angle resolution may be expensive and technically difficult.

As mentioned above, accelerator backgrounds can degrade track reconstruction via excessive channel occupancy. One possible way to ameliorate the effects of this background is via bunch tagging (or bunch-group tagging) of individual tracking hits, but such tagging may place strong demands on the tracker readout technology.

3.3 Calorimetry

3.3.1 Energy flow

The first question for calorimetry at the linear collider is one that not only influences the overall philosophy of this system but also has ramifications for other detector subsystems and for the overall cost: Should the calorimeter be optimized to use the 'energy flow' technique for jet reconstruction? The promise of substantial improvement in resolution using this technique is appealing. However, quantitative measures of this improvement are still being developed, and it is likely that an energy flow calorimeter will be relatively complicated and expensive because of the fine segmentation and high channel count.

Clearly, multi-jet final states will be important for LC physics. Examples from the physics program include separation of WW, ZZ, and Zh in hadronic final states, identification of Zhh, and $t\bar{t}h$ in hadronic decays, and full reconstruction of $t\bar{t}$ and WW events in studies of anomalous couplings and strongly-coupled EWSB. A further example comes at high energy from the processes $e^+e^- \to \nu\overline{\nu}WW$ and $e^+e^- \to \nu\overline{\nu}t\bar{t}$, where because of low statistics and backgrounds, one would need good jet-jet mass resolution without the benefit of a beam energy constraint. Indeed, one of the often-stated advantages of the e^+e^- environment is the possibility to reconstruct many types of final states accurately. In some instances, this is the key to the physics performance.

The energy flow (EF) technique makes use of the fact that the modest momenta of charged hadrons within jets are more precisely determined in the tracking detectors, than with a calorimeter. On the other hand, good energy resolution for photons (from π^0 decay) is achieved using any standard technique for electromagnetic calorimetry. Long-lived neutral hadrons (mostly K_L^0) are problematic using any technique, but they cannot be ignored. Therefore, a calorimeter designed to take advantage of EF must efficiently separate neutral from charged particle energy depositions. Such designs are characterized by a large tracking detector (radius R), a large central magnetic field (B), and an electromagnetic calorimeter highly segmented in 3-D. A figure of merit describing the ability to separate charged hadrons from photons within a jet is BR^2/R_m, where R_m is the Moliere radius of the electromagnetic calorimeter (EMCal). The EMCal's transverse segmentation should then be less than R_m in order to localize the photon showers accurately and distinguish them from charged particles. Similarly, the separation of the long-lived neutral hadrons from charged hadrons improves with BR^2 and a finely segmented hadron calorimeter (HCal). The reconstruction process involves pattern recognition to perform the neutral-charged separation in the calorimeter, followed by a substitution of the charged energy with the corresponding measurement from the tracker.

The advantage of EF is clear in principle. Whether the advantage is borne out with realistic simulation is not yet resolved, as the tools required to do justice to the technique are still under development. With their silicon/tungsten EMCal, the TESLA group currently finds [7] $40\%/\sqrt{E}$ for jet energy resolution (where E is the jet energy in GeV). They expect this to improve to $30\%/\sqrt{E}$ with progress in pattern recognition. Assuming that such good performance is indeed achievable with EF, it is useful to identify how this would improve the physics outlook, and at what cost.

3.3.2 Resolution, segmentation, and other requirements

There is no compelling argument from LC physics that demands outstanding photon energy resolution, resulting for example from an EMCal using high-Z crystals. Furthermore, such an optimization would not be consistent with the high degree of segmentation required for excellent jet reconstruction. Instead, the requirements for calorimetry from LC physics are jet energy and spatial resolution, and multi-jet invariant mass resolution. The required jet energy resolution depends, of course, on specific physics goals. A recent study [8] indicates that a resolution of $40\%/\sqrt{E}$ is necessary to measure the Higgs self-coupling using Zhh final states. One benchmark for jet-jet mass resolution is the separation of W and Z hadronic decays in WW, ZZ, and Zh events. Both of these requirements may be achievable using energy flow reconstruction.

Segmentation is a critical parameter, since an EF design requires efficient separation of charged hadrons and their showers from energy depositions due to neutrals.

The typical charged-neutral separation, Δx, is dervied from the particle density in jets after they pass through the tracking detectors. This depends upon the physics process and $\sqrt{s}$, as well as the tracker radius and the detector magnetic field. Studies show that the minimum Δx is typically 1–4 cm in the EMCal and about 5–10 cm in the HCal. The EMCal should be very dense, with Moliere radius of a few cm or less, and should have transverse segmentation that is smaller still, in order to localize the photon showers accurately. Fine longitudinal segmentation, with each layer read out, is also essential in order to track the charged particles through the EMCal and to allow charged-neutral separation in 3-D. This will also benefit the energy resolution for photons and electrons. There is no reason to organize the layers in towers, and, in fact, this probably should be avoided. The fine transverse segmentation provides excellent electron identification and photon direction reconstruction. The latter is also useful for measuring photons which result from a secondary vertex. This is relevant, for example, in gauge-mediated SUSY, which can lead to secondary vertices with a photon as the only visible decay particle.

For EF in the HCal, it is desirable to track MIPs throughout. One would need to identify shower positions with a resolution of a few cm. Because of the relatively diffuse distribution of deposited energy for hadron-initiated showers, the solution for charged/neutral identification is not as obvious as for the EMCal case, and different ideas are under consideration. In any scheme, one requires a high degree of segmentation. This might be implemented, for example, using scintillator tiles roughly 5–10 cm on a side. Another idea is to push to finer segmentation, using, for example resistive plate chambers (RPCs), but without providing pulse height in the readout. Such a 'digital' hadron calorimeter is one of the options being considered for TESLA. This provides increased resolution for pattern recognition, but perhaps with poorer neutral hadron energy resolution.

As with this segmentation issue, many of the other properties of the HCal in an EF calorimeter remain uncertain. One example is the necessary total calorimeter depth in interaction lengths. Another is the placement of the solenoid coil. Since the fields are typically large, and the coils are at large radius, their thickness is not negligible. Qualitatively, for good performance one would prefer to have the coil outside the HCal. But the tradeoffs are not yet well understood quantitatively.

The EF jet resolution is dominated by the tracker momentum resolution, the calorimeter pattern recognition efficiency, and by the purity of charged/neutral identification. Hence, single-particle resolutions are less important. However, the current EF designs yield energy resolution $A/\sqrt{E}$ in the range $A = 12$–20% for photons, and in the range $A = 40$–50% for single hadrons.

For a detector not designed to use energy flow, there are, of course, many traditional choices available. Assuming that jets are to be reconstructed using the calorimeter only, one might choose a compensating, sampling calorimeter with a tower geometry. One or more layers of detector with finer segmentation may be required

at the front of the EMCal, or at shower maximum, to aid with electron and photon identification. Such a calorimeter would certainly be cheaper than an EF device at a similar radius. At low $\sqrt{s}$, especially at the Z, this may suffice.

One also needs to consider Bhabha scattering in the calorimeter design. First, the final state $e^{\pm}$ at $\sqrt{s}/2$ determines the upper end of the dynamic range of the EMCal readout. For example, for a dense EMCal, the ratio of deposited energy for Bhabha electrons to MIPs can be 10^3 to 10^4, depending on segmentation. Secondly, the Bhabhas are used for luminosity measurements of two types. First, the Bhabha rate can be used to measure the absolute luminosity. Since this rate at intermediate to large angles (endcap and barrel) will be large compared to (known) physics processes, it would not be necessary to rely on a small-angle luminosity monitor (LUM), although a LUM would still be useful for crosschecks and operations. Running at the Z is an exceptional case where a precise LUM would be required. The Bhabhas also provide probably the best measurement of the luminosity spectrum, $d\mathcal{L}/dE$, because the Bhabha acolinearity is closely related to the beam energy loss. This is ideally measured at intermediate angles, and the EMCal endcap will need to be able to aid the tracker with this measurement.

In addition to Bhabha scattering, two other types of measurement have been discussed for the small-angle region. One is a measurement of the flux of pairs produced in the collision beam-beam interactions. This would provide immediate feedback to operators of a quantity closely related to the instantaneous luminosity. The other is small-angle tagging of the forward-scattered electron or positron resulting from a two-photon interaction. This is useful both in the study of the two-photon process itself and in reducing background in the study of processes such as slepton pair production which resemble two-photon reactions. Such a device would need to tag a single high-energy electron within the angular region flooded by low-energy pairs from the beam-beam interaction.

Finally, the small-angle elements of any calorimeter design must reflect the requirement to limit the detector contribution to the missing transverse momentum resolution. This contribution is roughly $E_b\theta_{\rm min}$, where E_b is the beam energy. Given the limited angular coverage of the central tracking systems, one should consider carefully what type of calorimetry should be used near $\theta_{\rm min}$.

3.3.3 Technology options

For the dense, finely segmented electromagnetic calorimeter required for energy flow, layers composed of a tungsten radiator with silicon detectors (Si/W) are a natural choice. The Moliere radius of tungsten is small (9 mm), and the silicon is thin and easily segmented transversely. Si/W EMCal's are currently incorporated in two LC detector designs, the TESLA detector and the NLC SD detector described in Section 4.2. This option has one outstanding drawback, the cost of the silicon detectors.

Both TESLA and SD assume that a cost of roughly \$3/cm^2 can be achieved in the future with a very large order. This is about a factor two cheaper than current costs. There are a number of cost and performance optimization possibilities. For example, one would probably not need to sample the EMCal uniformly in depth, reducing the sampling frequency after about 12 X_0. One could also improve the photon energy resolution by sampling with thicker silicon, at some small loss of Moliere radius.

Perhaps it is possible to design a competitive energy flow electromagnetic calorimeter at lower cost using an alternative to silicon, for example, scintillator tiles. The transverse segmentation is limited using present techniques by the inability to couple sufficient light to a readout fiber. Perhaps this can be improved. However, given the larger cells, sufficiently large B and R may compensate for the segmentation disadvantage. This is the rationale for the NLC L design described in Section 4.1. Another alternative being considered for TESLA is a Shashlik EMCal. Beam test results [9], using fibers of two lifetimes in order to achieve some longitudinal segmentation, have been impressive, but it is unclear whether the segmentation is sufficient for EF.

The hadron calorimeter for an EF detector is not as highly constrained as the EMCal. Here, scintillator tiles can be of size similar to present applications, say 8–10 cm on a side, with coupling to an optical fiber. Such a scheme is under consideration for the TESLA and NLC L and P designs. (The last of these is described in Section 4.3.) Other possibilities include the 'digital' option mentioned above, which might use, for example, double-gap RPC readout layers or extruded scintillator. The spatial resolution per layer might be about 1 cm.

If it were possible to relax the need for precise jet reconstruction, then one might forego EF, and save some money with a more traditional calorimeter. For example, the NLC P design uses modestly segmented towers built up from Pb/scintillator layers. This might also be implemented using liquid argon.

3.4 Muon detection

The main purpose of the LC muon system is to identify muons and provide a software muon trigger. A secondary purpose is to use the muon detector as backup calorimetry for those particles that penetrate beyond the normal hadron calorimeter. The signature for muons is their penetration through the calorimetry and the instrumented iron flux-return for the solenoid field.

The momentum of muons is determined from the central and forward tracking systems. This requires the association of tracks found in the instrumented flux-return with hits/tracks in the central and forward tracking detectors. Two conditions permit this: a reasonable density of hits in the inner layers of the tracking detectors and limited confusion from multiple scattering due to the electromagnetic and hadronic calorimeters between the inner tracking detectors and the front face of the muon detectors. These conditions are satisfied, since the maximum density of tracks, at a radius of 3 m, is about 1/cm^2 [10] and the r–ϕ rms multiple scattering of a 10 GeV/c

muon is approximately 2 cm. The number of radiation lengths X_0 of material in front of the muon system for the three candidate detectors L, SD and P are $200, 88$ and 125, respectively.

Muons are identified by their ionization in tracking chamber panels [10] or scintillator strips [11] in 2 cm gaps between 5 or 10 cm thick Fe plates that make up the barrel and end sections of the Fe return yoke for the central solenoidal magnetic field. RPCs are taken as the example technology. These planar devices can be built with appropriate perimeter shapes, and they do not contain wires that could break. Tracking hits from the avalanche produced in the RPC gaps are read out with strip electrodes that run in the ϕ and z directions. The spatial resolution of these strips is 1 cm per detector plane.

For the case of the L detector, it can be seen in Fig. 15.5 that the number of hits as a function of momentum for W pair production, plateaus at about 5 GeV with 25 instrumented gaps. The plot shows that in the 3 T field there will be very good efficiency if 15 or more hits are required in the muon tracking algorithm.

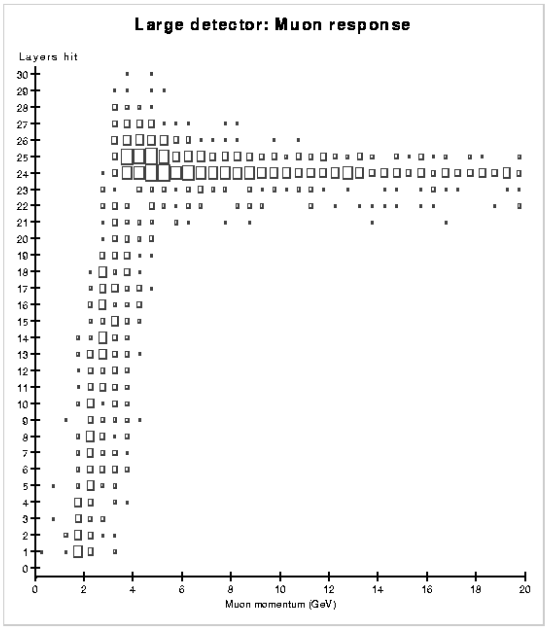

Figure 15.5: Hits in the muon system as a function of momentum for the L detector. The pllot shows 10000 $e^+e^- \to W^+W^-$ events in which one W decays to a muon.

The Fe plate and strip readout for the muon system can be used as additional

coarse hadron calorimetry, since the number of interaction lengths λ for the L, SD and P options are, respectively, 6.6, 6.1 and 3.9. The muon Fe adds 7, 6, and 6 λ that can be used in the determination of residual hadronic energy with a resolution that will be about $1/\sqrt{E}$.

3.5 Solenoid

The detector is assumed to be a classical solenoidal design. The field in the tracking region ranges from 3 to 5 T for the various designs. The solenoid is assumed to be of the CMS type, based on a relatively thick, multi-layer superconducting coil. The radial thickness of the complete assembly is about 85 cm. The CMS vacuum shell has a total thickness of 12 cm, and a cold mass thickness of 31 cm (aluminum). It is likely that the cold mass thickness will scale roughly as B^2R. Then, the coil of the SD detector would be about 35% thicker.

The iron serves as the flux return, the absorber for the muon tracker, and the support structure for the detector. The (perhaps debatable) requirement of returning most of the flux drives the scale of the detector. At this stage of preliminary design, it is assumed that the steel is in laminations of 5 cm with 1.5 cm gaps.

The door structure very likely runs along the beamline past L*, the position of the downstream face of the last machine quadrupole. Thus it is essentially certain that the Final Doublet (FD) is inside the detector, and quite possibly within the Hadronic Calorimeter. For this reason, the FD cannot be mounted on a massive column going directly to bedrock.

3.6 Particle ID

The physics topics of the linear collider do not demand hadron ID in a direct way, though the information may prove valuable for some analyses. Pions, kaons and protons are produced in the ratio of about 8:1:0.6 in high-energy e^+e^- colliders. The momentum spectrum of kaons in $q\overline{q}$ events at $\sqrt{s}$ =500 GeV extends up to 150-200 GeV/c, posing a possibly unsurmountable ID measurement challenge. However, the average kaon momentum is only 10–17 GeV/c, and more than half of all kaons have momenta below 7 GeV/c. In t-quark and multi-b jet Higgs events, the multiplicity is higher, and so kaons have a slightly lower mean momentum.

The measurement of particle species distributions provides information on QCD processes and permits model tests, but the most important use of hadron ID may be to assist the application of other techniques, such as B tagging. As an example, two studies [12,13] have discussed the use of net kaon charge to tag the flavor of neutral B mesons produced in $q\overline{q}$ events. They find that with perfect knowledge of decay product identities in vertex-tagged neutral B mesons, roughly a quarter are correctly tagged by the net charge of kaons. The efficiency is much lower if all undiscriminated hadrons are used. It is a detailed, and so far unanswered, question whether the use of

hadron ID with realistic detector efficiencies can be an important tool to unscramble complex events that contain multiple b- or c-quark jets.

The geometric and, ultimately, the cost constraints limit the choice of technology for a hadron ID system of a linear collider detector. Ideally, it should take up no space and introduce no additional mass in front of the calorimeter. Traditional ionization measurement (dE/dx) in gas-based tracking chambers comes close to meeting these criteria.

The Time Projection Chamber (TPC) technology that appears in the TESLA and L tracker designs may be an optimal choice for combined tracking and ionization measurements for particle ID. The energy resolution that has been achieved with existing non-pressurized TPCs (*e.g.*, ALEPH at LEP) is 4.5%, which would yield π/K separation of better than 2σ for $p < 0.8$ GeV/c and 2-3 σ for $1.7 < p < 65$ GeV/c. One can improve the capability of a TPC by using pressurized gas to achieve 2.5% resolution, as demonstrated by the TPC at PEP. According to a recent model [14], this could provide 4σ π/K separation in the range $1.75 < p < 30$ GeV/c.

In practice, experiments that desire a high degree of species separation have supplemented ionization measurements with specialized devices such as time-of-flight, threshold Cerenkov or ring-imaging Cerenkov devices. The major drawback of a specialized hadron ID subsystem is its collateral impact on the tracking and calorimetry. All supplementary techniques take up radial space between the tracker and calorimeter, which means either shorter tracking volume or increased calorimeter radius with consequent cost and performance implications. Without a clearly defined need for the capability, it is difficult to justify a significant impact on the rest of the detector. For example, in the B^0 tagging study, even though the best performance was provided by an SLD-style CRID or a high-pressure TPC, relatively inexpensive improvements to an ALEPH-type TPC could achieve a sensitivity within a factor of two of these more complicated options but with little impact on the calorimetry.

In summary, at this stage there is no compelling argument to include a specialized hadron ID system in the high energy detector design, though in the process of optimizing the design this assumption may be reexamined.

3.7 Electronics and data acquisition

The NLC beam consists of 190 bunches spaced 1.4 ns apart, in trains that repeat at 120 Hz. There are variations with a doubled bunch spacing and an increased train frequency of 180 Hz, but these variations do not affect the basic theme. For most of the detector subsystems it will neither be possible, nor particularly desirable, to resolve bunches in a train. The train repetition rate of 120 Hz is a low frequency compared with Level 1 or Level 2 trigger rates at many other machines. There is no need for a hardware trigger, and (zero-suppressed, calibration-corrected) data can flow from the detector at this rate. A traditional Level 3 Trigger (software on a small set of processors) can select events for storage.

The time horizon for a detector is roughly 8 to 10 years away, which is at least 5 Moore's Law generations. To be sure, Moore's Law refers to computing power per dollar, but there are clearly related trends in most areas of silicon technology. At this time it seems most appropriate to sketch plausible architectures to help generate cost estimates, and to avoid detailed designs.

Perhaps the clearest distinction that should be made is the role of interconnections that are not on silicon. Rather inexpensive systems have been developed for large CCD detectors. The costs strongly reflect the number of output nodes that must be serviced, and correspond only weakly to the number of pixels being transmitted through that node. In addition, because of the train spacing, there is no penalty to serial multiplexing of the data from very large numbers of pixels. This is in contrast to the LHC, where there are many interactions associated with each beam crossing, which occurs every 25 ns. This is not to say there are no limits to the serial multiplexing. The readout of the SLD Vertex Detector crossed about 8 beam crossings at SLC, and it would be desirable to avoid this at the next-generation linear collider.

Consequently, we have developed the concept of clusters rather than channels. A cluster is a set of detector elements that can conveniently be processed and serialized into a single data stream, presumably an optical fiber. In the CCD example, each node might correspond to a cluster, although it might even be possible to handle multiple nodes in a single cluster. For the CCD case, we think of an ASIC located millimeters from the CCD and bonded to the CCD. This ASIC might handle the clock generation and the gate drives as well as the amplification and digitization of the CCD data. For silicon strip detectors, we foresee a single chip servicing a cluster of strips, presumably a complete detector a few cm wide. For a calorimeter utilizing scintillator and Hybrid Photo Diodes or Multi-Anode Phototubes, a cluster would correspond to all the outputs from each such device. In all cases, we avoid, as much as possible, all low-level cables and interconnects. The cluster reflects the mechanical nature of the detector. Some cases are less obvious. For a tungsten-silicon calorimeter, a cluster might correspond to a large area board carrying many close packed wafers of silicon diodes. It may cover perhaps a square meter or so. Variations on this concept would cover readout sectors of the TPC and the muon tracking detectors.

Thus the detector proper carries all the front end processing, and a relatively modest set of fibers carries data off the detector. We envision the fibers delivering the data to processors, perhaps based on VME, although there are hints that crate systems based on optical serial backplanes may arrive in time. These processor arrays would complete the signal processing, build the events, and pass those events to the system responsible for the Level 3 decision.

4 Detectors

Three detector models are now being studied as potential detectors for the NLC. These include two options for the high-energy IR, called L and SD, and one for the lower-energy, second IR, called P. Here we describe each of these detectors, and present some of their performance curves.

4.1 L detector for the high-energy IR

The L detector design is driven by the desire to provide a large tracking volume, to optimize tracking precision. This leads to a large-radius calorimeter and limits the magnetic field strength to about 3 Tesla.

The L detector is illustrated in Fig. 15.6. Table 15.1 presents the dimensions of the L detector, along with those for the SD and P detectors, described below.

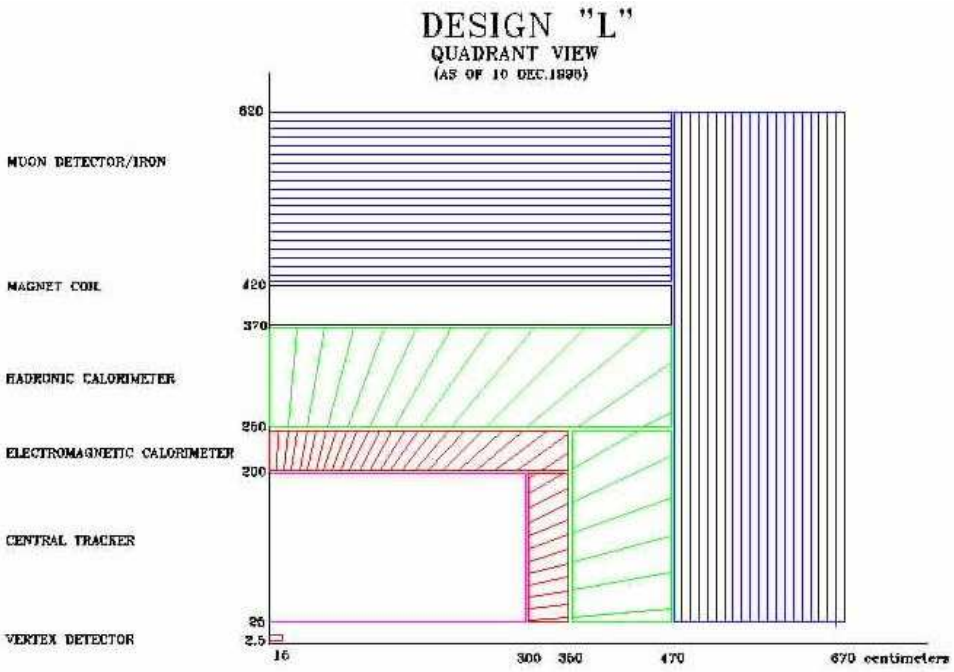

Figure 15.6: Quadrant view of the L detector.

The vertex detector is a five-barrel CCD vertex detector, based on the technology developed for SLD. The beam pipe radius of 1 cm allows the inner barrel of the detector to reside 1.2 cm from the IP. The inner barrel extends over 5 cm longitudinally. The other barrels have radii of 2.4 cm, 3.6 cm, 4.8 cm, and 6.0 cm, and they each extend 25 cm longitudinally. The barrel thicknesses are 0.12% X_0 and the precision

Component	L Detector				SD Detector				P Detector			
	R(cm)		Z(cm)		R(cm)		Z(cm)		R(cm)		Z(cm)	
	Min	Max	Min	Max	Min	Max	Min	Max	Min	Max	Min	Max
Vertex Det.	1.0	10	0	15	1.0	10	0	15	1.0	10	0	15
C.Track.	25	200	0	300	20	125	0	125	25	150	0	200
ECal												
Barrel	200	250	0	350	127	142	0	187	150	185	0	235
EndCap	25	200	300	350	20	125	172	187	25	150	205	240
HCal												
Barrel	250	370	0	470	143	245	0	289	215	295	0	320
EndCap	25	250	350	470	20	125	172	187	25	175	240	320
Magnet	370	420	0	470	248	308	0	289	185	215	0	235
Iron/Muon												
Barrel	420	620	0	470	311	604	0	290	295	425	0	320
EndCap	25	620	470	670	20	604	290	583	25	425	320	450

Table 15.1: Dimensions of the L, SD, and P Linear Collider Detectors.

is assumed to be 5 μm. (This is taken as a conservative assumption, since SLD has achieved 3.8 μm.) The entire system comprises 670,000,000 pixels of $20 \times 20 \times 20$ μm^3.

Figure 15.7 illustrates this system. The detector operates in an ambient temperature of 190°K, created by boil-off nitrogen. It is enclosed within a low mass foam cryostat. The same five-barrel CCD design has been assumed for the SD and P detectors below.

The performance of the vertex detector is illustrated in Figs. 15.8 and 15.9, where it is also compared to the SD and P Detector performance. The impact parameter resolution shown in Fig. 15.8 is shown to surpass the performance of SLD's VXD3. The bottom and charm tagging performance, shown in Fig. 15.9, is also seen to be exceptional.

The L detector central and forward trackers consist of a large-volume TPC, an intermediate silicon tracking layer (silicon drift detector or double-sided silicon microstrips), and five layers of double-sided, silicon microstrip disks in the forward regions. An additional scintillating-fiber intermediate tracker option has also been proposed to provide precise bunch timing. Figure 15.10 shows a sketch of the L detector tracking system.

A large-volume TPC with three-dimensional space point measurements along charged particle trajectories provides excellent pattern recognition (including recognition of long-lived particles that decay in the tracking volume) and good particle identification via dE/dx measurements. The baseline L detector TPC [15] has 144 tracking layers enclosed in a cylindrical volume of inner and outer radii = 50 and 200 cm, respectively, and of half-length 290 cm. The assumed resolutions on each hit are 150 μm in r–ϕ and 0.5 mm in r–z. A GEM-based readout has the potential to reduce

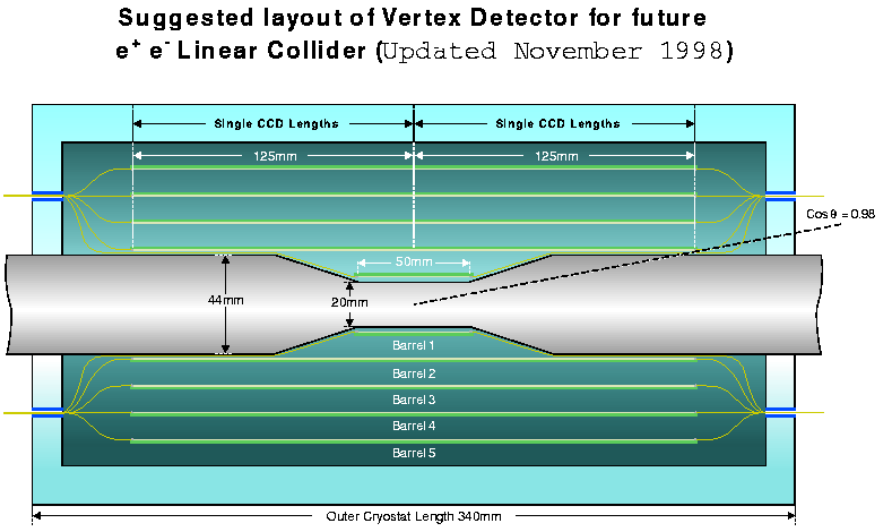

Figure 15.7: The five-barrel CCD vertex detector proposed for the linear collider.

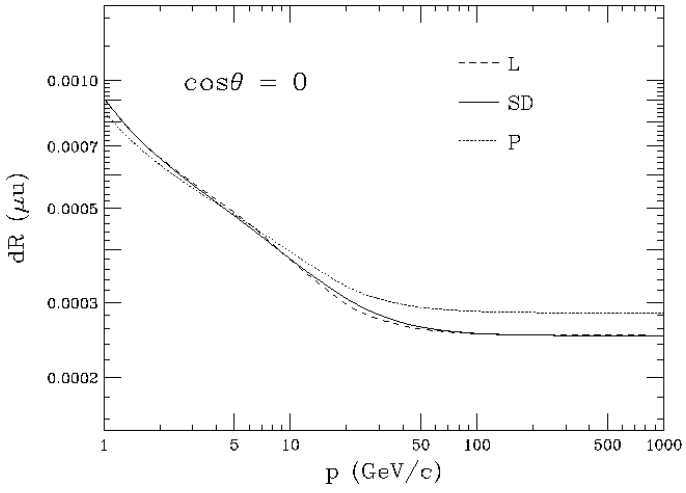

Figure 15.8: Impact parameter resolution versus momentum for the vertex detector shown in Fig. 15.7.

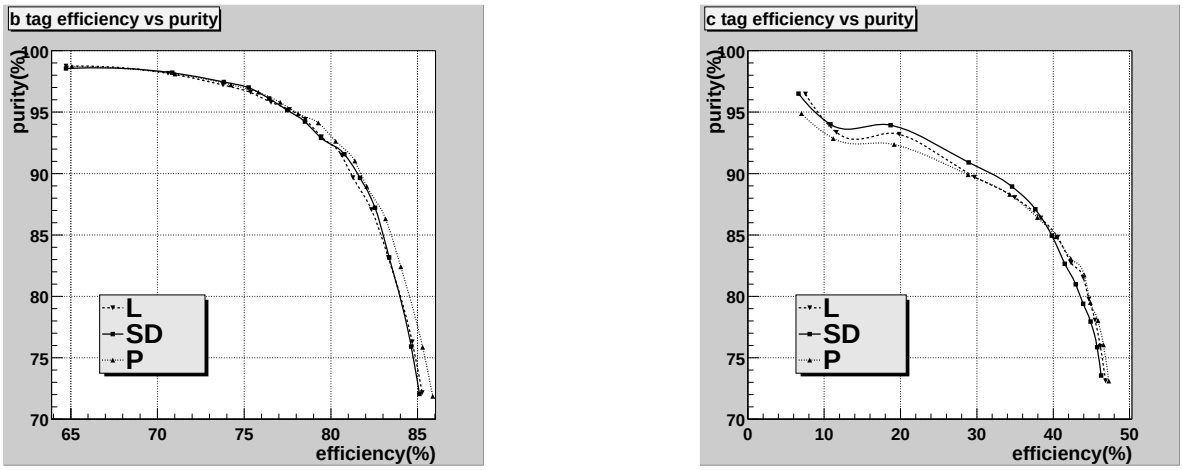

Figure 15.9: Vertex-tagging purity versus efficiency for b (left) and c (right), evaluated for decays of the Z^0 at $E_{\mathrm{CM}} = 91.26$ GeV.

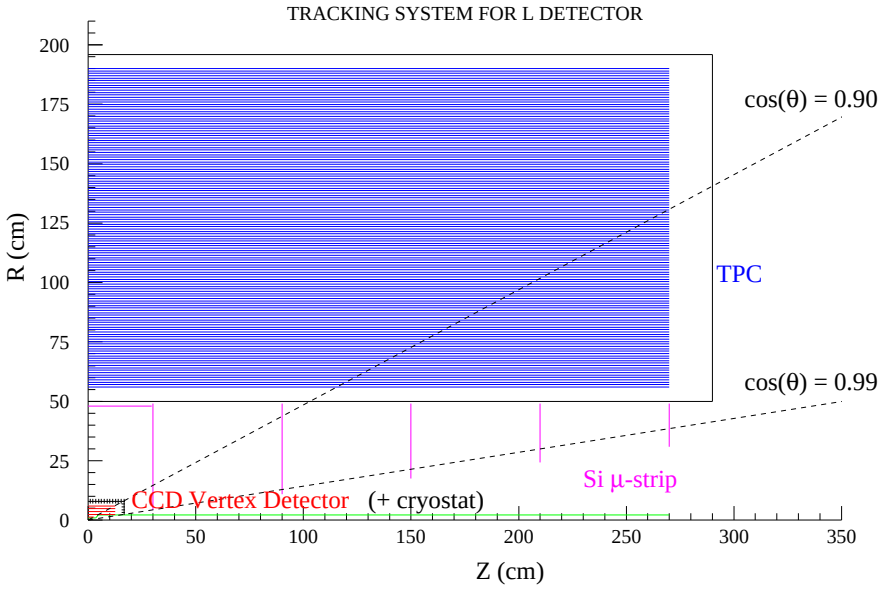

Figure 15.10: Sketch of L detector tracking system.

the r–ϕ resolution to 100 μm. The small transverse diffusion for TPC operation in the 3 T magnetic field requires very narrow cathode pads and large total channel counts. Longer pads or the use of induced signal on adjacent pads may be considered to reduce the channel count. Good track timing resolution is obtained by requiring individual charged tracks to point back to a reconstructed vertex in the r–z plane. This timing resolution helps in reducing accelerator backgrounds.

The TPC in the STAR detector at RHIC has over 138,000 electronics channels and includes several design innovations. To reduce the required cable plant, low-noise low-power front end electronics are mounted on the TPC end planes. The analog signals are amplified, sampled and digitized before being sent to the DAQ system over fiber optics. A similar scheme is assumed here, with 20-MHz sampling, a 200-ns peaking time and 9-bit digitization.

The TPC analog front end electronics would consist of a high-bandwidth preamplifier and shaper amplifier (8-16 channels/ASIC chip), providing a 200 nsec peaking time pulse to the analog sampling and digitization section. The analog signals from the preamplifier and shaper amplifier would be sampled and stored with a high-frequency 20-MHz clock as they come in, and then digitized on a longer (10 μsec) time scale as new samples are being taken. The recognition of charge cluster signals on a central cathode-pad channel triggers a switched capacitor array (SCA) to sample the channel and its nearest neighbors.

Gas mixtures of argon with methane and carbon dioxide are being considered, with Ar(90%):CH_4(5%):CO_2(5%) being quite attractive in balancing safety concerns, neutron-background quenching, and drift velocity. Positive ions feeding back from endplane gas amplification can be mitigated by the installation of a gating grid.

A silicon intermediate tracking detector just inside the TPC inner radius provides nearly a factor of two improvement in momentum resolution for high-p_t tracks and offers a pattern recognition bridge between the TPC and the vertex detector. Two silicon options are under consideration: a silicon drift detector and a double-sided silicon microstrip layer. In each case the layer would have a half-length of 29.5 cm and an average radius of 48 cm. The estimated space-point resolutions in r–ϕ and r–z are 7 μm and 10 μm, respectively, for the silicon drift detector option, with both at 7μm for the double-sided microstrip option.

An additional or alternative intermediate tracker constructed from scintillating fibers offers high-precision timing to allow the matching of tracks to individual beam bunches. The current NLC accelerator design provides beams composed of trains of bunches with bunch spacings of 1.4 ns. Large rates of two-photon interactions are expected both from interactions of virtual photons and from real photons created by beamstrahlung. The overlap of the two-photon events with e^+e^- annihilation events results in additional 'mini-jets', which can be a problem if tracks created in different bunch crossings are not separated. A scintillating-fiber intermediate tracker, coupled by clear fiber to visible light photon counters and read out by the SVXIIe chip [16] can achieve time resolutions on the order of 1 ns to associate tracks with individual bunches, as well as to complement time measurements in the TPC. Appropriate Si:As devices manufactured by Boeing [17] have a fast response time of less than 100 ps. One possible system consists of two axial layers and two 3°-stereo layers with a half-length of 29.5 cm at an average radius of 48 cm, supported by a carbon fiber cylinder. Scintillating fibers of diameter 800 μm would provide individual measurements to

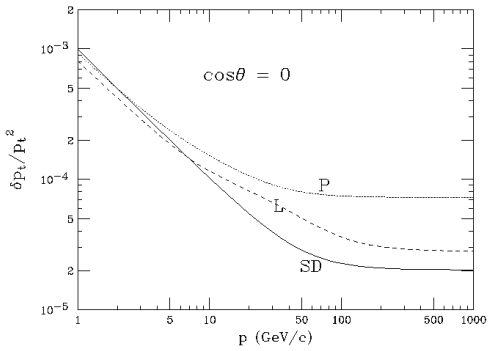

Figure 15.11: Expected fractional momentum resolution *vs.* momentum for the L, SD, and P central trackers for tracks transverse to the beam direction.

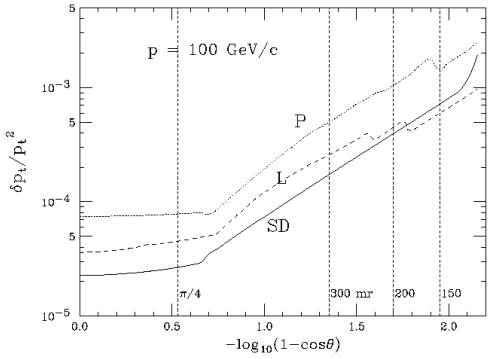

Figure 15.12: Expected fractional momentum resolution *vs.* $\cos\theta$ for the L, SD, and P central trackers for 100 GeV tracks.

230 μm and a combined point measurement with a precision of ~ 100 μm, resulting in a system with 15,000 channels.

As currently envisioned, the five layers of the L detector forward disk system are double-sided silicon microstrips, at distances of 30 cm to 270 cm from the interaction point, with fixed outer radii at 48 cm. Each side provides counterposing $\pm$ 20 mrad r–ϕ stereo information, with a point resolution of 7 μm. For high-momentum tracks at $\theta = 300$ mrad ($|\cos\theta| = 0.955$), this small-angle stereo geometry provides a resolution in θ of about ± 300 μrad. If large-angle (90°) stereo were used instead, the θ resolution would improve to about ± 100 μrad. Although the layout of silicon strip detectors is more naturally suited to small-angle stereo, the demands placed on the θ resolution by the determination of the differential luminosity spectrum may force the consideration of large-angle stereo.

The performance of the L detector tracking system, including the CCD vertex detector, is summarized in Fig. 15.11, which shows fractional momentum resolution vs. momentum for tracks transverse to the beam direction ($\cos\theta$=0). Figure 15.12 shows the fractional momentum resolution *vs.* $\cos\theta$ for tracks of momentum 100 GeV. In the limit of high-momentum tracks, the L tracking resolution in $1/p_t$ is 3×10^{-5} GeV^{-1}. Figure 15.13 shows the expected distribution in recoil mass from dimuons in the Higgsstrahlung process $e^+e^- \to hZ \to X\mu^+\mu^-$ at $\sqrt{s} = 350$ GeV for the nominal L detector baseline and for several globally rescaled resolutions in $1/p_t$.

The electromagnetic calorimeter of the L Detector is a lead-scintillator laminate with 4 mm lead followed by 1 mm scintillator for 40 layers. This results in 28.6 radiation lengths with a 2.1 cm Moliere radius. One layer of 1 cm^2 silicon pads is foreseen near shower maximum. The transverse segmentation of the scintillator is 5.2 cm $\times$ 5.2 cm. The barrel of the electromagnetic calorimeter has an inner radius

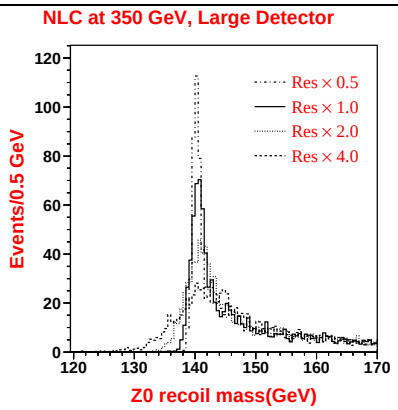

Figure 15.13: Expected recoil mass distribution in recoil mass from dimuons in the Higgsstrahlung process $e^+e^- \to hZ \to X\mu^+\mu^-$ at $E_{cm} = 350$ GeV for the nominal L detector baseline and for several globally rescaled resolutions in $1/p_t$.

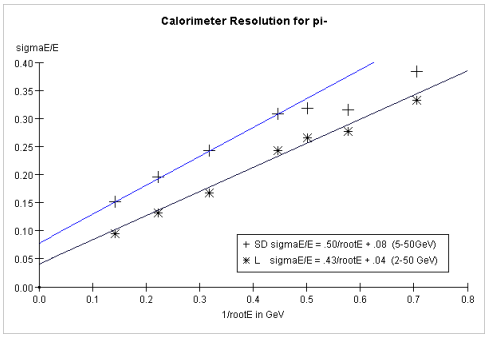

Figure 15.14: Expected π^- energy resolution in the L ($\sigma_E/E = 0.43/\sqrt{E}+0.04$) and SD ($\sigma_E/E = 0.50/\sqrt{E}+0.08$) Detectors.

of 200 cm. The electromagnetic energy resolution is expected to be $17\%/\sqrt{E}$.

The hadronic calorimeter is 120 layers of 8 mm lead layers with 2 mm scintillator sampling. The entire calorimeter comprises 6.6 interaction lengths. The transverse segmentation of the scintillator in the hadronic calorimeter is 19 cm × 19 cm. Figure 15.14 presents the expected π^- energy resolution.

The hope is that the large BR^2 of the L design will allow jet reconstruction using energy flow at a more modest cost than Si/W, overcoming the limited transverse segmentation possible with scintillator and the larger Moliere radius of lead. But, since the transverse segmentation of the EMCal is much larger than the Moliere radius, it is not clear whether energy flow can be effectively carried out for L. This is in contrast to the SD case, where the fine segmentation allows one to have some confidence that an efficient EF reconstruction can be carried out. This is clearly an area where additional work with full shower simulations is required.

Since shower reconstruction for an EF algorithm for the American detectors is still in its infancy, one can in the meantime use parameterizations of calorimeter performance using a fast simulation. One would expect that the performance from full reconstructions will eventually approach that of the fast simulation. Therefore, for the following performance plots we apply the energy flow technique, but assume a perfect charged-neutral separation in the calorimeters. The appropriate charged track resolutions and EMCal resolutions are then applied. This assumption is not unreasonable for SD, but for L it is probably too idealized. In any case, our method should indicate the asymptotic limit of performance.

To examine jet energy resolution, we used $e^+e^- \to q\overline{q}$ events without ISR or beamstrahlung, and demanded that exactly two jets be reconstructed. Hence, $E_{\rm jet} = \sqrt{s}/2 = E_{\rm beam}$. An example distribution of the reconstructed jet energy, for $\sqrt{s} = 100$ GeV is given in Fig. 15.15. Only events with $|\cos\theta_{\rm thrust}| < 0.8$ are included. The tail of the distribution is due to QCD and jet-finding effects, whereas the resolution we are interested in here is given by the Gaussian distribution near $E_{\rm beam}$, and we take the σ of this fit as the resolution. Figure 15.16 gives the resolution (the asymptotic limit of performance without accounting for non-Gaussian tails, as described above) as a function of $E_{\rm jet}$. A fit to these data gives

$$\frac{\sigma_{E_{\rm jet}}}{E_{\rm jet}} = \frac{0.18}{\sqrt{E_{\rm jet}}} \ . \tag{15.1}$$

One should not expect to actually achieve this idealized resolution with the L calorimeter.

Another important and general measurement of performance is the jet-jet mass resolution. To examine this, we examine the process $e^+e^- \to ZZ \to$ hadrons. Exactly four final-state jets were required. To get a distribution with little background, we require that one 2-jet combination have mass near M_Z, then plot the mass of the other jet pair, M_{jj}. An example M_{jj} distribution is given in Fig. 15.17 for $\sqrt{s} = 350$ GeV. Again, we fit a Gaussian to the distribution near $E_Z = E_{\rm beam}$ to extract a measure of the M_{jj} resolution. This resolution, σ_{Mjj}/M_{jj}, is plotted vs. $E_Z = \sqrt{s}/2 \approx E_{jj}$ in Fig. 15.18. A fit to the data of the form $(A/\sqrt{E_Z}) \oplus B$ gives

$$\frac{\sigma_{M_{jj}}}{M_{jj}} = \frac{0.64}{\sqrt{E_Z}} \ , \tag{15.2}$$

with negligible constant term. To the extent that the dijets from a Z are perfectly identified and that no color connection or jet merging effects occur, the sampling term constant here should approach that for the single jet energy resolution given in (15.1). The degradation of dijet mass resolution from this ideal limit requires more study.

The 3 T solenoidal coil is located outside the hadronic calorimeter to optimize calorimeter performance. The inner radius of the solenoidal coil is 370 cm.

The muon system consists of 24 layers of 5 cm iron plates, with 3 cm gaps for RPC detectors. Axial strips of 3 cm pitch measure the ϕ coordinate to 1 cm precision in all 24 gaps, and every sixth gap provides azimuthal strips for a measurement of the z coordinate to 1 cm precision. The barrel muon system begins at a radius of 420 cm. Figure 15.5 illustrates the expected performance for the L detector.

4.2 SD detector for the high energy IR

The strategy of the 'Silicon Detector' (SD) is based on the assumption that energy flow calorimetry will be important. While this has not yet been demonstrated in

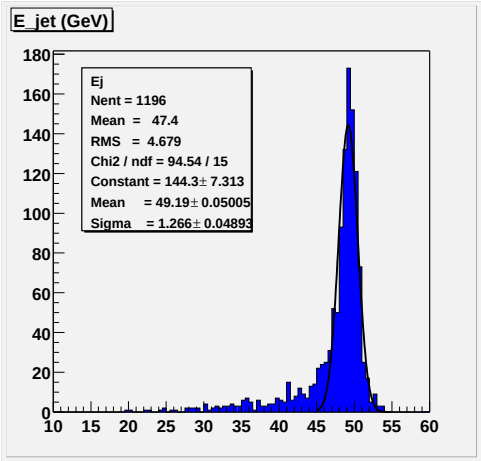

Figure 15.15: Reconstructed jet energy with the L detector for 50 GeV beam energy.

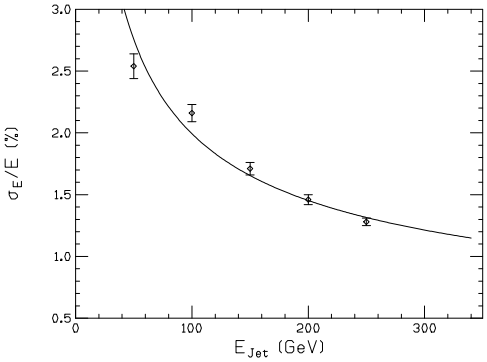

Figure 15.16: Jet energy resolution (in %) vs. jet energy for the L detector. The curve is the fit described in the text.

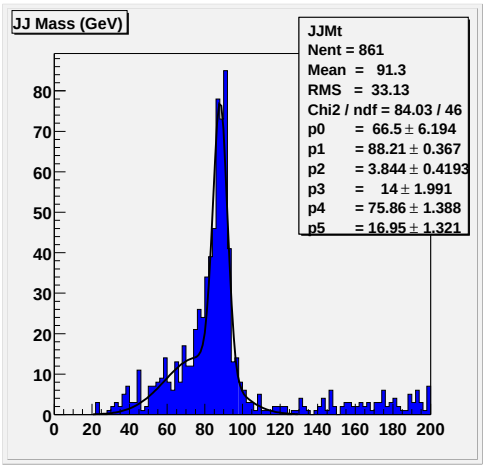

Figure 15.17: Reconstructed jet-jet mass for Z candidates in $e^+e^- \to ZZ \to$ hadrons at 350 GeV for the L detector.

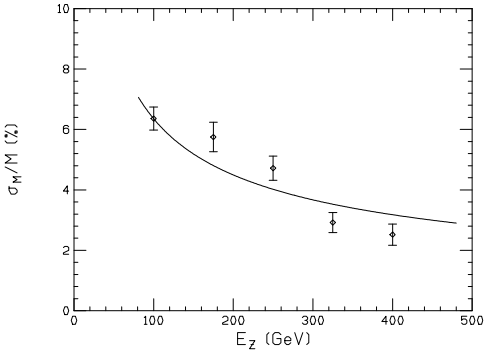

Figure 15.18: Jet-jet mass resolution (in %) for $Z \to 2$ jets vs. Z energy for the L detector in $e^+e^- \to ZZ \to$ hadrons events. The curve is the fit described in the text.

simulation by the American groups, the TESLA Collaboration has accepted it. This assumption then leads directly to a reasonably large value of BR^2 to provide charged-neutral separation in a jet, and to an electromagnetic calorimeter (EMCal) design with a small Moliere radius and small pixel size. Additionally, it is desirable to read out each layer of the EMCal to provide maximal information on shower development. This leads to the same nominal solution as TESLA: a series of layers of about 0.5

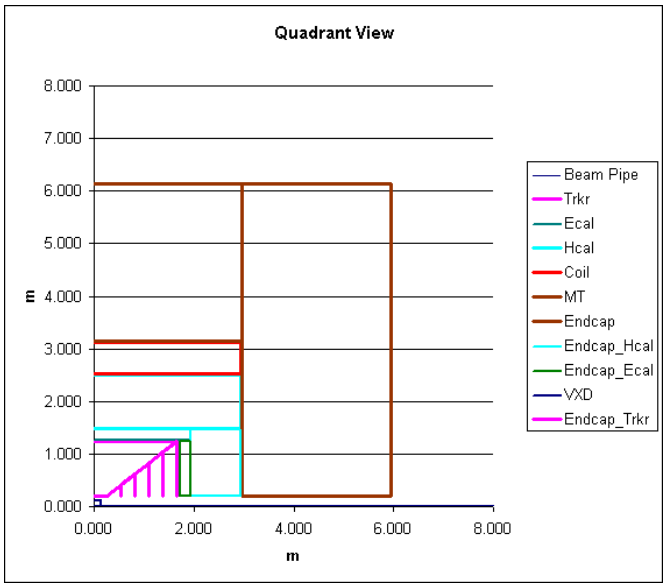

Figure 15.19: Quadrant view of the SD detector.

X_0 tungsten sheets alternating with silicon diodes. Such a calorimeter is expensive; its cost is moderated by keeping the scale of the inner detectors down. This has two implications: the space point resolution of the tracker should be excellent to meet momentum resolution requirements in a detector of modest radius, and the design should admit high-performance endcaps so that the barrel length (or $\cos\theta_{\rm Barrel}$) will be small. Obviously it is desirable to minimize multiple scattering in the tracker, but compromises will be needed and must be tested with detailed simulation. The last real strategic question is whether the Hadronic Calorimeter (HCal) will be inside or outside the coil. Locating the HCal inside the coil permits reasonably hermetic calorimetry, but requires a larger, more expensive coil and more iron to return the flux. It is assumed that the detector will have an ultra-high-performance vertex detector based on CCD's or an equivalent thin, small pixel technology, as we have discussed for the L detector. A muon tracker will be interleaved in the iron flux return utilizing reliable RPC's or equivalent.

These considerations lead to a trial design with a tracking radius of 1.25 m and a field of 5 T. This is a BR^2 of 8, compared to 10 for TESLA and 12 for the L detector. The tracker is 5 layers of silicon strips with a $\cos\theta_{\rm Barrel}$ of 0.8. Sets of five disks with silicon strips are arranged as endcaps to complete the acceptance. The HCal is inside the coil. The quadrant view is shown in Fig. 15.19, and the major dimensions are tabulated in Table 15.1.

The SD detector relies entirely upon silicon tracking in a 5 T solenoidal field in the central and forward regions. Its central and forward trackers consist of a 5-layer

silicon barrel—a silicon drift detector (SDD) or microstrips—and five layers of double-sided silicon microstrip forward disks. Figure 15.20 shows a sketch of the SD detector tracking system. The inner/outer radii of the barrel layers are 20/125 cm. The inner and outer disks are at 40 cm and 167 cm from the interaction point. The boundary between the barrel and disk system lies at $|\cos\theta| = 0.8$.

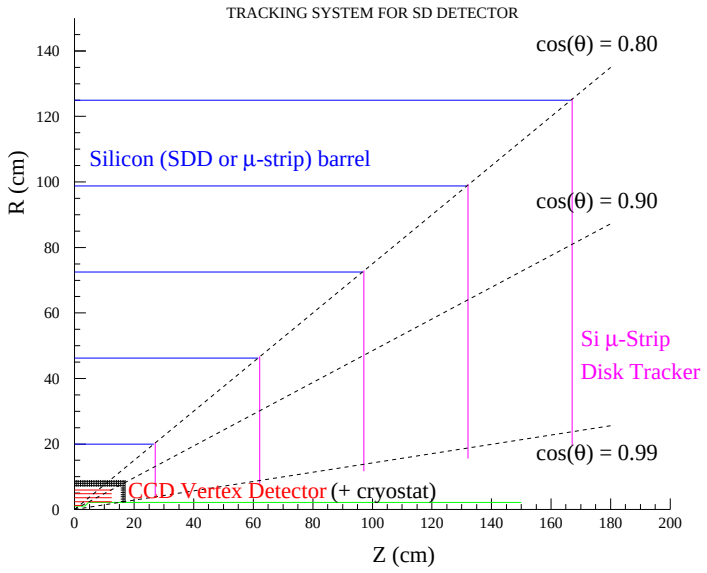

Figure 15.20: Sketch of SD detector tracking system.

The SDD option provides a solid-state analog to a time projection chamber. A potential gradient is applied via implanted cathodes in the silicon in order to force the generated electron cloud to drift through the bulk of the silicon to a collection anode. The highest voltage supplied to a single cathode can be up to 2500 V. By measuring the cloud distribution across the collection anodes and the drift time to the anodes in parallel, one records three-dimensional position information with a one-dimensional electronics readout. Three-dimensional position resolutions below 10 μm in each dimension can be achieved with an anode spacing between 200 and 300 μm. Thus, the electronics cost is considerably reduced compared to other semiconductor detector options. Recently, a three-barrel SDD Tracker, using 216 large-area Silicon Drift wafers, was successfully completed and has been installed in the STAR experiment at RHIC.

Compared to the STAR detector the following modifications would be made to build a linear collider tracker: 1) increase the wafer size to 10 cm $\times$ 10 cm; 2) reduce the wafer thickness from 300 to 150 μm; and 3) redesign the front-end electronics for lower power to eliminate water cooling. The detector contains 56 m^2 of active silicon,

requiring about 6000 wafers and 4.4 million channels distributed over 229 ladders constructed from carbon-fiber material.

The silicon strip detector (SSD) option makes use of what is at this time a very mature tracking technology. Nevertheless, several avenues for further R&D are discussed below. It should be possible to exploit the small (order 10^{-5}) duty cycle of the linear collider to reduce the power dissipated by the readout electronics by switching to a quiescent state in between trains. This would substantially reduce the heat load, leading to a great reduction in the complexity and material burden of the mechanical structure.

In order to improve the robustness of the detector against linear collider backgrounds, it should be possible to develop a microstrip readout with a short shaping time, with timing resolution of order 5–10 nsec. This would allow out-of-time background hits to be eliminated from the bunch train with a rejection factor of better than 10:1.

On the other hand, the high granularity of microstrip detectors would make an SSD central tracker fairly robust against backgrounds even in the absence of intra-train timing. If instead it is felt that low- and intermediate-momentum track parameter resolution is more important than timing resolution, the use of a readout with a very long shaping-time should make it possible to implement detector ladders of substantially greater length than that of the 10–20 cm ladders of conventional strip detector systems. The AMS collaboration has developed a slow readout [19] with 6 electrons equivalent noise per cm of detector length. This may allow single ladders to stretch the entire half-length of the outermost silicon layer, and for the inner layers to be thinned. This, combined with a space frame that derives much of its support from the ladders themselves, would lead to a substantial reduction in the material burden, and give an overall low-momentum track parameter resolution on par with that of the L detector.

The forward disks for the SD tracker would have the same intrinsic performance as those described above for the L detector.

The performance of the SD detector tracking system, including the CCD vertex detector, is summarized in Fig. 15.11 and Fig. 15.12. In the limit of high-momentum tracks, the SD tracking resolution in $1/p_t$ is 2×10^{-5} GeV^{-1}.

The EMCal consists of layers of tungsten with gaps sufficient for arrays of silicon diode detectors mounted on G10 mother boards. The thickness of these gaps is a major issue, in that it drives the Moliere radius of the calorimeter. A thickness of 4 mm seems quite comfortable, accommodating a 0.3-0.5 mm silicon wafer, a 2 mm G10 carrier, and 1.5 mm of clearance. Conversely, 1.5 mm seems barely plausible, and probably implies a stacked assembly rather than insertion into a slot. For now, we assume a 2.5 mm gap.

It is expected that the readout electronics from preamplification through digitization and zero suppression can be integrated into the same wafer as the detectors. A

fallback would be to bump- or diffusion-bond a separate chip to the wafer. Thus it is expected that the pixel size on the wafer will not affect the cost directly. A pixel size between 5 and 10 mm on a side is expected. Shaping times would be optimized for the (small) capacitance of the depleted diode, but will probably be too long to provide any significant bunch localization within the train.

The HCal is chosen to lie inside the coil. This choice permits much better hermeticity for the HCal, and extends the solenoid to the endcap flux return. This makes a more uniform field for the track finding, and simplifies the coil design. The HCal absorber is a non-magnetic metal, probably copper or stainless steel. Lead is possible, but is mechanically more difficult. The detectors could be 'digital', with high-reliability RPC's assumed. The HCal is assumed to be 4 λ thick, with 34 layers of radiator 2 cm thick alternating with 1 cm gaps.

We have examined performance for the SD detector model in the same way as the L detector, calculating the asymptotic limit of performance. (See the corresponding discussion in Section 4.1 for the limitations of this analysis.) The electromagnetic energy resolution is expected to be $18\%/\sqrt{E}$. Figure 15.14 presents the expected π^- energy resolution. The resolution for jet energy reconstruction is given in Fig. 15.21. A fit to these data gives for the asymptotic limit

$$\frac{\sigma_{E_{\rm jet}}}{E_{\rm jet}} = \frac{0.15}{\sqrt{E_{\rm jet}}} \ . \tag{15.3}$$

As previously, we fit a Gaussian to the distribution near $E_Z = E_{\rm beam}$ to extract a measure of the M_{jj} resolution. This resolution, σ_{Mjj}/M_{jj}, is plotted vs. E_Z in Fig. 15.22. A fit to the data of the form $(A/\sqrt{E_Z}) \oplus B$ gives

$$\frac{\sigma_{Mjj}}{M_{jj}} = \frac{0.72}{\sqrt{E_Z}} \ , \tag{15.4}$$

with negligible constant term. These idealized studies are not yet precise enough to conclude that this is significantly worse than the L Detector performance.

The coil concept is based on the CMS design, with two layers of superconductor and stabilizer. The stored energy is 1.4 GJ, compared to about 2.4 GJ for the TESLA detector and 1.7 GJ for the L detector. The coil thickness is 60 cm, which is probably conservative.

The flux return and muon tracker is designed to return the flux from the solenoid, although the saturation field for the iron is assumed to be 1.8 T, which may be optimistic. The iron is laminated in 5 cm slabs with 1.5 cm gaps for detectors.

4.3 P detector for the lower-energy IR

The P Detector is proposed as a lower-cost detector for the second IR, capable of the performance required for lower-energy operation, including the Z-pole physics.

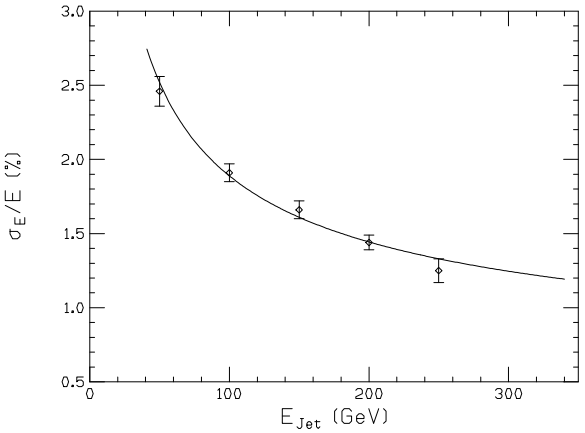

Figure 15.21: Jet energy resolution (in %) *vs.* jet energy for the SD detector. The curve is the fit described in the text.

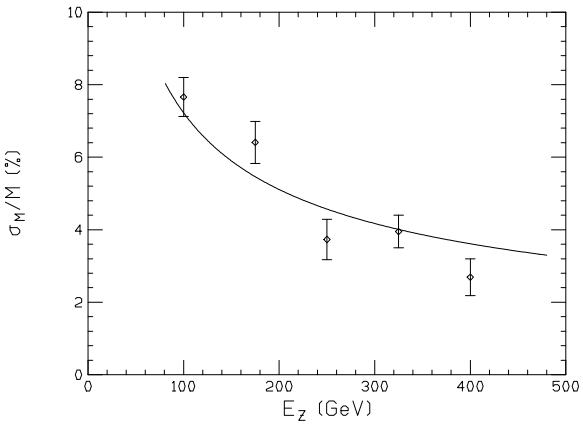

Figure 15.22: Jet-jet mass resolution (in %) for $Z \to 2$ jets *vs.* Z energy for the SD detector in $e^+e^- \to ZZ \to$ hadrons events. The curve is the fit described in the text.

The P detector is illustrated in Fig. 15.23. The dimensions of the P Detector are presented in Table 15.1.

The P detector employs the same CCD vertex detector design described for the L detector above, illustrated in Fig. 15.7.

The P detector's tracker design is modelled very closely upon that of the L detector. Since it is meant to operate at lower center-of-mass energies, its required resolution in $1/p_t$ is correspondingly less severe, allowing for a smaller tracking system and therefore a smaller, cheaper overall detector design. Figure 15.24 shows a sketch of the P detector tracking system.

Briefly, the P central tracker consists of a 120-layer TPC, of inner/outer radii = 25/150 cm and half-length 200 cm. Again, one or more intermediate tracking layers of silicon or scintillating fiber just inside the inner TPC radius may be desirable. The forward tracker consists of five silicon microstrip disks similar to those in the L and SD detectors. The performance of the P detector tracking system in a 3 T solenoidal field, including the CCD vertex detector, is summarized in Fig. 15.11 and Fig. 15.12. In the limit of high-momentum tracks, the P tracking resolution in $1/p_t$ is 6×10^{-5} GeV^{-1}.

The 3 Telsa solenoidal coil is located outside the electromagnetic calorimeter and inside the hadronic calorimeter. This compromise (over the desire to move the coil outside the hadronic calorimeter) contains the cost of the P detector. The inner radius of the solenoid is 185 cm.

The electromagnetic calorimeter of the P Detector consists of 32 layers of lead-scintillator laminate, with 4 mm lead layers followed by 3 mm scintillator, for 22.8

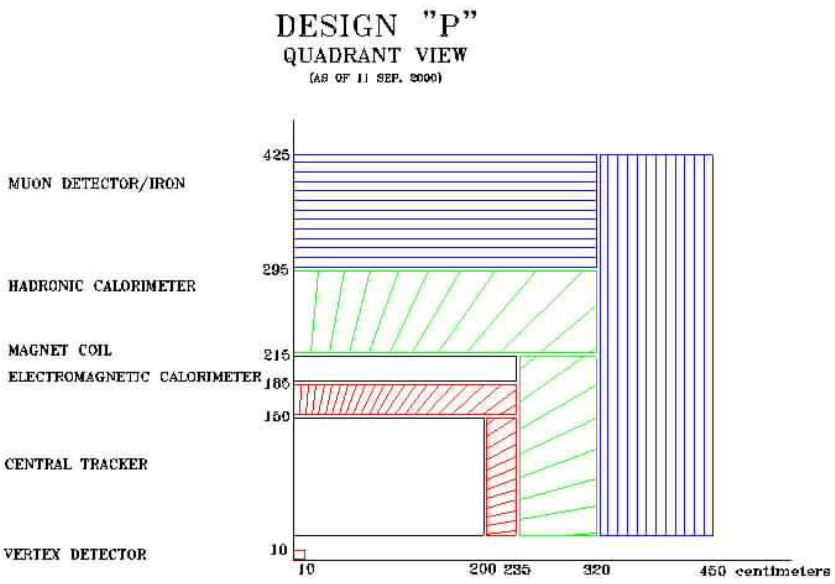

Figure 15.23: Quadrant view of the P detector.

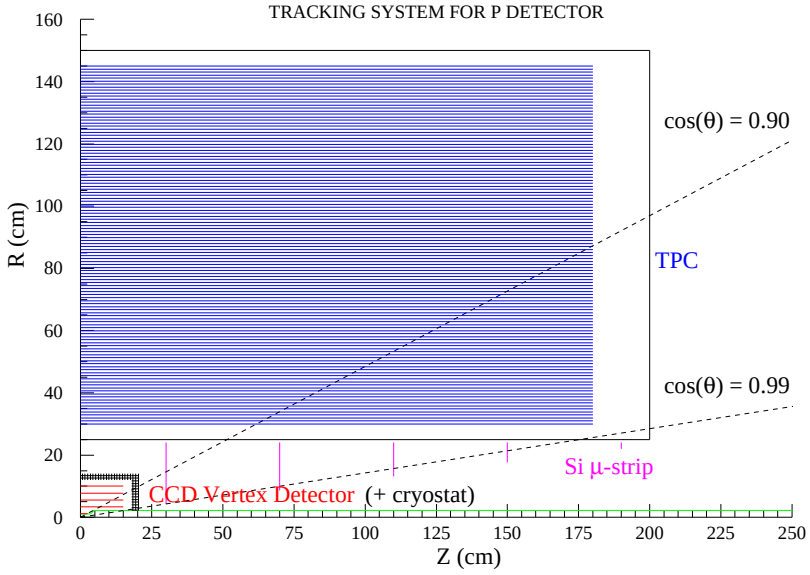

Figure 15.24: Sketch of P detector tracking system.

radiation lengths. These layers are ganged in pairs, giving 16 readout layers. One layer of 1 cm^2 silicon pads is forseen near the EMCal shower maximum. The transverse segmentation of the scintillator is 2 degrees $\times$ 2 degrees. It has an inner radius of 150 cm.

The hadronic calorimeter is 65 layers of 8 mm lead layers with 3 mm scintillator sampling. These layers are ganged to produce 8 independent samples. The inner radius of the hadronic calorimeter barrel is 215 cm. The entire calorimeter (electromagnetic and hadronic) comprises 3.9 interaction lengths. The transverse segmentation of the scintillator in the hadronic calorimeter is 4 degrees $\times$ 4 degrees.

Given its segmentation, the P detector would not be well-suited for using energy flow in jet reconstruction. Unlike L and SD, the segmentation is organized as towers of constant θ and ϕ. For running at the Z, excellent jet reconstruction is probably not an important issue. However, at higher energy, for light Higgs or W-pair physics, for example, this conclusion is less clear. Jet reconstruction for P would most likely be carried out using the calorimeter alone (or the tracker alone). Note, however, that the Pb-scintillator ratio, as currently proposed, would not be expected to give good compensation of electromagnetic and hadronic energy depositions. Performance results for jet reconstruction, similar to those given for L and SD, have not yet been carried out. The results would provide an interesting point of comparison to the energy flow performance of SD.

The muon system consists of 10 layers of 10 cm iron plates, with 3 cm gaps for RPC detectors. Axial strips of 3 cm pitch measure the ϕ coordinate to 1 cm precision in all 10 gaps, and two gaps (5 and 10) provide azimuthal strips for a measurement of the z coordinate to 1 cm precision.

4.4 Cost estimates

The costs of the subsystems of each of the three detectors have been estimated based on past experience and escalation to FY01. The three cost estimates are shown in Table 15.2. Approximately 40% contingency is assumed for each of the detectors, resulting in a total cost estimate of \$359 million for the L detector, \$326 million for the SD detector, and \$210 million for the P detector.

References

[1] TESLA Technical Design Report, http://tesla.desy.de/new_pages/TDR_CD/start.html

[2] T. Matsui, in *Physics and Experiments with Future Linear Colliders (LCWS99)*, ed. E. Fernandez and A. Pacheco. (Univ. Auton. de Barcelona, Bellaterra, 2000).

[3] C. Hensel, LC-DET-2000-001, Table 7 (2000).

Detector	L	SD	P
1.1 Vertex	4.0	4.0	4.0
1.2 Tracking	34.6	19.7	23.4
1.3 Calorimeter	48.9	60.2	40.7
1.3.1 EM	(28.9)	(50.9)	(23.8)
1.3.2 Had	(19.6)	(8.9)	(16.5)
1.3.3 Lum	(0.4)	(0.4)	(0.4)
1.4 Muon	16.0	16.0	8.8
1.5 DAQ	27.4	52.2	28.4
1.6 Magnet & support	110.8	75.6	30.5
1.7 Installation	7.3	7.4	6.8
1.8 Management	7.4	7.7	7.4
SUBTOTAL	256.4	242.8	150.0
1.9 Contingency	102.6	83.4	60.0
Total	359.0	326.2	210.0

Table 15.2: e^+e^- linear collider detector budgets (WBS to subsystem level) in M$ FY01.

[4] The SLD Collaboration, Nucl. Inst. and Meth. **A400**, 287 (1997).

[5] J. E. Brau and N. Sinev, IEEE Trans. Nucl. Sci. **47**, 1898 (2000).

[6] M. N. Frary and D. J. Miller, DESY 92-123A, Vol I, 1992, p. 379; D. Cinabro, in *Physics and Experiments with Future Linear Colliders*, ed. E. Fernandez and A. Pacheco. (Univ. Auton. de Barcelona, Bellaterra, 2000).

[7] J.-C. Brient, in *Physics and Experiments with Future Linear e^+e^- Colliders (LCWS 2000)*, ed. A. Para. (AIP Conference Proceedings, 2001).

[8] P. Gay, in *Physics and Experiments with Future Linear e^+e^- Colliders (LCWS 2000)*, ed. A. Para. (AIP Conference Proceedings, 2001).

[9] P. Checchia, in *Physics and Experiments with Future Linear e^+e^- Colliders (LCWS 2000)*, ed. A. Para. (AIP Conference Proceedings, 2001).

[10] T. Behnke, S. Bertolucci, R. Heuer, R. Settles, eds. DESY Pub: 2001-011 March 2001 Part III, A Detector for TESLA, p. IV-107.

[11] A. Para, in *Physics and Experiments with Future Linear e^+e^- Colliders (LCWS 2000)*, ed. A. Para. (AIP Conference Proceedings, 2001).

[12] R. J. Wilson, in *Physics and Experiments with Future Linear Colliders (LCWS99)*, ed. E. Fernandez and A. Pacheco. (Univ. Auton. de Barcelona, Bellaterra, 2000).

[13] R. J. Wilson, in *Physics and Experiments with Future Linear e^+e^- Colliders (LCWS 2000)*, ed. A. Para. (AIP Conference Proceedings, 2001).

[14] H. Yamamoto, in *Physics and Experiments with Future Linear Colliders (LCWS99)*, ed. E. Fernandez and A. Pacheco. (Univ. Auton. de Barcelona, Bellaterra, 2000).

[15] M. Ronan and R. Settles, to appear in *Proceedings of the Vienna Instrumentation Conference*, Vienna, Austria, Feb 19–23, 2001.

[16] R. Yarema *et al.*, Fermilab-TM-1892, June 1994 (revised Oct. 1996).

[17] Boeing Electronic Systems, 3370 Miraloma Ave, Anaheim, CA 92803; M. D. Petroff *et al.*, Appl. Phys. Lett. **51**, 406 (1987).

[18] For a cost breakdown, see `http://www-mhp.physics.lsa.umich.edu/~keithr/LC/trackercosts.html`.

[19] M. Fauluzzi, Nucl. Inst. and Meth. **383**, 35 (1996).

Questions for Further Study

Chapter 16 Suggested Study Questions on LC Physics and Experimentation

1 Physics issues

1.1 Higgs physics

For further information on this section, consult with: Jack Gunion, Howard Haber, Andreas Kronfeld, Rick van Kooten.

1. Perform a fully simulated study of the precision to which Higgs branching ratios can be determined for $m_h = 115$ GeV; for $m_h = 140$ GeV; for $m_h = 200$ GeV. How do these precisions depend on CM energy?

2. Is $\gamma\gamma$ needed to measure the total Higgs width, for low mass Higgs?

3. Outline the necessary experimental program to determine the spin/parity of a putative Higgs state.

4. Optimize a program for determination of the Higgs self-couplings. What requirements does this study impose on the dijet invariant mass resolution?

5. What is the utility of positron polarization for Higgs measurements?

6. From knowledge of measured Higgs branching ratios (fermion pairs, ZZ, WW, gg, $\gamma\gamma$), the total width, and the couplings g_{ZZh}, g_{WWh}, what reach is available to detect the presence of the SUSY states H, A? What is the relative importance of errors in each measurement?

7. To what extent can one measure $\tan\beta$ for the SUSY Higgs from Higgs sector measurements alone? Is it possible to do so in a truly model-independent way for the most general sets of MSSM parameters?

8. How will one disentangle H^0 and A^0 in the decoupling limit where the masses are nearly degenerate?

9. Contrast the use of e^+e^- and e^-e^- beams for the $\gamma\gamma \to h$ measurement. The use of e^+e^- admits numerous physics backgrounds that are absent for e^-e^-. Is it critical to avoid these backgrounds? Can the advantage of e^-e^- over e^+e^- be compensated by higher integrated luminosity?

10. The dominant backgrounds to $\gamma\gamma \to h \to b\overline{b}$ are $\gamma\gamma \to b\overline{b}(g)$ and $\gamma\gamma \to c\overline{c}(g)$. The production cross section for $c\overline{c}(g)$ is about 25 times larger than for $b\overline{b}(g)$. The background can be suppressed, first, by improved b tagging, and second, by improved Higgs (two-jet) mass resolution. With this in mind, what is the optimal strategy for isolating the Higgs peak from the background?

11. Contrast the use of e^+e^- and e^-e^- beams, in the same way, for a broadband search for a heavy Higgs s-channel resonance in $\gamma\gamma$.

1.2 Supersymmetry

For further information on this section, consult with: Jonathan Feng, Uriel Nauenberg, Frank Paige, James Wells.

1. Develop a plan for measuring the chargino mass matrix, including mixing, for the most general sets of MSSM parameters.

2. Do the same for the neutralino, stau and stop mixing matrices.

3. Is there a program by which one could, at least in principle, measure all 105 independent MSSM parameters?

4. What can LC measurements tell us, and with what precision, about the nature of the SUSY model and the SUSY breaking mechanism and scale? What can be learned about the scale and physics of grand unification?

5. Evaluate the benefit of positron polarization for SUSY measurements.

6. For what questions of SUSY spectroscopy are $\gamma\gamma$, $e\gamma$, and e^-e^- beams of special importance?

7. How well can CP-violating effects be studied in supersymmetry? How do these compare and connect to those made in the B factories or K decays?

8. What limits can be set on lepton flavor violation in slepton reactions? Is it possible to measure quark flavor violation effects that are associated with SUSY parameters and independent of CKM mixing?

9. What measurements from the LC would be required to verify the neutralino origin of cosmological dark matter?

10. What information encoded in the SUSY parameters can provide information about the nature of string/M theory?

1.3 New physics at the TeV scale

For further information on this section, consult with: Tim Barklow, Bogdan Dobrescu, JoAnne Hewett, Slawek Tkaczyk.

1. What precision can eventually be reached on anomalous WWV, ZZV and $t\bar{t}V$ couplings? What machine parameters are needed?

2. For the broad range of strong coupling models that obey existing precision EW constraints, what are the observable consequences at a 500 GeV LC? At 1000 GeV? At 1500 GeV? Are there models of strong coupling for which there are no observable consequences at 500 GeV?

3. Is it possible for models of a strong-coupling Higgs sector to mimic predictions of supersymmetry or extended Higgs models in a way that these models cannot be distinguished at the LHC? What e^+e^- measurements would be most important in these cases?

4. What is the utility of $\gamma\gamma$ or e^-e^- operation for probing the strong coupling models?

5. Develop general classification of models with large extra dimensions.

6. How can measurements at the TeV scale constrain string/M-theory models with string or quantum gravity scales much less than 10^{19} GeV?

7. Describe the reach of a LC for seeing large extra dimensions as a function of energy and luminosity in various scenarios. To what extent does the higher precision of a 500 GeV LC complement the higher energy reach of the LHC?

8. What is the role of $\gamma\gamma$, $e\gamma$, and e^-e^- experiments in probing models with extra dimensions?

9. What would be the role of the LC in understanding the nature of cosmological dark matter in models not related to supersymmetry?

10. In what way can LC measurements constrain gravitational effects such as Hawking black hole radiation?

1.4 Top quark physics

For further information on this section, consult with: Ulrich Baur, David Gerdes.

1. How well can the top quark width be determined from threshold measurements? A full analysis should include the threshold shape, the top quark momentum distribution, and the forward-backward asymmetry from S–P mixing. Are there additional effects that can contribute to this determination?

2. Can one determine the top quark Yukawa coupling at the $t\bar{t}$ threshold? With what precision?

3. Can CP violation associated with the top quark be probed at the $t\bar{t}$ threshold?

4. Can a high-precision top quark mass be obtained from continuum $t\bar{t}$ production? Is there an infrared-safe definition of m_t that can be applied to this analysis?

5. How well can the top quark Yukawa coupling be determined in $e^+e^- \to t\bar{t}h$? What backgrounds arise from other top quark production processes (*e.g.*, $e^+e^- \to t\bar{t}g$)? Are spin correlations derived from kinematic fitting useful in this analysis?

6. How well can one measure the vector and axial $t\bar{t}Z$ couplings?

7. How well can one measure the $t\bar{t}\gamma$ form factors and the top anomalous magnetic moment?

8. How well can one measure the $(V + A)$ decay of the top quark?

9. What ambiguities arise when one fits for more than one anomalous coupling at a time? Can polarization or spin correlation measurements resolve these ambiguities?

1.5 QCD and two-photon physics

For further information on this section, consult with: Bruce Schumm, Lynne Orr.

1. What is the precision that can be obtained for α_s from e^+e^- annihilation? In particular, can it be definitively demonstrated that detector systematics are less than $\pm 1\%$?

2. What is the precision that can be obtained for α_s from measurements on the top quark?

3. Outline the program for obtaining the photon structure functions. What energies of operation are desired, and are special beam conditions required?

4. How can the LC make definitive studies of all-orders BFKL resummation?

1.6 Precision electroweak measurements

For further information on this section, consult with: Lawrence Gibbons, Bill Marciano.

1. Evaluate the need for Giga-Z in various scenarios in which there do or do not exist light Higgs particles.

2. Evaluate the need for Giga-Z in scenarios in which new light particles from supersymmetry or other new physics are discovered.

3. Are there strategies for further improving the precision for measuring $\sin^2\theta_w$ using Z-pole observables? How can the various systematics limits described in the text be avoided?

4. Evaluate the precision of W and top quark mass measurements. What special measurements of the accelerator parameters will be needed to achieve this precision?

5. What are the systematic limits on B physics measurements, including CKM parameters and rare B decay rates, at a polarized Z factory?

2 Accelerator issues

2.1 Running scenarios

For further information on this section, consult with: Joel Butler, Paul Grannis, Michael Peskin.

1. What elements should be present in a charge to a future international technical panel established to compare linear collider technical proposals? What emphasis should be given to risk analysis, needed R&D, upgradability in energy or luminosity, cost comparison?

2. For a physics-rich scenario (*e.g.*, low mass Higgs and SUSY with observable $\widetilde{\chi}_1^0$, $\widetilde{\chi}_2^0$, $\widetilde{\chi}_1^+$, $\widetilde{t}$, $\widetilde{\tau}$) outline the desired run plan, giving the required integrated luminosity for all necessary beam energies, beam polarizations, beam particles. What compromises can be envisioned to limit the number of distinct machine parameters without undue effect on the physics results?

3. Do the same for a thinner physics scenario (*e.g.*, with Higgs mass of 180 GeV and no supersymmetry or other new particle observation).

2.2 Machine configuration

For further information on this section, consult with: Charles Prescott, Tor Raubenheimer, Andre Turcot.

1. Evaluate an IR scheme with IR1 capable of operation at $E_{CM} \leq 250$ GeV and IR2 capable of operation at $E_{CM} < 500$ (1000) GeV. Contrast this configuration with one in which two detectors share an IR in push-pull mode.

2. How important is it that the LEIR be able to operate at energies of 500 GeV or higher?

3. Evaluate the benefits from simultaneous operations at two IRs (with interleaved pulse trains). What are the constraints on the collider design?

4. What are the requirements imposed on the first-phase accelerator design to permit upgrade to multi-TeV energies?

5. What constraints and opportunities are brought by including a free electron laser facility with the NLC? Are there other non-HEP uses of the linear accelerator that could be contemplated?

2.3 Positron polarization

For further information on this section, consult with: John Jaros, Steve Mrenna, Mike Woods.

1. Evaluate the need for positron polarization in accomplishing the physics program. What polarization (and error), energy (and error), luminosity are required for the relevant physics topics?

2.4 Photon collider

For further information on this section, consult with: Jeff Gronberg, Adam Para, Tom Rizzo, Karl van Bibber.

1. Compile the list of physics topics for which $\gamma\gamma$ operation is essential or desirable.

2. Typically $\gamma\gamma$ luminosity and $e\gamma$ luminosity are comparable at a $\gamma\gamma$ collider. Identify $e\gamma$ processes that might be problematic backgrounds for $\gamma\gamma$ physics analyses.

3. How can a detector be made compatible with both $\gamma\gamma$ and e^+e^- operation?

4. Is it sufficient to provide $\gamma\gamma$ collisions only for $E_{CM}(\gamma\gamma) < 400$ GeV (*i.e.*, at the low energy IR)?

5. Evaluate the prospects for high-power lasers and the configuration of the $\gamma\gamma$ IR. Is R&D needed on the most important IR components (*e.g.*, mirrors, masking, beam stability)?

2.5 e^-e^-

For further information on this section, consult with: Jonathan Feng, Clem Heusch.

1. Compile the list of physics topics for which e^-e^- operation is essential or desirable.

2.6 Fixed Target

For further information on this section, consult with: Mike Woods.

1. What experiments could be done using the e^- or e^+ beam of a linear collider for fixed target experiments? For example, can Møller scattering of a fixed target beam be used to obtain $\sin^2\theta_w$ with very high precision? Can the spent beams that have passed through the interaction region be used in these experiments?

2. What are the relative advantages of e^- *vs.* e^+ beams?

3. What experiments could be done using the polarized γ beams from laser backscattering for fixed target experiments? Can fixed target experiments be done with the spent beams while the collider is operating in $\gamma\gamma$ mode?

3 Detector issues

3.1 Detectors

For further information on this section, consult with: Jim Brau, Marty Breidenbach, Gene Fisk, Ray Frey, Tom Markiewicz, Keith Riles.

1. What are the physics reasons for wanting exceptional jet energy (mass) resolution? How do signal/backgrounds and sensitivities vary as a function of resolution? Is mass discrimination of W and Z in the dijet decay mode feasible, and necessary?

2. How does energy flow calorimetry resolution depend on such variables as Moliere radius, $\Delta\theta/\Delta\phi$ segmentation, depth segmentation, inner radius, B field, number of radiation lengths in tracker, etc.?

3. What benefits arise from very high-precision tracking (*e.g.*, silicon strip tracker)? What are the limitations imposed by having relatively few samples, and by the associated radiation budget? What minimum radius tracker would be feasible?

4. Evaluate the dependence of physics performance on solenoidal field strength and radius.